

2014-01-01

# Gas-Solid Bed Hydrodynamics Of Non-Spherical Particles

A S M Raufur Rahim Chowdhury

*University of Texas at El Paso*, [archowdhury@miners.utep.edu](mailto:archowdhury@miners.utep.edu)

Follow this and additional works at: [https://digitalcommons.utep.edu/open\\_etd](https://digitalcommons.utep.edu/open_etd)



Part of the [Mechanical Engineering Commons](#)

---

## Recommended Citation

Chowdhury, A S M Raufur Rahim, "Gas-Solid Bed Hydrodynamics Of Non-Spherical Particles" (2014). *Open Access Theses & Dissertations*. 1218.

[https://digitalcommons.utep.edu/open\\_etd/1218](https://digitalcommons.utep.edu/open_etd/1218)

This is brought to you for free and open access by DigitalCommons@UTEP. It has been accepted for inclusion in Open Access Theses & Dissertations by an authorized administrator of DigitalCommons@UTEP. For more information, please contact [lweber@utep.edu](mailto:lweber@utep.edu).

# GAS-SOLID BED HYDRODYNAMICS OF NON-SPHERICAL PARTICLES

A S M RAUFUR RAHIM CHOWDHURY

Department of Mechanical Engineering

APPROVED:

---

Norman Love Jr., Ph.D., Chair

---

Ahsan R Choudhuri, Ph.D.

---

Chunqiang Li, Ph.D.

---

Charles H. Ambler, Ph.D.  
Dean of the Graduate School

Copyright ©

by

A S M Raufur Rahim Chowdhury

2014

## **Dedication**

*To my Parents*

# GAS-SOLID BED HYDRODYNAMICS OF NON-SPHERICAL PARTICLES

by

A S M RAUFUR RAHIM CHOWDHURY, B.S.ME

THESIS

Presented to the Faculty of the Graduate School of

The University of Texas at El Paso

in Partial Fulfillment

of the Requirements

for the Degree of

MASTER OF SCIENCE

Department of Mechanical Engineering

THE UNIVERSITY OF TEXAS AT EL PASO

August 2014

## **Acknowledgements**

At first I would like to express my gratitude to my parents. I would also thank to my grandparents, siblings, cousins, uncles, aunts and friends to support during my graduate degree at The University of Texas at El Paso. I would also want to thank all my family members live in El Paso for their support towards my education. It's a great honor for me to work with supervision of my advisor Dr. Norman Love. His expert guidance helped me to become a better engineering student.

I want to thank members of my thesis committee Dr. Ahsan Choudhuri and Dr. Chunqiang Li for their insights, comments, revision and participation in my thesis presentation. I would also want to appreciate my colleagues in Center for Space Exploration Technology Research (cSETR) lab for their assistance and contribution during my research work. I would also like to thank Md. Rashedul Hasan Sarker for guiding me as a senior group member all along the project and I would also like to thank Christian Rodarte and Salvador Sandoval for being such wonderful group member. Finally, I would like to thank Olympia Caudillo, M.Ed. for her time and consideration for reviewing and formatting my thesis.

This research is supported by the U.S. Department of Energy, under awards DE-FE-0003742 (Project Manager Robie Lewis). However, any opinions, findings, conclusions, or recommendations expressed herein are those of the authors and do not necessarily reflect the views of the Department of Energy.

## **Abstract**

Gas-solid beds are ubiquitous in industrial and energy production applications. Examples include fluidized beds, which are used in many systems such as in Integrated Gasification Combined Cycle (IGCC) power plants or in chemical looping systems. These examples and others involve complicated interactions between each phase of reactants in the system. The motivation of this work stems from the need for a better understanding of bed hydrodynamics in existing energy systems; results from this work can be used directly in software such as Fluent to more accurately predict flow behaviors of gas and solid phases. The experimental data are collected from two setups including an optically accessible drag measurement facility that was used to obtain the drag coefficient at various particle Reynolds numbers and a lab-scale gas-solid packed bed which was used to validate the computational model through pressure drop measurements across the packed bed. Results showed that the new correlation presented in this thesis predicted drag with more accuracy when compared to existing models and experiments for particle sphericities up to 0.9. Implementation of the drag relationship into Fluent through a user-defined function was also done using the two-fluid model. The newly developed drag model predicted the pressure drop behavior for non-spherical particles for a wide range of particle sphericities from 0.5 to 0.9 and Reynolds numbers between 1 and 1000.

## Table of Contents

Acknowledgements.....	v
Abstract.....	vi
List of Tables .....	x
List of Figures .....	xi
Chapter 1 : Introduction .....	1
1.1 Overview.....	1
1.2 Research Objectives.....	3
1.3 Practical Relevance .....	3
1.4 Facilities.....	4
1.5 Thesis Organization .....	4
Chapter 2 : Literature Review .....	6
2.1 Multiphase Flow .....	6
2.1.1 Types of Multiphase Flow .....	6
2.2 Gasification .....	7
2.2.1 History of Gasification.....	8
2.2.2 Primary Gasification Technologies.....	10
2.3 Fluidization .....	11
2.3.1 Fluidized Bed .....	11
2.3.2 Fluidization Regimes .....	12
2.4 Gas-Solid Fluidized Bed.....	13
2.4.1 Pressure Drop.....	13
2.4.2 Minimum Fluidization Velocity.....	16
2.4.3 Void Fraction .....	17
2.4.4 Hydrodynamics Behavior of Fluidized Bed.....	18
2.5 Drag Force & Drag Correlation .....	20
2.6 Non-Linear Regression .....	23
Chapter 3 : Experimental Setup & Technical Approach.....	25
3.1 Experimental Set up.....	25
3.2 Test materials .....	28
3.2.1 Production of Non-Spherical Particles.....	29
3.2.2 Measurement of Particle Size and Shape .....	30
3.2.3 Sphericity Measurement .....	31
3.2.4 Sets of particles with different sphericity.....	34

3.3	Bed Pressure Drop and Flow Rate Measurement .....	35
3.4	High Speed Flow Visualization .....	38
3.5	Shadow sizing .....	40
3.5.1	Shadow Sizing Measurement Principle .....	41
3.5.2	Calibration.....	43
3.5.3	Shadow Sizer Processing .....	44
3.6	Test Matrix.....	47
3.7	Statistical Analysis of Experimental Data.....	48
Chapter 4 : Computational Domain .....		51
4.1	Geometry.....	51
4.2	Boundary conditions .....	52
4.3	Mesh.....	53
4.4	Eulerian-Eulerian Models .....	54
4.5	Conservation Equations .....	58
4.6	K-epsilon model:.....	59
4.6.1	Standard k-epsilon model.....	59
4.7	Problem Setup.....	61
4.7.1	General .....	61
4.7.2	Models.....	63
4.8	Drag analysis of the particles .....	65
Chapter 5 : Results and Discussions .....		67
5.1	Effect of particle density on the hydrodynamic behavior of a Gas-Solid Fluidized Bed.....	68
5.1.1	Mass distribution of the particles .....	68
5.1.2	Effect of density analysis .....	70
5.2	Drag correlation development.....	74
5.3	Comparison of computational to experimental data when using spherical particles .....	80
5.4	Qualitative comparison of bubbling behavior of particles from simulation and experiment.....	81
5.5	Plots of drag coefficient at various Reynolds numbers for different drag models and newly proposed drag model.....	82
5.6	Comparison of pressure drop versus superficial velocity using new drag model for different sphericities .....	85
5.7	Single rotating and Multiple rotating falling particles .....	88
5.7.1	Single rotating particle .....	89
5.7.2	Multiple rotating particles .....	90

Chapter 6 : Conclusion & Future Work .....	92
6.1    Conclusion .....	92
6.2    Future Work .....	93
References .....	95
Glossary .....	99
Vita.....	101

## List of Tables

Table 2.1: Voidage of Randomly Packed Beds with uniformly sized Particles Larger than 500 $\mu\text{m}$ . (Packing of Non-Spherical particles) [14] .....	18
Table 2.2: Summary of select non-spherical drag coefficients available in literature .....	22
Table 3.1: Sphericity of Different Shapes, Materials and Commonly Used Pickings [48] .....	34
Table 3.2: Ranges of Particles and Sphericity .....	35
Table 3.3: t-distribution table.....	50
Table 4.1: Conditions for the Simulation Using 2D Assumption .....	65
Table 5.1: Analytical and Experimental Minimum fluidization Velocity and Pressure Drop for 90-425 $\mu\text{m}$ Hematite particles .....	71
Table 5.2: Analytical and Experimental Minimum fluidization Velocity and Pressure Drop for 90-425 $\mu\text{m}$ Borosilicate glass beads particles.....	71
Table 5.3: Analytical and Experimental Minimum fluidization Velocity and Pressure Drop for 125-300 $\mu\text{m}$ Hematite particles .....	72
Table 5.4: Analytical and Experimental Minimum fluidization Velocity and Pressure Drop for 125-300 $\mu\text{m}$ Borosilicate glass beads particles. ....	73
Table 5.5: Values of constants used in Eq. 5.3 for different sphericities to predict $C_D$ .....	76
Table 5.6: Percent of Deviation in pressure drop at minimum fluidization.....	88
Table 5.7: Single rotational particle's experimental and numerical values .....	90
Table 5.8: Multiple rotational particles experimental and numerical values .....	91

## List of Figures

Figure 2.1: Gasification Technology [9] .....	8
Figure 2.2: Schematic representation showing appearance of flow regimes relevant to gas-solid fluidization [14] .....	14
Figure 3.1: Schematic Diagram of Laboratory Scale Fluidized Bed .....	26
Figure 3.2: Laboratory Scale Fluidized Bed .....	27
Figure 3.3: (a) Air Delivery System (b) High Pressure Blower (c) Butterfly Valve (d) Thermal Mass Flow Meter (e) Digital Differential Manometer (d) External Power Supply .....	28
Figure 3.4: Zoomed Image of 1 mm Spherical Particles .....	29
Figure 3.5: CRAVER 3851 Hydraulic Compressor.....	30
Figure 3.6: (a) Stake of Sieve Pan (b) Sieve Shaker (c) Precision Balance.....	31
Figure 3.7: (a) Dino Capture Microscope (b) Focusing the Particles .....	32
Figure 3.8: (a) Calibration Image (b) Sample Image of Non-Spherical Particle (c) Measurement of Circumscribe Diameter of Non-Spherical Particles.....	32
Figure 3.9: Particles are arranged with different size and sphericity .....	35
Figure 3.10: Digital Manometer with RS 232 Cable .....	37
Figure 3.11: Handheld Data Logger for Digital Manometer .....	37
Figure 3.12: Data Logger for Flow Meter.....	38
Figure 3.13: Schematic image of Experimental Setup for Terminal Velocity Measurement of Particles ..	40
Figure 3.14: Schematic Diagram of Shadow Sizing .....	41
Figure 3.15: LED Constellation System .....	42
Figure 3.16: Dantec High Speed Camera.....	42
Figure 3.17: Shadow Sizing.....	43
Figure 3.18: Calibration Image .....	44
Figure 3.19: Particle Selection with its Contour .....	45
Figure 3.20: Shadow Image of Test Particles .....	46

Figure 3.21: Example of Shadow Sizer Processed Result .....	46
Figure 4.1: (a) Schematic diagram of the fluidized bed, (b) Geometry made in ANSYS Workbench 13.052 .....	
Figure 4.2: Boundary Conditions.....	53
Figure 4.3: (a) Mesh of the 2D bed, (b) Bottom section of the bed .....	54
Figure 4.4: Problem Setup .....	61
Figure 4.5: Mesh Scale in the General Section .....	62
Figure 4.6: Mesh Quality. ....	63
Figure 4.7: Models .....	64
Figure 5.1: Mass Distribution of 90-425 micro meter particles in weight%.....	69
Figure 5.2: Mass distribution for Hematite Particles. ....	69
Figure 5.3: Mass distribution for Glass beads Particles.....	69
Figure 5.4: Pressure Drop vs. Superficial Velocity for 90-425 $\mu\text{m}$ particle and 5 cm bed height .....	73
Figure 5.5: Pressure Drop vs. Superficial Velocity for 125-300 $\mu\text{m}$ particle and 5 cm bed height. ....	74
Figure 5.6: Drag coefficient vs Reynolds number for Sphericity of 0.47 .....	77
Figure 5.7: Drag coefficient vs Reynolds number for sphericity 0.53 .....	77
Figure 5.8: Drag coefficient vs Reynolds Number for sphericity 0.58 .....	78
Figure 5.9: Drag Coefficient vs Reynolds Number for sphericity 0.63 .....	78
Figure 5.10: Drag Coefficient vs Reynolds Number for sphericity 0.68 .....	79
Figure 5.11: Drag Coefficient Vs Reynolds Number for sphericity 0.73 .....	79
Figure 5.12: Comparison of computational to experimental data.....	81
Figure 5.13: Qualitative comparison of bubbling behavior of particles from (top) simulation and experiment (bottom) at $t = 2, 5, \text{ and } 7 \text{ s}$ from left to right .....	82
Figure 5.14: Plots of drag coefficient at various Reynolds numbers ( $<10^3$ ) for different drag models including $\circ$ = Holzer and Sommerfeld [3], $\square$ = Haider and Levenspiel [15], $\Delta$ = Chien [26], and $\diamond$ = newly proposed drag model. All are compared to experimental measurements $\bullet$ . From top left values for sphericity ( $\phi$ ) are (a) 0.475, (b) 0.53, (c) 0.58, (d) 0.63, (e) 0.68 and (f) 0.90 .....	84
Figure 5.15: Pressure Drop vs. Superficial Velocity using developed model with sphericity 0.50.....	86

Figure 5.16: Pressure Drop vs. Superficial Velocity using developed model with sphericity 0.65 .....	87
Figure 5.17: Pressure Drop vs. Superficial Velocity using developed drag model with sphericity 0.90....	87
Figure 5.18: Images of the single rotating falling particle. ....	89
Figure 5.19: Image of multiple rotation falling particles .....	91

## **Chapter 1 : Introduction**

### **1.1 Overview**

Our world is full of devices dependent on an energy supply. Without a transmittable, reliable, and constant energy supply it is hard to think of how a person might make it through the day. With the increasing demand for the production of energy, researchers are making tremendous effort to produce energy more efficiently while maintaining costs low. There are various sources of energy production. Coal is one source of energy which is abundant in the United States and has been used for many years. The Department of Energy's (DoE) clean coal research and development is focused on developing and demonstrating advanced power generation and carbon capture, utilization and storage technologies for existing facilities and new fossil-fueled power plants by increasing overall system efficiencies and reducing capital costs [1]. Worldwide and in the United States, more than 40% of the electricity is generated by coal fired power plants and in the United States about 20% by natural gas [2]. Gasification is process that is widely used to produce synthetic fuels from coal. In this process, carbon monoxide, hydrogen and carbon dioxide are produced from carbonaceous material. At high temperature ( $>973$  K) using required amount of steam and/or oxygen a gas mixture is produced which is called synthetic fuel or for short 'syngas'. Coal gasification offers one of the most versatile and clean way to convert coal into electricity, hydrogen, and other valuable energy products [3]. In order to produce an abundant amount of energy it is important to increase the efficiency of the gasification power plant which is the future of power generation in the world. Adequate research is required to scale up and build gasification plants to decrease pollutants from coal combustion and increase efficiency without elevating costs. Thus the fluidized bed is a very necessary tool to produce energy from coal gasification. A fluidized bed is formed when required quantity of

particulate solid substances is placed under certain condition with a liquid or gas. The flow rate of the fluid can be elevated so that the solid particles act as though they were a fluid. Fluidized bed reactors (FBR) are catalytic reactors in which the catalyst is fluidized within the reactor. This allows for extensive mixing in all directions. A result of the mixing is excellent temperature stability and increased mass-transfer and reaction rates. Fluidized bed reactors are capable of handling large amounts of feed and catalyst [4]. The fluidized-bed reactor has the ability to process large volumes of fluid. For the catalytic cracking of petroleum naphtha to form gasoline blends, for example, the virtues of the fluidized-bed reactor drove its competitors from the market. Fluidization occurs when small solid particles are suspended in an upward- flowing stream of fluid. A reactor device which is used to carry out these multiphase chemical reactions is called gasifier. The term multiphase flow is used to refer to any fluid flow consisting of more than one phase or component [5]. Multiphase flow can be consists of any different state, liquid-gas, gas-solid, liquid-solid. In a coal gasification power plant reaction inside the fluidized bed reactor consists of gas-solid flow. Due to the complex interaction of the particles in the bed the solid behavior is very difficult to access [6]. At the same time, it is very important to understand the process very well, so that fluidized bed can be designed. Analyzing the fluidized bed computationally an area that researchers are trying to develop. Computational analysis of fluidized bed can help to study the multiphase flow phenomena inside fluidized bed reactors of different scale and size. Numerous developments need to be made in order to understand the fluidized bed behavior computationally. For this reason, this thesis focuses on understanding the hydrodynamic behavior of the fluidized bed experimentally and computationally.

## **1.2 Research Objectives**

The purpose of this study is to analyze the characteristics of the fluidized bed experimentally and computationally. Minimum fluidization is one of the important parameters that are used to design a gasifier or fluidized bed. For this study the drag of the particle is studied since it is a very important parameter that will allow for more accurate prediction of flow behavior. Very little studies are found in literature which show the experimental development and implementation of a drag model for non-spherical particles into the Two-Fluid model. This project will document how well the new drag model predicts the change of pressure drop with the change of superficial velocity with the experiment. The following tasks are outlined in this thesis:

- 1) Effect of Particle Density on Hydrodynamic Behavior of a Gas-Solid Fluidized Bed for non-spherical particles.
- 2) Development of a drag model for non-spherical particles
- 3) Prediction of minimum fluidization velocity using the existing drag models
- 4) Implementation of the drag model that is produced using here in Two Fluid model
- 5) Comparison of the results found implementing the drag model in the ANSYS 13.0 Fluent with other existing drag models in literature and with data from experiments for Glass beads particles.

## **1.3 Practical Relevance**

The drag model developed in this thesis can be used in the computational two fluid model to predict the pressure drop and hydrodynamic behaviors in a gas-solid gasifier operating on non-spherical particles more accurately. This drag model can be used in many applications. The data then produced from the experiments and use of the drag relationship can be used for designing a

fluidized bed for different scales and sizes. Using these data, a fluidized bed can be built with more accurate predictions which can save cost and time for designing.

#### **1.4 Facilities**

The experimental work was done in the Center for Space Exploration Technology Research (cSETR) at the University of Texas at El Paso laboratories in E105 Goddard Laboratory, located on the first floor of the engineering building and in E211 Challenger – Columbia Laboratory. The laboratories are outfitted with wide range of instruments with hydraulic compressor, high speed camera, 5 HP blower, sieve shaker, microscopic camera, flow meter, differential manometer etc. to perform experiment and experimental measurements. Computational works were done in the cSETR Computation Center E201. The computational lab is equipped with twelve core i5 computers for the computational work. The computational lab is connected to a server which is located at the University of Texas at El Paso, which has 11 nodes and 8 core processors on each of the nodes. If required this computational lab also has the facility to connect to the Texas Advanced Computing Center (TACC), which one of the most powerful super computers available.

#### **1.5 Thesis Organization**

In Chapter 1 the importance of coal and coal gasification technology is being briefly discussed. Related topics such as fluidized bed, fluidized bed reactor and multiphase flow are summarized. Research objectives and the facilities available at the University of Texas at El Paso are also mentioned here. Chapter 2 contains the literature review of this thesis. This chapter discusses the literature review of the gasification technology, fluidized beds, and different types of multiphase flows, drag force, the two fluid model, and the discrete element method. The experimental set up, design parameters, test matrix, computational domain, computational

technique are explained in Chapter 3. Chapter 4 depicts the results found from the experiments, computational model, and compares the results with the theoretical findings existing in literature. Chapter 5 succinctly explains the results and compares the results with literature and recommended works for the future.

## **Chapter 2 : Literature Review**

### **2.1 Multiphase Flow**

Multiphase flow is a kind of flow consisting more than one phase or component. In multiphase flow two or more phases are not chemically reacted. Solid, liquid and gaseous are the three general phases exists. It is a flow of the mixture of more than one of these phases. In fluid mechanics, multiphase flow is a generalization of the modelling used in two-phase flow to cases where the two phases are not chemically related or where more than two phases are present. Each of the phases is considered to have a separately defined volume fraction, and velocity field.

#### **2.1.1 Types of Multiphase Flow**

##### **2.1.1.1 Dispersed Phase and Separated Flows**

Disperse phase flow is a kind of flow in which one phase is consists of discrete elements, such droplets in a gas or bubbles in a liquid [7]. For this kind of flow discrete elements are not connected. Separated flow is a kind of flow where two phases are separated by line of contact. An annular flow is a separated flow in which there is a liquid layer on the pipe wall and a gaseous core.

##### **2.1.1.2 Gas-Liquid Flows**

Gas-liquid flows are omnipresent in our life. This kind of flow has many applications in our daily life. Gas-liquid flows contain gas bubbles in liquid flow or liquid droplets in gaseous flow. Process industries are interested to use this type of flow. Formation of droplets of combustible liquid fuel is very important for internal combustion engine, spray formation with droplets for processing materials. Also in heat exchanger the use of steam water flow are very common.

#### **2.1.1.3 Gas-Solid Flows**

Gas-solid Flows contain suspended solid particle by gas. Gasification is a perfect example of gas-solid flows. In fossil fuel power plant, the combustion of coal depends of coal particle burning and suspension of coal particles into gasifying agents. Cyclone separator and electrostatic precipitators are also use the principle of gas-solid flow. Moreover, gas-solid flows are also used for pneumatic transportation.

#### **2.1.1.4 Liquid-Solid Flows**

Liquid-solid flows contain liquid solid particles. This kind of low is also called slurry flows. This flow has also many applications in our daily life. Solid particles are transported using this kind of flow.

#### **2.1.1.5 Three-Phase Flows**

Three phase flows are also encountered in engineering problem. For example bubbles in slurry flows are an example of three phase flow. In literature, not much work has been found about three phase flow.

### **2.2 Gasification**

Gasification is a process which through a set of chemical reactions, oxygen and steam is used to convert the carbon containing feedstock to synthesis gas or syngas. Syngas is a mixture of hydrogen, carbon monoxide, carbon dioxide and other gaseous compounds. The chemical reaction takes place in a controlled environment and produces the syngas. Gasification is one of the technologies which has proven to be a robust tool for power production and can be operated either as a simple, low technology system based on a fixed-bed gasifier, or as a more

sophisticated system using fluidized-bed technology [8]. Gasification is a technology that brings a new horizon in the area of efficient and cost effective energy production.

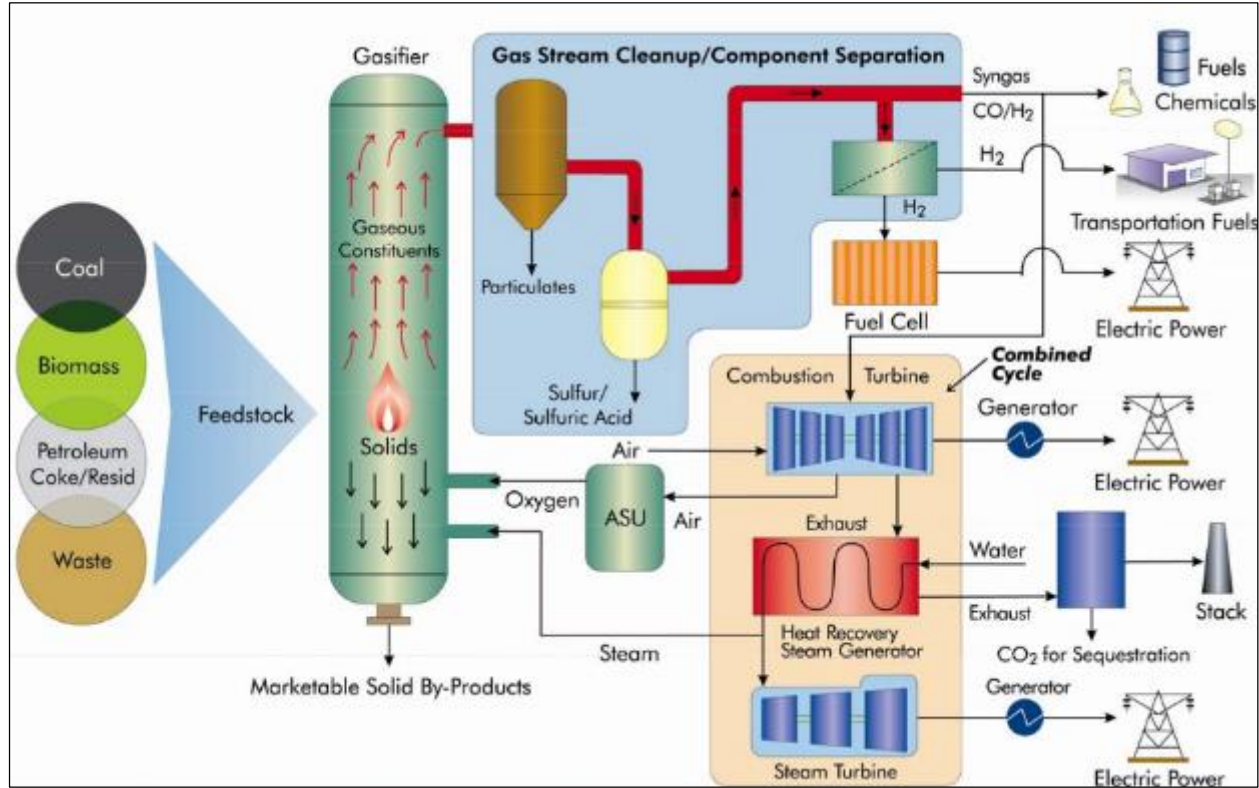


Figure 2.1: Gasification Technology [9]

The gasification process breaks the feedstock that is used into simpler components by which it removes impurities such as sulfur and mercury and high temperature drives out ash from feedstock which ensures a clean production of synthetic gas. Although synthetic gas has lower heating value than natural gas it can still be used in high-efficiency combined cycle electric power plants or to make many products presently made from natural gas such as ammonia fertilizer, methanol derived chemicals.

### 2.2.1 History of Gasification

Gasification was invented in the early-1800s. It has undergone a complete transformation since then. In the last two decades rapid changes have happened in this field. The changes of

gasification can be categorized into the following stages and is described by significant time periods in the below sections [10]:

**1850 to 1940.** In this period natural gas production was invented. Before and during this period “town gas” was used to produce light and heat. To produce this gas, gasification of coal is used. In the late 1940s all gas and fuel for streetlights and domestic illumination was produced from the gasification of coal.

**1940 to 1975.** During this period gasification technology was further developed, with many advances occurring post-World War II [11]. It developed more when German engineers used gasification to produce synthetic fuel. Then this technology was exported to South Africa during the 1950s. Once exported to South Africa, the technology was further developed to produce liquid fuels and chemicals.

**1975 to 1990.** After the Arab Oil Embargo of 1973 the next stage in the evolution of gasification began. To ensure that during the “energy crisis” that dependence on foreign energy sources was reduced the U.S. government provided financial support for several proof-of-concept gasification projects, including the world’s first Integrated Gasification Combined Cycle (IGCC) electric power plant.

**1990 to 2000.** This stage of gasification technology development began in the early 1990s when government agencies in the United States and Europe provided financial support to four medium-sized projects to further demonstrate the feasibility of the IGCC process.

**2000 to present.** Commercial developers started building IGCC power plants without government subsidies, the current stage of gasification development began. These new IGCC facilities are adjacent to refineries where petroleum coke and other residual hydrocarbons are readily available.

## **2.2.2 Primary Gasification Technologies**

Primarily modern gasification technologies generally fall into three categories depending upon the flow conditions in the gasifier, moving bed, entrained flow, and fluidized bed. Subsequent sections in this chapter will briefly describe each gasification technology.

### **2.2.2.1 Moving bed**

In this type of bed, the carbonaceous fuel is dry-fed through the top of the reactor and as the fuel slowly falls, it reacts with the gasifying agents flowing in a counter-current through the bed. The fuel goes through the various stages of gasification until it is ultimately consumed, leaving only syngas and a dry or molten ash. The syngas has a low temperature around 400-500°C and contains significant quantities of tars and oils when this configuration is used.

### **2.2.2.2 Entrained flow**

In the entrained flow unit the fuel and gasifying agents flow in the same direction. The feedstock which may be dry-fed or wet-fed, goes through the various stages of gasification as it moves with the steam/oxygen flow. The syngas exits through the top of the reactor and the ashes flow down the sides as a molten slag, which is removed from the bottom. In this type of gasification technology operating temperatures are very high around 1200-1600°C.

### **2.2.2.3 Fluidized bed**

The fuel, introduced into an upward flow of steam/oxygen, remains suspended in the gasifying agents while the gasification process takes place. Since the operating temperature of the reactor (800-1050°C) is less than the temperature at which the ashes from the fuel melt, these can be removed either in dry form or as agglomerate [10]. For this research a laboratory scale fluidized bed is used. Different combinations of flow velocity and bed height are used for the research purposes. Further details of this type of gasifier are provided in the next section.

## **2.3 Fluidization**

Fluidization is a process in which solids behave like a fluid when blowing gas or liquid flowing upwards through the solid-filled reactor pushes particles upward. Fluidization occurs when a fluid (gas or liquid) is passed up through the granular material in the case of a gas-solid bed. Fluidization is widely used in commercial operations; the applications can be roughly divided into two categories,

- Physical operations, such as transportation, heating, absorption, mixing of fine powder, etc.
- Chemical operations, such as reactions of gases on solid catalysts and reactions of solids with gases etc.

The fluidized bed is one of the best known contacting methods used in the processing industry, for instance in oil refinery plants. Among its chief advantages are that the particles are well mixed leading to low temperature gradients, they are suitable for both small and large scale operations and they allow continuous processing. There are many well established operations that utilize this technology, including cracking and reforming of hydrocarbons, coal carbonization and gasification, ore roasting, Fisher-Tropsch synthesis, coking, aluminum production, melamine production, and coating preparations. The application of fluidization is also well recognized in nuclear engineering as a unit operation for example, in uranium extraction, nuclear fuel fabrication, reprocessing of fuel and waste disposal.

### **2.3.1 Fluidized Bed**

A fluidized bed is formed when solid particles are placed under appropriate conditions, with the introduction of the fluid flow the after reaching a certain limit the bed act as a fluid. In this type of bed high velocity of upward flow of gasifying agent introduced to the feedstock.

Upward flow makes suspends the solids and various stages of gasification take place. This type of bed provides back mixing, which mixes the new feed coal with undergoing gasification coal. Usually less than 6 mm particle sizes are used to maintain suspension of particles into the bed. Fluidized beds operate at significantly high temperatures for acceptable carbon conversion rate but less than ash fusion temperature to avoid clinker and de-fluidization of bed. This type of gasifier is suitable for coal and other type of fuel like biomass. Escudero et al. describes there are several advantages of fluidized beds as chemical reactors it includes a high rate of heat and mass transfer, low pressure drops, and uniform temperature distribution. As stated before, there are several types of fluidized beds; the most common types are the Stationary Fluidized Beds (SFB) or Fixed Fluidized Beds (FFB) and Circulating Fluidized Beds (CFB). SFB or FFB refers to fluidized beds where the particles remain inside the fluidized bed [12].

### **2.3.2 Fluidization Regimes**

Number of distinct flow regimes are shown by gas-solid fluidized bed. With the increase of superficial velocity the flow regime changes. There are six different regimes found in gas-solid flow. These are delayed bubbling or minimum fluidization or fixed bed, bubbling regime, slugging regime, turbulent regime, fast fluidization, and pneumatic conveying. Fig. 2.2 shows the schematic representation showing appearance of flow regimes relevant to gas-solid fluidization. Escudero [12] described the phenomena of the fluidization regimes, in the first bed column in Fig. 2.2 the delayed bubbling or minimum fluidization or fixed bed regime the air flow across the bed does not have enough velocity to move the particle upward so the bed remain fixed. With the increase of the superficial velocity the bed reaches to bubbling fluidization, bubble starts to form and coalesce engender solid-fluid mixing; the velocity at which bubbles start to form is called minimum bubbling fluidization velocity. Yang [13] considered that the slugging regime appears

in beds where the bed height ( $H$ ) over the bed diameter ( $D$ ) is larger than 2. It ascertain that bubbles have enough time to coalesce in bigger bubbles called slugs, when the bubbles grow to  $2/3$  of the bed diameter the system enters to a slugging regime. Turbulent fluidization occurs when superficial gas velocity ( $U_g$ ) increases and reaches to critical velocity ( $U_c$ ). The critical velocity delimits the onset of turbulent regime. When turbulent fluidization occurs bubbles or slugs begins to breakdown instead of continuing to grow. It is usually determined experimentally as the superficial gas velocity at which the standard deviation of pressure fluctuations reaches a maximum. Fast fluidization occurs when superficial gas velocity ( $U_g$ ) increases beyond the transport velocity ( $U_{tr}$ ). Solid particles are thrown outside of the bed which makes the bed surface unable to distinguish. When the superficial gas velocity is much higher than the transport velocity pneumatic conveying regime is reached. This regime is characterized by the particle being transported out of the bed in a dilute phase.

## **2.4 Gas-Solid Fluidized Bed**

A gas-solid fluidized bed is used for this project. In gas-solid fluidized bed solid particles are suspended by gas. There are many parameters used to characterize the behavior of the gas-solid fluidized bed, among them pressure drop and minimum fluidization velocity are the primary parameters used to characterize the behavior of the fluidized bed.

### **2.4.1 Pressure Drop**

The gas-solid fluidized bed is filled with solid particles usually packed together near the bottom of a column. Flow of the gasifying agent passes through the packed bed and the gas flow experiences a resistance. For the flow of the gasifying agent the resistance through the bed is mainly due to the drag force acting on the particles as the flow passes over them. For passing the

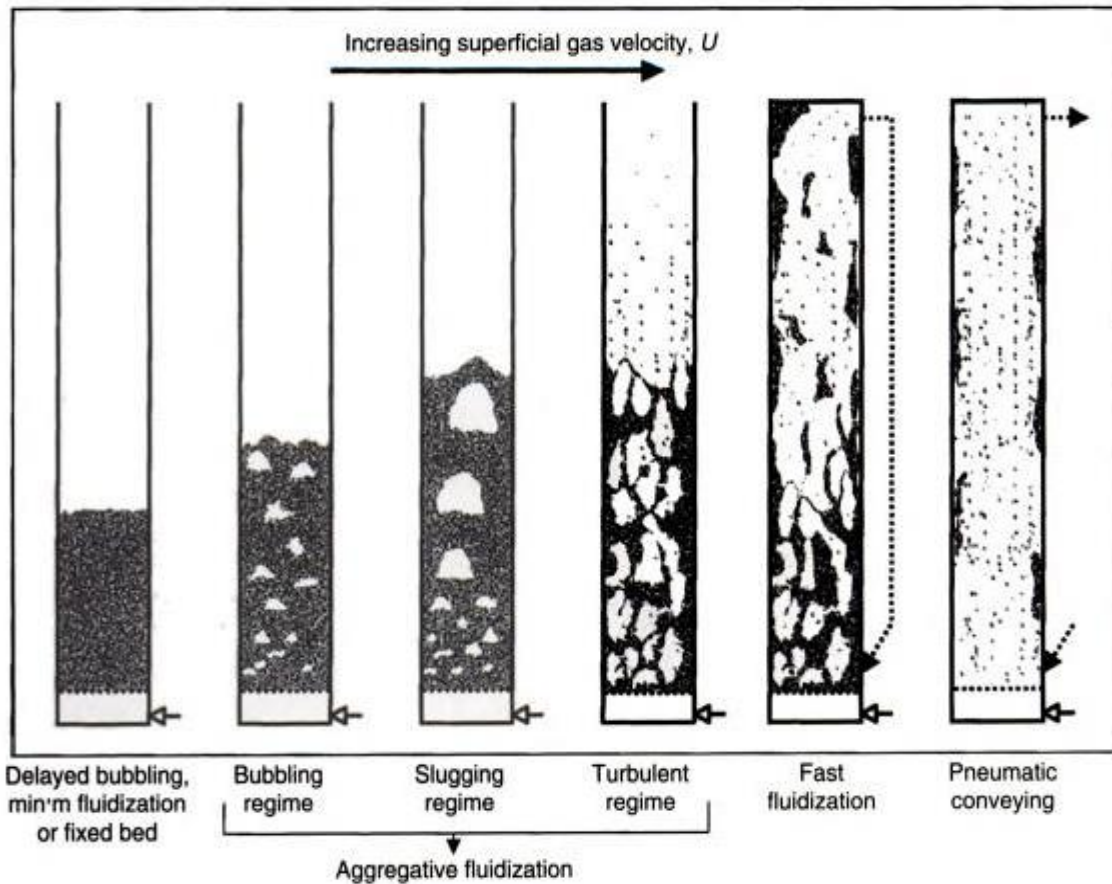


Figure 2.2: Schematic representation showing appearance of flow regimes relevant to gas-solid fluidization [14]

flow at a specified flow rate through bed for proper mixing both gas and solid phase a pressure drop is required. This pressure drop through bed is measured from the total drag force exerted by the solid particles. Niven et al. [15] describes that It is that the pressure loss during one-dimensional flow through a packed bed of granular material is given by the sum of two terms: a viscous energy loss term, proportional to the fluid velocity, and an inertial loss term, proportional to the velocity squared.

$$\frac{\Delta P}{L} = aU + bU^2 \quad (2.1)$$

where,  $\Delta P$  = Pressure Drop;  $L$  = Bed height;

$U$  = Superficial fluid velocity

$a$  and  $b$  are emperical parameters

One form of this equation is widely used by engineers which was given by a famous scientists named Sabri Ergun. On 1952 Ergun expressed bed frictional factor as a function of Reynolds number to measure the bed pressure drop.

$$f_p = \frac{150}{Re} + 1.75 \quad (2.2)$$

Where,

$$f_p = \left(\frac{\Delta P}{L}\right) \left(\frac{D_p}{\rho V_s^2}\right) \left(\frac{\varepsilon^3}{1 - \varepsilon}\right) \quad (2.3)$$

$$Re = \frac{D_p V_s \rho}{(1 - \varepsilon) \mu} \quad (2.4)$$

Here,

$\Delta P$  = Pressure Drop

$L$  = Length of the Bed

$D_p$  = Diameter for spherical particles

$\rho$  = Fluid density

$\mu$  = Dynamic Viscosity of Fluid

$\varepsilon$  = Void Fraction

$V_s$  = Superficial Gas Velocity

Plugging in the value of frictional factor and Reynolds number from Eqs. 2.3 and 2.4, in Eq. 2.2, the bed pressure drop comes as follows,

$$\Delta P = \frac{150(1 - \epsilon)^2 \mu}{D_p^2 \epsilon^3} L V_s + \frac{1.75 \rho_f (1 - \epsilon)}{D_p \epsilon^3} L V_s^2 \quad (2.5)$$

Changing in pressure drop in Eq. 2.5 is subjected to solid particles equivalent diameter ( $D_p$ ) and void fraction of the bed ( $\epsilon$ ).

The Eq. 2.5 is Ergun equation. The sphericity term is included for the non-spherical particles in the equation. In this equation,  $D_p$  is the diameter of spherical particles. But for non-spherical particles, their equivalent diameter was used where,  $D_{eq} = \phi \times D_{sd}$ . Here  $D_{sd}$  is the Sauter-mean diameter [16]. For non-spherical particles the bed pressure drop equation will be,

$$\Delta P = \frac{150(1 - \epsilon)^2 \mu}{D_{eq}^2 \epsilon^3} L V_s + \frac{1.75 \rho_f (1 - \epsilon)}{D_{eq} \epsilon^3} L V_s^2 \quad (2.6)$$

#### 2.4.2 Minimum Fluidization Velocity

When the superficial velocity is exerted at the beginning, the fluidization or minimum fluidization velocity the upward force by flow is equal to the gravitational force exerted by bed particles. Pressure drop across bed is equal to total weight of bed particle per unit area of cross section [17].

Minimum fluidization velocity can be calculated by balancing net weight of bed particle by upward flow force of gasifying agent.

$$\text{Upward force} = \Delta P \times A$$

$$\text{For a fixed bed height (L) with void fraction } (\epsilon), \text{ volume of particles} = (1 - \epsilon) A \times L$$

$$\text{Net weight of particles} = (1 - \epsilon) \times (\rho_p - \rho_f) A \times L \times g$$

Here,

$\rho_p, \rho_f, g$  are density of particles, gasifying agent and gravitational force respectively.

By balancing net weight of particles and upward force

$$\Delta P = (1 - \epsilon) \times (\rho_p - \rho_f) L \times g$$

Using the value of pressure drop  $\Delta P$  in Eq. 2.5

$$1.75 D_p \rho_f V_{mf}^2 + 150(1 - \epsilon) \mu V_{mf} = (\rho_p - \rho_f) D_p^2 g \epsilon^3 \quad (2.7)$$

At the balancing point of total bed weight and upward force the superficial gas velocity ( $V_s$ ) is referred as minimum fluidization velocity ( $V_{mf}$ ).

### 2.4.3 Void Fraction

Void fraction is one of the most important parameters to design the fluidized beds. It is the measure of the void spaces in materials, and is a fraction of the volume of voids over the total volume, between 0 and 1, or as a percentage between 0 and 100. Packing characteristic is an indispensable parameter to design and operate the packed fluidized bed. The bed is made densely packed in our experiment. It is done by pouring the particles into the bed and shaking it for several minutes. Respective authors ranged the voidage 0.37 to 0.39 for dense packed bed of mono-sized spherical particles [13].

Table 2.1: Voidage of Randomly Packed Beds with uniformly sized Particles Larger than 500  $\mu\text{m}$ . (Packing of Non-Spherical particles) [14]

Sphericity	Voidage	
	Loose Packing	Dense Packing
0.25	0.85	0.8
0.3	0.8	0.75
0.35	0.75	0.7
0.4	0.72	0.67
0.45	0.68	0.63
0.5	0.64	0.59
0.55	0.61	0.55
0.6	0.58	0.51
0.65	0.55	0.48
0.7	0.53	0.45
0.75	0.51	0.42
0.8	0.49	0.4
0.85	0.47	0.38
0.9	0.45	0.36
0.95	0.43	0.34
1	0.41	0.32

#### 2.4.4 Hydrodynamics Behavior of Fluidized Bed

Due to numerous applications, hydrodynamic behavior of fluidized bed has become an area of interest for the researchers. This is a widely used technology in industries for various purposes. Particle size, particle shape, bed diameter, bed height, minimum fluidization velocity are the important parameters in determining the hydrodynamic behavior of the fluidized bed. Numerous studies are found in literature about the hydrodynamic behavior of the fluidized bed. Bed height is an important parameter in determining the behavior of the fluidized bed. Rectangular bed (2D) and cylindrical bed (3D) was used by Geldart et al. [18] to analyze the effect of the bed height. For both 2D and 3D fluidized bed six different bed heights were used and no effect on minimum fluidization velocity on increasing bed height for cylindrical fluidized bed is found from their investigation. The effect of particles diameter and bed height on minimum fluidization velocity for cylindrical shaped fluidized bed is investigated by Gunn et al.

[19]. They also did not find any significant effect of bed height on minimum fluidization velocity. The scenario of the minimum fluidization velocity and bed diameter for the rectangular bed is different from the circular fluidized bed. Hilal et al. [20] investigated the minimum fluidization velocity for two fluidized bed with different diameters (0.29 m and 0.089 m). They found that minimum fluidization velocity decreased with the increase of bed diameter. One of the important parameters of the fluidized bed is minimum fluidization velocity. Hilal et al. analyzed the effects of bed diameter, gas distributor, and inserts on minimum fluidization velocity. Lin et al. showed that the minimum fluidization velocity for increasing fluidization and defluidization indicates that the  $U_{mf}$  for increasing fluidization was typically higher than at defluidization [21]. Caicedo et al. [22] used rectangular bed (2D) with dimensions of 1 x 0.2 x 0.012 m and different ranges of particles (160-250, 250-400, 490-700  $\mu\text{m}$ ) at different bed heights and at different bed widths. According to the authors the minimum fluidization velocity increased with the increase of bed height, particle diameter and decreases with the increase of column width. Zhong et al. [23] used Geldart Type-D particles at different heights in a spouted fluidized bed with dimensions of 300 mm  $\times$  300 mm and 2000 mm height. The authors found that the influence of static bed height on the minimum fluidization increases with the increase of bed height. They also determined that for different densities the pressure drop and minimum fluidization velocity significantly changes based on the density of particles used. Sau et al. determined that the total pressure drop increased with the increase of superficial gas velocity [24]. Rao et al. [25] used two fluidization segregation units with a 1.6 cm and 2.4 cm column diameter. In their experiment they used glass beads with a particle range of 100-600 $\mu\text{m}$  and 2500 kg/m<sup>3</sup> density. They found that minimum fluidization velocity is influenced by bed diameter and bed height. Minimum fluidization decreased with an increase of bed diameter and increased with

increase of bed height. Escudero [26] proposed that bed pressure drop increased when the ratio of bed height and diameter increased. This effect was found to be related to the bulk density and mass of the material. In their investigation, they found that each type of particle has no influence in minimum fluidization velocity with increasing height and minimum fluidization velocity influenced by particles density. It increases with increase of particle density.

## **2.5 Drag Force & Drag Correlation**

Drag is a kind force which acts opposite to the relative motion of any object moving with respect to a surrounding fluid. It can exist between two fluid layers or surfaces or a fluid and a solid surface. This is one of the most fundamental parameters to characterize the behavior of the fluidized bed. Dissimilar other resistive forces, such as dry friction, which are nearly independent of velocity, drag forces depend on velocity. Drag forces always decrease fluid velocity relative to the solid object in the fluid's path. Brucato et al. [27] presented a new experimental technique for measuring average particle drag coefficients in turbulent media. It is based on a direct measurement, by means of a suitable residence time technique, of the settling velocity exhibited by a cloud of particles. Chhabra et al. [28] evaluated a selection of widely used correlations for estimating the drag coefficient of non-spherical particles in incompressible viscous fluids. Experimental results have been culled from 19 independent studies embracing wide ranging particle shapes including cylinders, needles, cones, prisms, discs, rectangular, parallelepiped and cubes. Ceylan et al. [29] found drag correlation for the spherical solid particles which can determine the drag coefficient of the of the non-spherical particles for Reynolds number,  $Re$  up to  $Re < 1000$ , for the liquids with a flow behavior index,  $n$ , in the range of  $0.5 < n < 1$  (where  $n=1$  for Newtonian liquids). Tran-Cong et al. [30] measurements the drag coefficients for six different geometrical shapes, including isometric, axisymmetric, orthotropic, plane and elongated

conglomerates of spheres. From these measurements, a new and accurate empirical correlation for the drag coefficient,  $C_D$ , of variously shaped particles has been developed. Yow et al. [31] developed an explicit equations to characterize the effects of sphericity and Reynolds number of a particle on its drag coefficient. Various studies about the drag correlation of the spherical particles are found in literature, on the other hand for the non-spherical particle it is modicum. Many studies found in literature about the spherical and the non-spherical particles produces inexact results if those correlation are used. So, finding accurate correlation of the drag force of the non-spherical particle is necessary to predict behavior of the fluidized bed and for the other applications. This thesis is focusing on determining the drag correlation of the non-spherical particles and implementing in computational code. Scientists are working on finding the drag correlation of the spherical and the non-spherical particles in many aspects, such as for different ranges of Reynolds number and fluid properties. Loth et al. [32] reviewed and investigated the drag of a non-spherical particle for a variety of shapes (regular and irregular) and particle Reynolds numbers. Point-force models for the trajectory-averaged drag were discussed for both the Stokes regime ( $Re \ll 1$ ) and Newton regime ( $Re \gg 1$  and sub-critical with approximately constant drag coefficient) for a particular particle shape. Hsu et al. [33] examined the influences of the particle concentration, the nature of the Carreau fluid, and Reynolds number, on the drag coefficient. It shows that the drag coefficient declines with the decreasing particle concentration, and the reversal of the flow field in the rear region of a sphere is enhanced by the shear-thinning nature of the fluid. Gabitto et al. [34] developed an explicit equations for the drag coefficient and the terminal velocity of free-falling solid particles of cylindrical shape. Zastawny et al. [35] derives and validates a new framework to predict the drag and lift coefficients as well as the torque coefficients for four non-spherical particle shapes in a flow with a wide range of flow  $Re$

and rotational Re numbers. Each of the correlations depends on Re number, the dimensionless rotation and the angle of incidence between the particle and the direction of the local fluid velocity. Terfous et al. [36] established a relationship based on the characteristics of both the fluid and the particles to calculate directly the settling velocity of a spherical particle in a fluid at rest. The settling velocity values obtained with the proposed relationship were validated using experimental data and the model proved to be reliable and precise. Barati et al. [37] presents development of high accurate drag coefficient correlations from low to very high Reynolds numbers (up to  $10^6$ ) using a multi-gene Genetic Programming(GP) procedure. Table 2.2 summarizes some of the drag correlation of the non-spherical particles.

Table 2.2: Summary of select non-spherical drag coefficients available in literature

Reference	Drag Correlation	Parameters
Haider and Levenspiel (1989) [38]	$C_D = \frac{24}{Re} (1 + A Re^B) + \frac{C}{1 + \frac{D}{Re}}$ $A = \exp (2.3288 - 6.4581\phi + 2.4486\phi^2)$ $B = 0.0964 + 0.55.65\phi$ $C = \exp (4.905 - 13.8944\phi + 18.422\phi^2 - 10.2599\phi^3)$ $D = \exp (1.4681 + 12.2584\phi - 20.7322\phi^2 + 15.8855\phi^3)$	Poor prediction for particles with $\phi < 0.67$
Ganser (1993) [39]	$C_D = \frac{24}{Re K_1 K_2} [1 + 0.118 (Re K_1 K_2)^{0.65657}]$ $+ \frac{0.4305}{1 + \frac{3305}{Re K_1 K_2}}$ <p>Isometric Shapes:  <math>K_1 = [(1/3) + (2/3)\phi^{-0.5}]^{-1}</math>  <math>K_2 = 10^{1.8148(-\log \phi)^{0.5743}}</math></p> <p>Isometric Shapes:  <math>K_1 = [(1/3) + (2/3)\phi^{-0.5}]^{-1}</math>  <math>K_2 = 10^{1.8148(-\log \phi)^{0.5743}}</math></p>	Assumes every particle experiences a Stokes' regime where drag is linear in velocity and a Newton's regime where drag is proportional to the square of the velocity

Reference	Drag Correlation	Parameters
Chien (1994) [40]	$C_D = \frac{30}{Re} + 67.289 \exp(-5.03\phi)$	$0.2 \leq \phi \leq 1$ $Re < 5000$  Over prediction of drag for spheres especially in creeping flow regime
Tran-Cong et al. (2004) [30]	$C_D = \frac{24}{Re} \frac{d_A}{d_n} \left[ 1 + \frac{0.15}{\sqrt{c}} \left( \frac{d_A}{d_n} Re \right)^{0.687} \right]$ $+ \frac{0.42 \left( \frac{d_A}{d_n} \right)^2}{\sqrt{c} \left[ 1 + 4.25 \times 10^4 \left( \frac{d_A}{d_n} Re \right)^{-1.16} \right]}$ <p> <i>d<sub>A</sub> = Surface equivalent sphere diameter</i>  <i>d<sub>n</sub> = Nominal diameter</i>  <i>c = Particle circularity</i> </p>	$0.15 < Re < 1500$ $0.80 < d_A/d_n < 1.50$ $0.4 < c < 1.0$
Holzer and Sommerfeld (2008) [41]	$C_D = \frac{8}{Re} \frac{1}{\sqrt{\phi_{\parallel}}} + \frac{16}{Re} \frac{1}{\sqrt{\phi}} + \frac{3}{\sqrt{Re}} \frac{1}{\phi^{3/4}}$ $+ 0.4210^{0.4(-\log \phi)^{0.2}} \frac{1}{\phi_{\perp}}$	Accounts for particle orientation relative to flow field

## 2.6 Non-Linear Regression

Nonlinear regression is a kind of regression analysis in which observational data are modeled by a function which is a nonlinear combination of the model parameters and depends on one or more independent variables. Brown et al. introduced a simple, easily understood method for carrying out non-linear regression analysis based on user input functions. While it is relatively straightforward to fit data with simple functions such as linear or logarithmic functions, fitting data with more complicated non-linear functions is more difficult [42]. This tool is very essential for modelling different kinds of scientific phenomena. Brown et al. [43] demonstrated a method for fitting complex electrophysiological data with multiple functions using the SOLVER add-in of the ubiquitous spreadsheet Microsoft Excel. Tsekouras et al. [44]

described a non-linear multivariable regression method for midterm energy forecasting of power systems in annual time base. This method performs an extensive search in order to select the appropriate transformation functions of input variables, the weighting factors and the training periods to be used, by taking into consideration the correlation analysis of the selected input variables. With this procedure the best forecasting model is formed. In our case, non-linear regression is used to create a correlation between drag force and Reynolds number, which is an integral part of this project. Terminal velocity of the particles is measured from the experiment and using this drag force and Reynolds number are found. From there using MATLAB code the correlation between drag force and Reynolds number is found. This is one of the most unique feature of this research project.

## **Chapter 3 : Experimental Setup & Technical Approach**

This section of the thesis will describe the experimental set up, test matrix, and technical approach to run the experiments. Section 3.1 will describe the all the components of the fluidized bed used to validate the computational model, section 3.1.1 will describe about the previous experimental set up that was used. The production of test material will be described in section 3.2. Productions of non-spherical particles will the described in section 3.2.1. Section 3.2.2 will describe the categorization of Particles Size and Shape. Section 3.2.3 will explain the sphericity measurement of the particles. Bed pressure drop and flow rate measurement are explained in section 3.3. High speed flow field visualization is an important part of the thesis which is discussed on section 3.4. Section 3.5 discusses about the Shadow sizing technique, section 3.5.1 explains about the shadow sizing measurement principle, section 3.5.2 talks about the calibration of the shadow sizing measurement, and section 3.5.3 discusses about the shadow sizer processing.

### **3.1 Experimental Set up**

The experimental fluidized bed set up will be described in this section. The schematic diagram of a laboratory scale gas solid fluidized bed is shown in Fig. 3.1. The experimental set up consists of a blower, butterfly valve, fluid delivery channel, flow meter, flow distributor, digital manometer, quartz tube, test particles, mash catch, computer for data processing. To supply air to the gasifying agent a high-pressure blower with 3730 KW and 34 m<sup>3</sup>/min flow rate has been used.

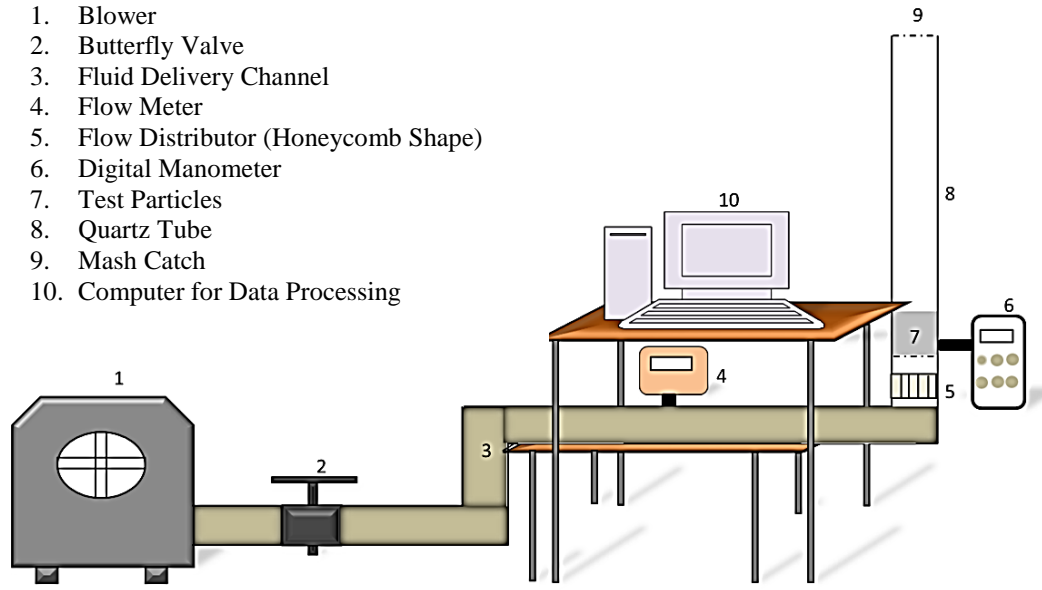


Figure 3.1: Schematic Diagram of Laboratory Scale Fluidized Bed

With the 300 cm long and 12.7 cm diameter sheet metal pipe with three elbows the air was supplied to the test section.

To meet the requirement recommended by the manufacturer this length and elbows were used flow meter which was recommended to get the proper flow rate reading through the cross section of sheet metal pipe. The outlet of the blower is rectangular in shape. A duct reducer with  $12.7 \times 17.8$  cm rectangular to 10.2 cm circular duct was used and connected from blower outlet to sheet metal pipe inlet to fit into the outlet of the blower. A wafer style butterfly valve with 12.7 cm diameter and 5.7 cm thickness was used to control the flow rate to the test section, which is connected between the blower and first elbow among the three. To measure flow rate across the bed a thermal mass flow meter was used between second and third elbow. The distance between elbows and flow meter was maintained as flow meter manufacturer requirement.

A quartz tube with 12 cm outer diameter and 0.318 cm wall thickness was inserted into in to the plexi glass tube, which is the bottom part of the test section. This bottom section is made of plexi glass tube with 12.7 cm outer diameter and 3.18 m wall thickness. The quartz tube will assist to attain better optical access for particle image velocimetry (PIV) and also for shadow sizing analysis for dilute part of test section during experiment.

A mesh made of brass with 53 micron was installed at the bottom of the test section to hold particles and another mesh with same type was also installed at top part of bed column section to hold the particle from falling out of the bed column. A small opening was made at 1.5 cm above from bottom of test section to measure the pressure drop across the bed. A tygon tube from digital manometer was connected to that small opening and a small part of mesh with 53 micron was attached to that small opening to restrain the particle entering into tube. For uniform distribution of gasifying agent (air) to the test section a honeycomb shape distributor was inserted 8 cm below from test section to maintain a uniform distribution of gasifying agent (air). For thermal mass flow meter an external power supply was used.

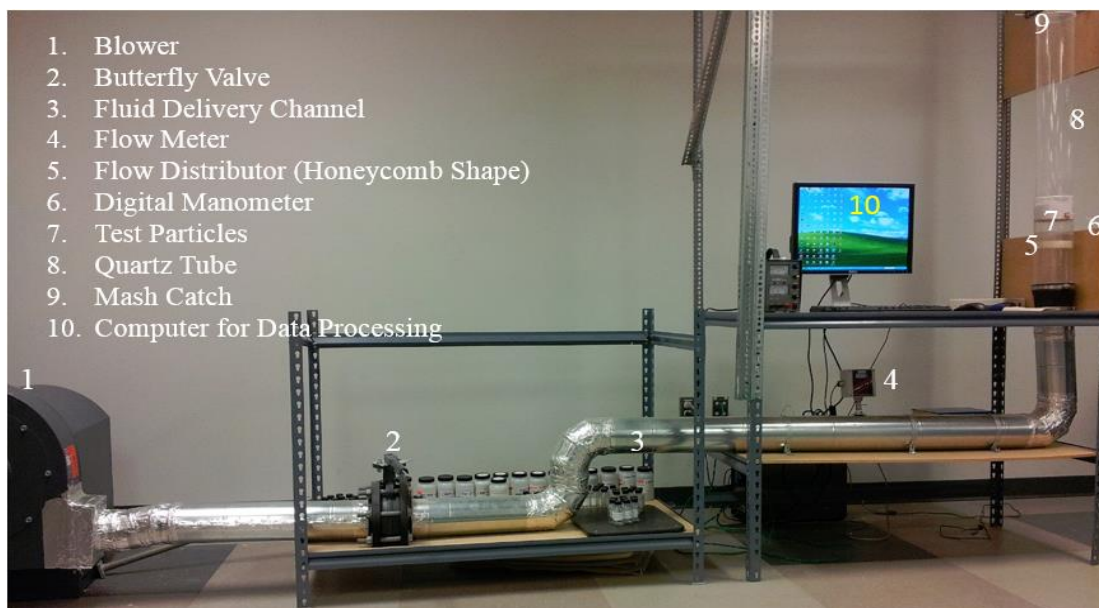


Figure 3.2: Laboratory Scale Fluidized Bed

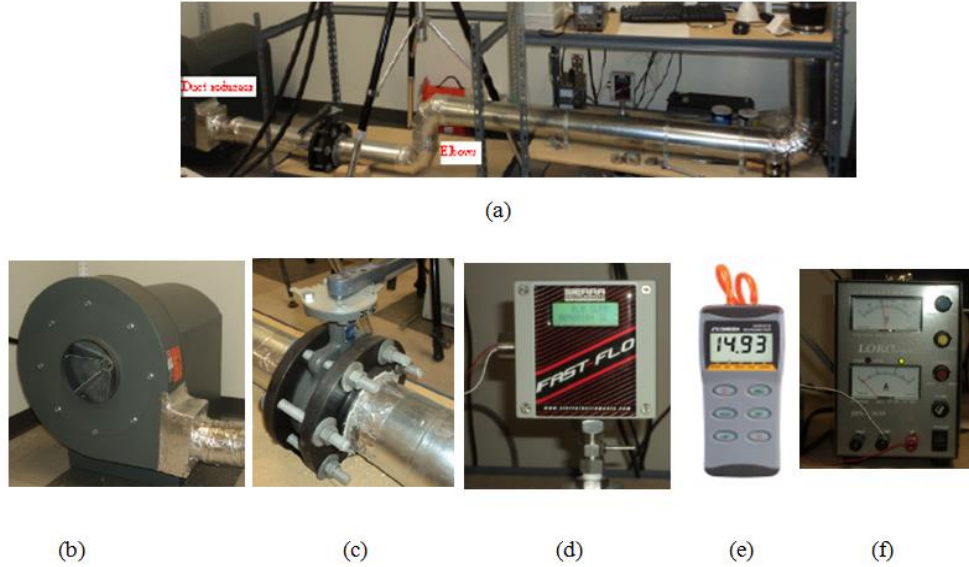


Figure 3.3: (a) Air Delivery System (b) High Pressure Blower (c) Butterfly Valve (d) Thermal Mass Flow Meter (e) Digital Differential Manometer (f) External Power Supply

### 3.2 Test materials

Borosilicate glass beads with density  $2230 \text{ kg/m}^3$  and Canadian Hematite with density  $4989 \text{ kg/m}^3$  was selected as test material to investigate the hydrodynamics of fluidized bed. For the experiment both spherical and non-spherical particles are selected. Initially, spherical particles for were chosen but in reality all the all the particles inside the coal gasification plan are irregular in shape. For our research both spherical and non-spherical particles are selected.

1 mm borosilicate glass beads with density  $2230 \text{ kg/m}^3$  are selected for spherical particles. A sample of spherical particles image is shown in Fig. 3.5.



Figure 3.4: Zoomed Image of 1 mm Spherical Particles

### **3.2.1 Production of Non-Spherical Particles**

Non spherical particles of 6 mm borosilicate glass beads were crashed by a CRAVER 3851 hydraulic compressor to produce the non-spherical particles. A die and punch system with 5.08 cm diameter was used to put the spherical particles and then crushed into hydraulic compressor. The stainless steel die and punch used here, is capable to withstand high pressure exerted by hydraulic compressor.

The particles crushed for the experiment had different size ranges from few microns to large irregular shape. If the particles were larger then it is required than the particles were crushed again. An Octagon digital with 60 Hz, 110 volts, single phase sieve shaker was used with mounting different sieve plate into the sieve shaker to categorize the particles in desired particle size distribution. Ranges of sieve plates were 20 $\mu$ m to 2000 $\mu$ m. A precision weighing balance was used with capacity 620g and readability 0.001 g to measure the particle weight.

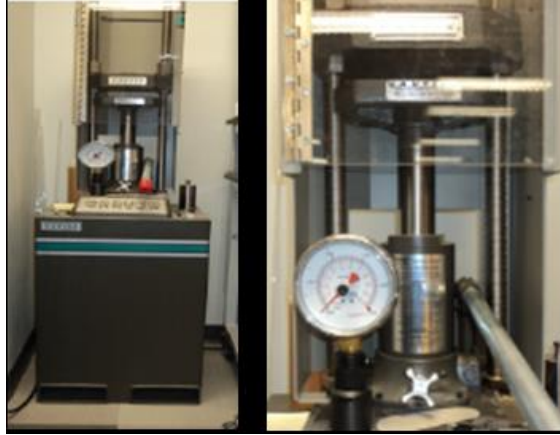


Figure 3.5: CRAVER 3851 Hydraulic Compressor

### 3.2.2 Measurement of Particle Size and Shape

The aggregate particle materials have many industrial applications. The particle size and shape is important to get optimum operation process, measurement.

Mechanical sieving technology is one of the most widely used methods for grading aggregate particles distribution. The aggregate particles are divided into fractions by Sieving method where each fraction contains a certain range of particle size.

The sieves are arranged by putting them one after another from lower range to higher range. To hold the powder like particles a pan was placed at the bottom. Then the stacked sieve placed into sieve shaker. Sample of aggregate particles put into top larger sieve pan and a cover is placed on top of that. Sieve shacking was carried out for specific period of time. Particles pass gradually from larger sieve aperture to lower sieve aperture. Finally, fraction of particles from each sieve was weighing by a precision balance with capacity 620 gm. and readability 0.001 gm.

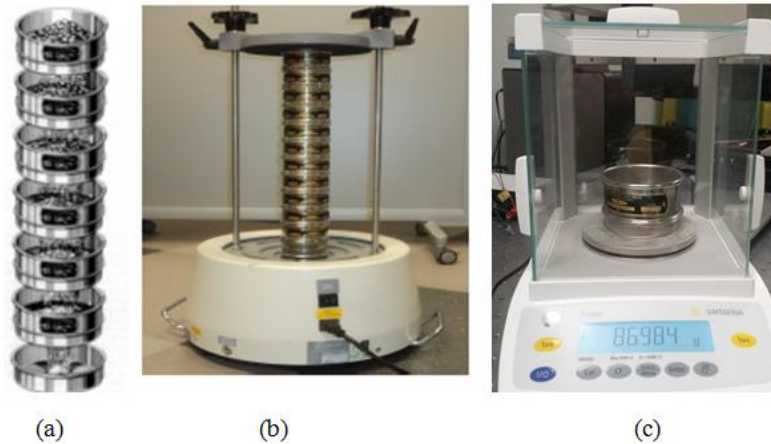


Figure 3.6: (a) Stack of Sieve Pan (b) Sieve Shaker (c) Precision Balance

### 3.2.3 Sphericity Measurement

Digital Image Processing (DIP) is a method of image processing which uses computer algorithm on digital images. It allows the use of much more complex algorithms, and hence, can offer both more sophisticated performance at simple tasks, and the implementation of methods which would be impossible by analog means. This technology has widespread application in medicine, biology, geography, meteorology, manufacturing, material science. Size and shape analysis is very important for particulate technology. It can also be used for size and shape analysis beyond the recent use of DIP technology [45]. Instead of processing the digital image we used to take digital image and find out the larger circumscribe circle of the particle by using software provided with DinoLite, the versatile digital microscope.

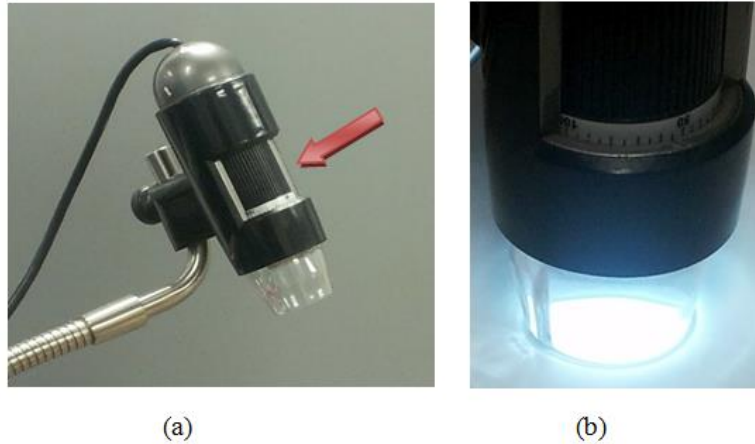


Figure 3.7: (a) Dino Capture Microscope (b) Focusing the Particles

The object was focused by adjusting the dial with microscope and then the image was captured. At time of adjusting the dial, the dial number (magnification value) was noted and put into with magnification window before play with the image to get circumscribe diameter of the particle. Prior to measure the circumscribe diameter of particle standard measurement ruler was used to calibrate the Dino Captured Microscope.

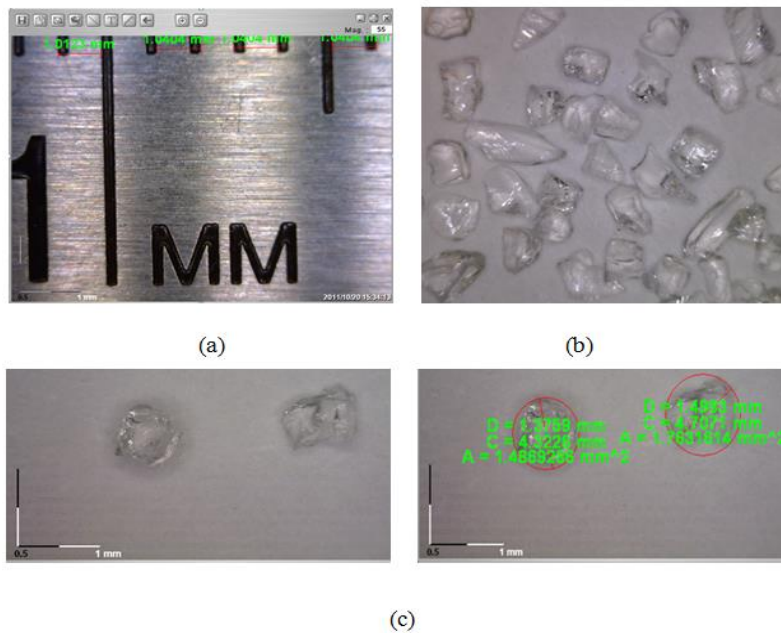


Figure 3.8: (a) Calibration Image (b) Sample Image of Non-Spherical Particle (c) Measurement of Circumscribe Diameter of Non-Spherical Particles

There are various methods of measuring the sphericity of a particle. The expression for sphericity of made by Hakon Wadell [46] is described by W.C. Krumbein [47]. According to Wadell definition sphericity ( $\phi$ ) is as follows,

$$\phi = \sqrt[3]{\frac{\text{Volume of Particle}}{\text{Volume of the Circumscribe Sphere}}}$$

From Wadell expression it can be seen that the particle volume has the same volume in terms of sphere and the diameter is the nominal diameter of the particle ( $d$ ). From this expression the basic volume of particle is  $\frac{\pi}{6}d^3$ . In general, the volume of circumscribe sphere has the longest diameter ( $a$ ) of the particle, so the volume of circumscribe sphere is  $\frac{\pi}{6}a^3$ . From these values the Wadell expression for sphericity comes as follows,

$$\phi = \sqrt[3]{\frac{\text{Volume of Particle}}{\text{Volume of the Circumscribe Sphere}}} = \frac{\frac{\pi}{6}d^3}{\frac{\pi}{6}a^3} = \frac{d}{a}$$

Krumbein used this expression to measure the sphericity of particle where the sphericity is the ratio of nominal diameter and longest diameter of the particle. Slide calipers is used to measure the longest diameter of particles in this case.

Test particles are crushed and they have the size of micro level, we used the digital image technology to get the longest diameter of the particles ( $a$ ) and the nominal diameter was considered as the mean sieve diameter ( $d$ ).

For our project work, to investigate the effect of particle size in fluidized bed, we accumulate different ranges of particles for Glass beads and Hematite.

Sphericity was measured for each particle ranges between 500-1400 micrometer by random selection and the sphericity was found between 0.45 and 0.93. It is also found that mean sphericity of crushed glass particles is 0.65 (Table 3.1).

Table 3.1: Sphericity of Different Shapes, Materials and Commonly Used Pickings [48]

Types of Particles	Sphericity
Sphere	1.00
Cube	0.81
Cylinder	
h=d	0.87
h=5d	0.70
h=10d	0.58
Disks	
h=d/3	0.76
h=d/6	0.60
h=d/10	0.47
Activated Carbon and	0.70-0.90
Coal	0.63-0.73
Cork	0.69
Glass, Crushed, Jagged	0.65
Sand	0.86-0.53
Wheat	0.85
Tugnsten Power	0.89

### 3.2.4 Sets of particles with different sphericity

Different sets of particles are arranged with the ranges of sphericity. One of the primary goals of this project is to implement the sphericity term in to drag model so that the model can determine the drag coefficient for the non-spherical particles. The particles are arranged for the different ranges. For each range of particle sphericity has been measured. Table 3.2 will shows different ranges of particles with the sphericity that has been measured for each range. Fig. 3.2 shows the particles arranged in bottles with different ranges (increasing bottom to up) and sphericity ranges (increasing from left to right).

Table 3.2: Ranges of Particles and Sphericity

Range	Sphericity								
500-600	0.45-0.50	0.51-0.55	0.56-0.60	0.61-0.65	0.66-0.70	0.71-0.75	0.76-0.80	0.81-0.85	0.86-0.90
600-710									
710-850									
850-1000									
1000-1180									
1180-1400									



Figure 3.9: Particles are arranged with different size and sphericity

### 3.3 Bed Pressure Drop and Flow Rate Measurement

A digital manometer capable for measuring differential pressure and also positive or negative gauge pressure was used. To measure bed pressure drop differential pressure option was

selected. A tygon tube with 5 mm inner diameter was connected from manometer to small opening in fluidized bed. This small opening was at 1.5cm above from bottom of fluidized bed. A mesh catch with 53 micron was attached to the opening to protect tube and manometer from entering test particles during experiment. Fig. 3.10 shows pressure measurement port connected with digital manometer. This manometer is capable of measuring between 0-0.014 MPa pressure drop.

Test particles were prepared by adding static guard before experiment. The static guard was used to remove inter particles bonding. Test particles were poured into bed from top opening of bed column and then bed column was shaken several times. This helps particles get more densely packed. Before starting the experiment loosened particles were removed from the test section. For the experiments bed pressure drop was measured at different increasing flow rates of gasifying agent (air). The flow rate was also measured simultaneously along with the pressure measurement. The air flow rate was increased gradually by regulating butterfly valve up to the beginning of separation of test particles in the packed bed. At this condition it was considered the point of minimum fluidization. At the point of minimum fluidization a small bed height increase was observed using high speed imaging. After minimum fluidization, flow rate were increased until they were trapped into top mesh which was connected into top part of bed column. At this condition the particles were entrained and reached their terminal velocity. By this time the fluidized bed had undergone different fluidization regimes described previously.



Figure 3.10: Digital Manometer with RS 232 Cable

Measured values of differential pressure drop were sent to a Handheld Data Logger (Fig. 3.11) by a RS 232 cable. Both the manometer and data logger provided the pressure drop reading up to 3 decimal points with  $\pm 0.3\%$  accuracy.

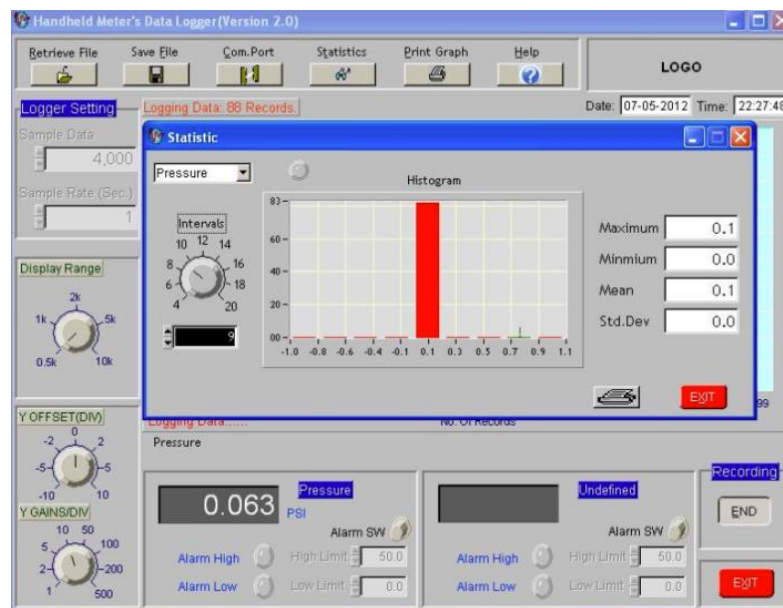


Figure 3.11: Handheld Data Logger for Digital Manometer

The mass flow rate was measured by insertion type mass flow meter with a 200 milliseconds response. The flow meter is shown in Fig. 3.3d was used to measure volumetric flow rate. This flow meter was also factory calibrated to range of 0 to 4000 SLPM. An external power supply with 20 VDC was used to run the flow meter. Data from flow meter was feed into

Sierra Smart Interface software provided by flow meter manufacturer. Fig. 3.12 shows data logger for flow meter.

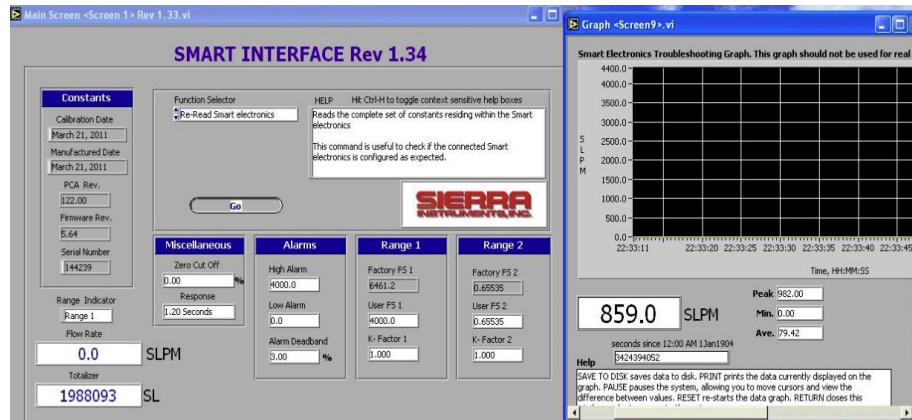


Figure 3.12: Data Logger for Flow Meter

### 3.4 High Speed Flow Visualization

High speed flow visualization has been a very fetching component of scientific visualization research for a long time. Various research groups have been working on flow field visualization because of its numerous applications. Numerous investigations have been observed due to the importance of multiphase flow with their complicated flow structures [49]. Some of the techniques and applications of the high speed flow field visualization from the literature studies is described by Laramée R. et al. [50] who describes flow visualization (FlowVis) as one of the classic subfields of visualization, covering a rich variety of applications, from the automotive industry, aerodynamics, turbo machinery design, to weather simulation, meteorology, climate modeling, ground water flow and medical visualization. Consequently, the spectrum of FlowVis solutions is very rich, spanning multiple technical challenges: 2D versus 3D solutions and techniques for steady or time-dependent data. Sometimes fluids, particles, gases form such complicated patterns that intuition fails when taking image of these cases. Some flows are so intricate that it cannot be analyzed even with the biggest computers available these days. Visual

images of actual flow can advise us of the real flow pattern. Wijk et al. [51] describes a new method for the visualization of two dimensional vector fields in general and fluid flow fields in particular. The method provides a single framework to generate a wide variety of visualizations of flow, varying from moving particles, streamlines, moving textures, to topological images. Fercher A. [52] described a potential application of a technique to the mapping of retinal blood flow. In this technique, a photograph of a flow field is taken under laser illumination. If the exposure is short enough, the velocity distribution in the field will be mapped on the photograph as variations in speckle contrast. These contrast variations can be converted to intensity variations by means of a simple spatial filtering technique, to give a direct picture of the velocity distribution in the flow field. For our research shadowgraphy technology is used. In our current experiment an attempt has taken to observe the flow structure in dilute section while the fluidized bed is fully fluidized. 210 mm above from the top surface of test particles (5.5 cm bed height) was considered as the test section. Also just after the top surface of test particles was considered as test section. At this section collapsing of bubbles were visible. Both spherical and non-spherical particles (1 mm nominal diameter) were taken as test particles.

Dynamic Studio Shadow Sizer measurement technique was used to get particles velocity and particle size for the current experiment. The experimental setup can measure size, shape and velocity of particles using backlighting and image analysis software. The Shadow Sizer can measure a wide range of particles types including bubbles, liquid droplets, solid particles and any object with a well-defined contour. Data is analyzed by DynamicStudio and includes histograms of size distribution, spatial distribution plots, cumulative histograms and tables [53].

### 3.5 Shadow sizing

Shadow sizing is a type of flow visualization. It is an imaging method which enables us to track particles. It reveals non-uniformities in transparent media like air, water, or glass [54]. It uses the color gradient to track something, where color gradient is approximately 90% it considers it as the target object and take the contour of that object. Shadow images of test section with less concentrated particles were captured with high speed camera at 1000 frame per second. Every two consecutive images were processed with commercial software DynamicStudio. The DynamicStudio detects it by selecting threshold level of images, counts and also give the instantaneous velocity of particles.

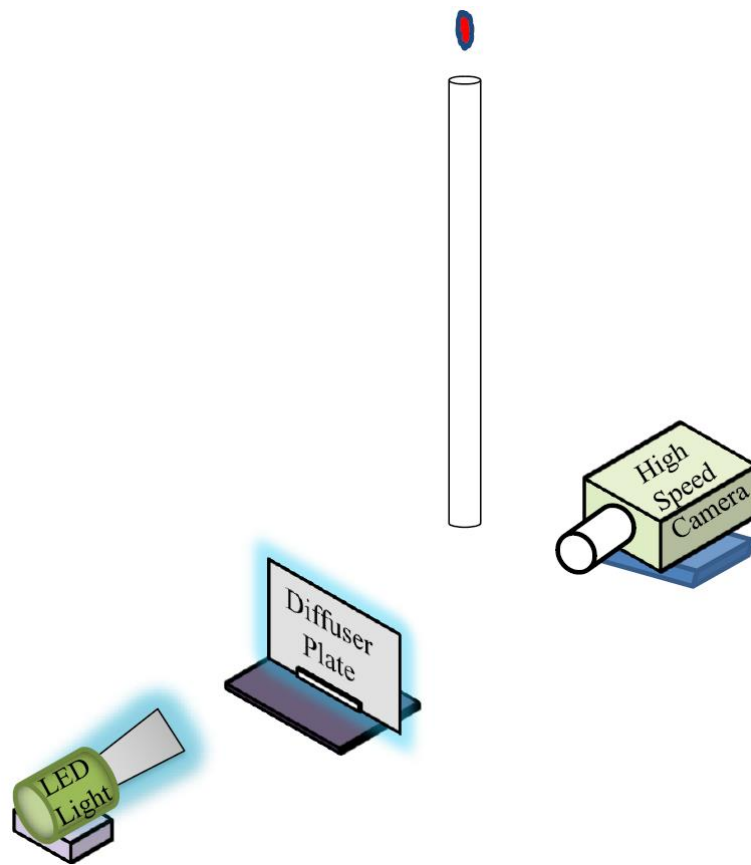


Figure 3.13: Schematic image of Experimental Setup for Terminal Velocity Measurement of Particles

### 3.5.1 Shadow Sizing Measurement Principle

A camera and a light source are required for shadow sizing. A ground glass diffuser plate is also placed between the light source and the test section. This ground glass diffuser helps to take the images of test particles as a shadow. Fig. 3.14 shows the schematic diagram of shadow sizing technology.

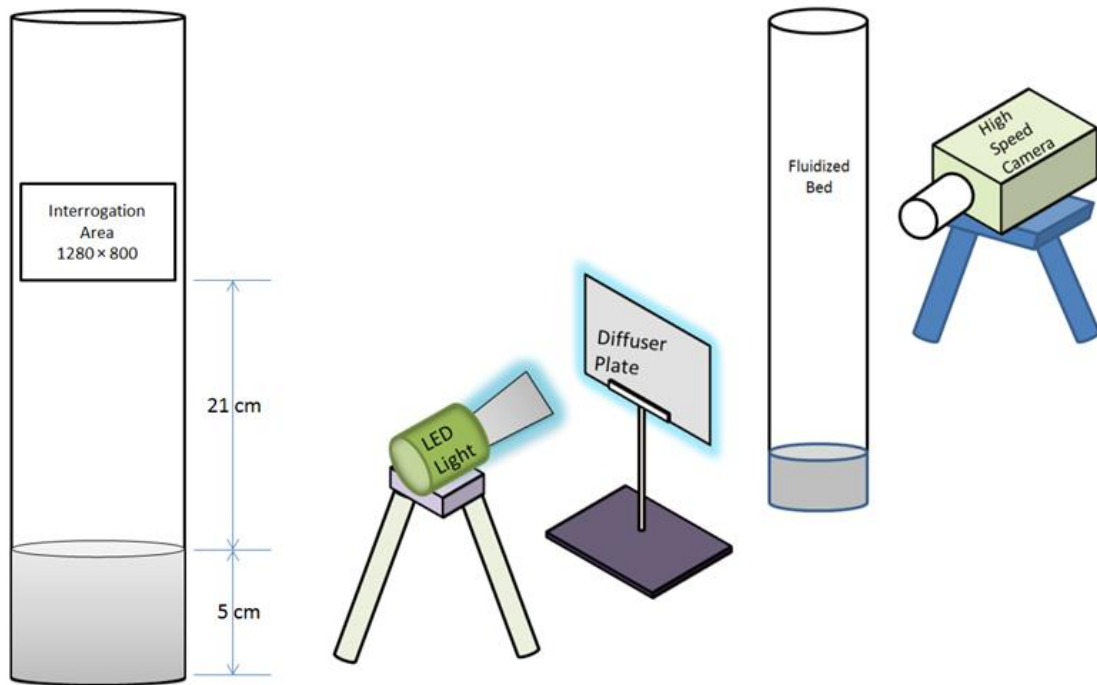


Figure 3.14: Schematic Diagram of Shadow Sizing

For light source LED based honeycomb and constellation illuminator was used with delivering lower to higher luminosity as required to get a perfect shadow image of test section. Fig. 3.14 shows the LED based light source.



Figure 3.15: LED Constellation System

To capture the image a Phantom high speed camera with 5 KHz was used. Image triggering rate can be change by using dynamic studio software. For the current experiment all the images have taken with 1000 Hz. Fig. 3.15 shows the Dantec high speed camera.



Figure 3.16: Dantec High Speed Camera

Both camera and LED light source are synchronized by a timer box. While the particles flows through the test section a light flash acquires and at the same time camera capture the image with help of synchronization device and freeze the particles motions. After acquiring the images shadow sizing software use advanced edge detection algorithm to detect the particles and

their shape. To find out the velocity shadow sizing uses two consecutive images with very short interval and particle tracking algorithm.



Figure 3.17: Shadow Sizing

Again without using the backlit light source (LED light) only high speed camera was used to visualize the fluidized bed test particles behavior. Two state of fluidization were observed for both spherical and non-spherical particles. 1) Incipient of minimum fluidization. 2) Bubbling Fluidization. These two observations will give a fundamental idea about particles behavior for a respective flow velocity of gasifying agent (air).

### 3.5.2 Calibration

Before processing the images it is required to capture a calibration image. A scale factor should measure from that calibration image. Images taken by high speed camera is in pixel unit. To get physical parameter of particles and their velocities in metric unit it is required to convert image from pixel unit to metric unit. A ruler scale is placed in test section and calibration image was taken. From measure scale factor window in dynamic studio software two points were selected and their numeric distance was put as required in metric unit. Fig. 3.17 shows a calibration image taken from dynamic studio software.

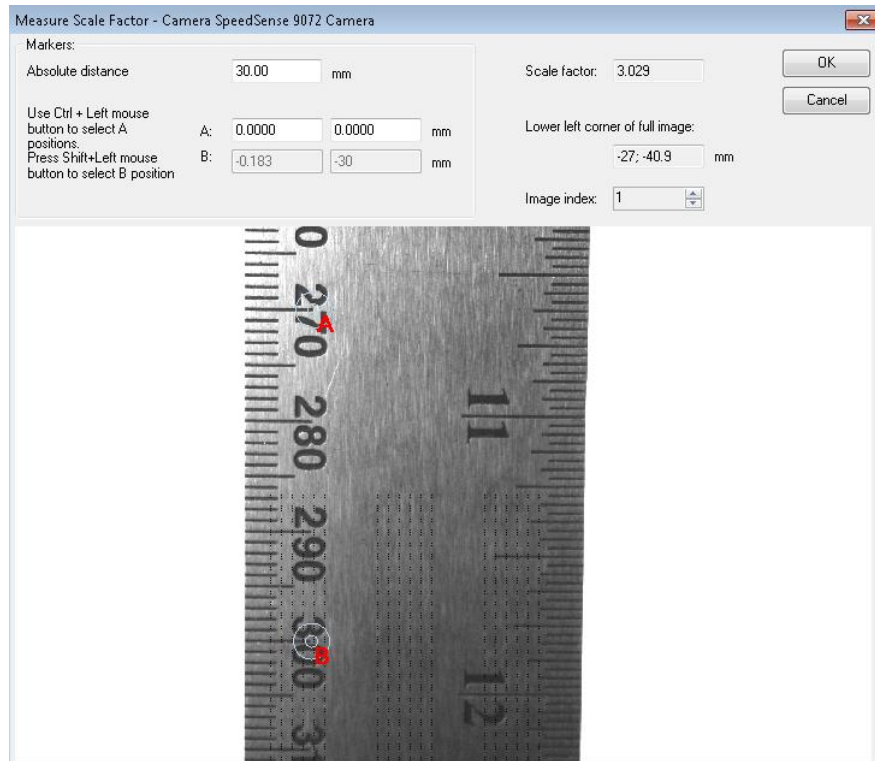


Figure 3.18: Calibration Image

### 3.5.3 Shadow Sizer Processing

According to shadow principle shadow sizer processing acquires data of particle size, shape, velocity, their position. Because of shadow principle there is no limitation of particle size and shape.

Images were taken from test section with single frame and 1000 Hz. Later single frame images were converted into double frame images. Double frame images were required to get particles velocity. From particles characterization window shadow assistant helps to capture the particle from the image. Particle was selected by shadow assistant with their contour and statistical information like particle pixel depth and edge gradients. Fig. 3.18 shows a selection method of particle with the help of shadow assistant. After shadow sizer processing it can detect

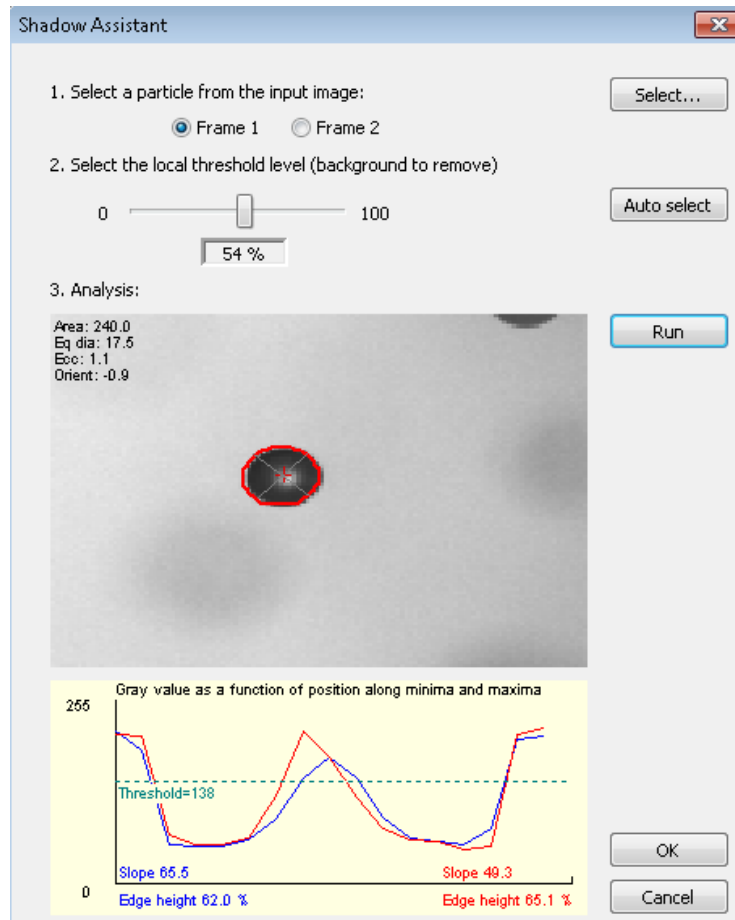


Figure 3.19: Particle Selection with its Contour

the particles, their contour, their velocity with direction and also their mean diameter. Fig. 3.19 shows a sample of double frame image and Fig. 3.20 shows its shadow processed results.

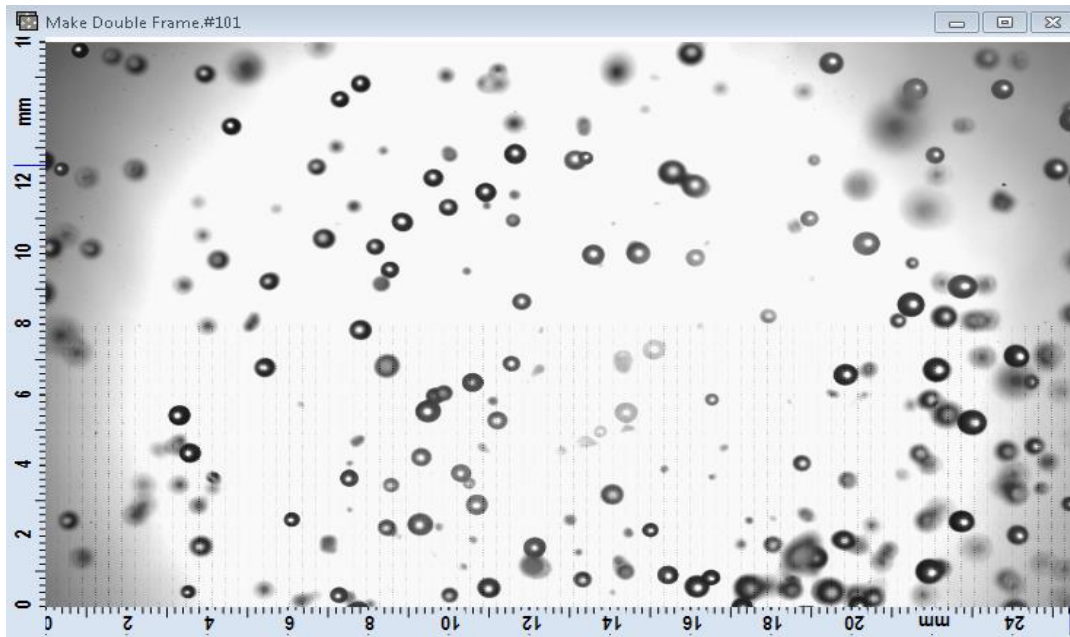


Figure 3.20: Shadow Image of Test Particles

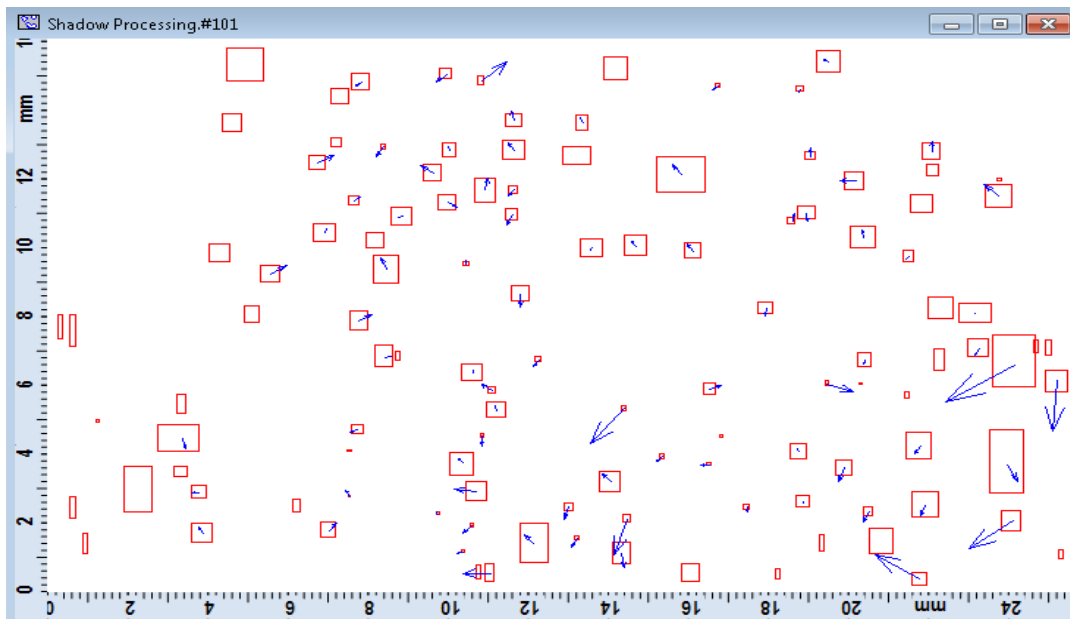


Figure 3.21: Example of Shadow Sizer Processed Result

### 3.6 Test Matrix

The section will describe test matrix for the results presented in chapter-5.

- 1) Observe the Effect of Particle Density on Hydrodynamic Behavior of a Gas-Solid Fluidized Bed for non-spherical particles
- 2) Measuring sphericity of the particles six ranges from 500  $\mu\text{m}$  -1400  $\mu\text{m}$ .
- 3) Measuring terminal velocity of the non-spherical particle with different ranges and different sphericities.

A test matrix has shown below of our experiment to observe hydrodynamics of laboratory fluidized bed, sphericity and terminal velocity measurement of the particles.

Table 3.2: Test Matrix to Observe the Effect of Particle Density on Hydrodynamic Behavior of a Gas-Solid Fluidized Bed for non-spherical particles

Particle	Particle Size ( $\mu\text{m}$ )	Bed Height (cm)
Hematite	90-425	3, 4, 5
	125-300	3, 4, 5
Borosilicate Glass beads	90-425	3, 4, 5
	125-300	3, 4, 5

Table 3.3: Sphericity measurement of the particles for different ranges

Range		Sphericity							
500-600	0.45-0.50	0.51-0.55	0.56-0.60	0.61-0.65	0.66-0.70	0.71-0.75	0.76-0.80	0.81-0.85	0.86-0.90
600-710									
710-850									
850-1000									
1000-1180									
1180-1400									

### 3.7 Statistical Analysis of Experimental Data

For experimental results it is required to identify the specifications for measuring systems. While taking measurement it is observed some randomness into measured data even if the same measurement has taken repeatedly. This randomness mainly caused by uncontrolled variables, less precision of measuring instrument. This randomness can make an effect on drawing a conclusion from measured data (34). Thus, before using experimental data it is obvious to make a statistical analysis of those. Table 3.4 shows 29 data set of pressure drop (unit=Pa) taken with constant flow velocity .073 m/sec.

Table 3.4: Experimental data set of pressure drop at 0.73 m/sec flow velocity

506.07342	499.8682	503.3155	515.726	515.726	511.5892
512.27868	494.3524	509.5208	494.4903	510.8997	516.4155
496.42079	516.4155	506.7629	512.9682	517.7945	528.1366
502.62605	499.1787	508.1418	499.1718	512.2787	507.4524
507.45237	515.726	499.8682	526.0681	529.5155	

These measurements were taken for non-spherical particles ranges from 355-500  $\mu\text{m}$ . 1 minute interval were taken before taking each data. Basic statistics of measured data has shown in Table 3.5.

Table 3.5: Statistical Description of Measured Data

Number of Measured Data	Minimum Value	Maximum Value	Mean Value	Median	Standard Deviation
29	494.35	529.52	509.53	509.52	9.4

From statistical analysis it is found that standard deviation is 9.4 Pa. Standard deviations are considered as statistically significant normal random error. Because of some error in measurement a constant value is always needed to add up to the measured value. That added value was 6.89 Pa. This value is referred as bias error. Table 3.6 shows a statistical analysis of measured data.

Table 3.6: Statistical Analysis of Pressure Drop with .073 m/sec Flow Velocity

Mean Pressure	Random Error	Bias Error
509.53 Pa	9.40 Pa	6.89 Pa
Error in Percentage	1.84%	1.35%

On the other hand Fig. 3.21 shows a statistical histogram of pressure drop with bin width range 5 Pa.

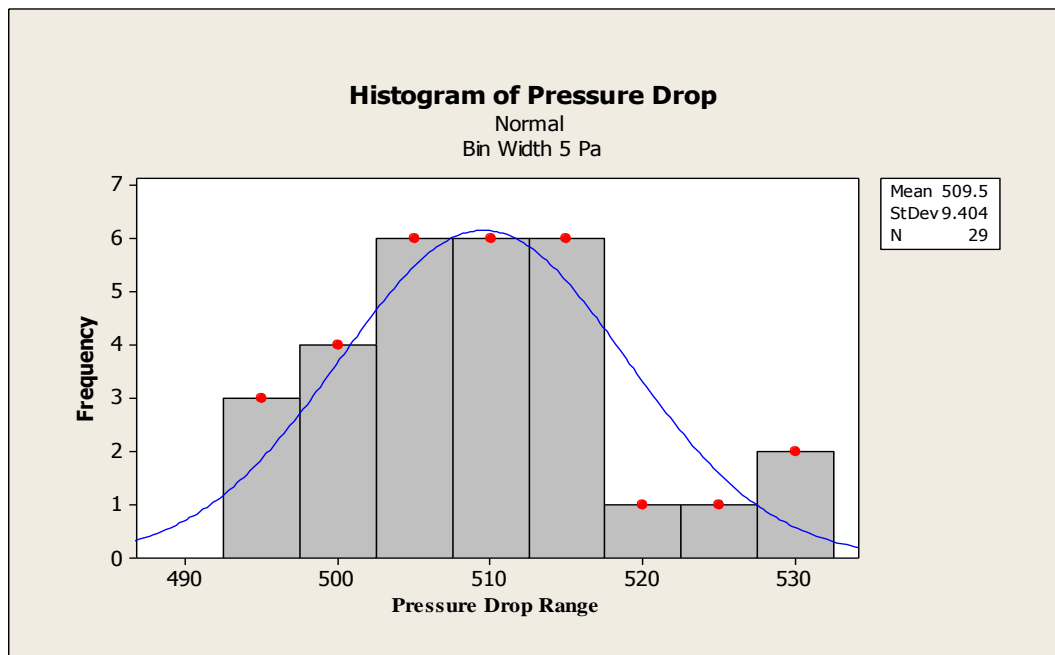


Figure 3.21: Histogram of Pressure Drop

An error was also calculated for measurements using a 95% Confidence interval by using t-distribution table. Our measured data have 28 degrees of freedom. For a 95% confidence interval and for degree of freedom 28 our required value from t-distribution table is 2.048. Finally, from standard procedure our lower and upper ranges were found. The ranges are 505.47 to 513.09.

Table 3.3: t-distribution table

df	$\alpha = 0.1$	0.05	0.025	0.01	0.005	0.001	0.0005
$\infty$	$t_{\alpha} = 1.282$	1.645	1.960	2.326	2.576	3.091	3.291
1	3.078	6.314	12.706	31.821	63.656	318.289	636.578
2	1.886	2.920	4.303	6.965	9.925	22.328	31.600
3	1.638	2.353	3.182	4.541	5.841	10.214	12.924
4	1.533	2.132	2.776	3.747	4.604	7.173	8.610
5	1.476	2.015	2.571	3.365	4.032	5.894	6.869
6	1.440	1.943	2.447	3.143	3.707	5.208	5.959
7	1.415	1.895	2.365	2.998	3.499	4.785	5.408
8	1.397	1.860	2.306	2.896	3.355	4.501	5.041
9	1.383	1.833	2.262	2.821	3.250	4.297	4.781
10	1.372	1.812	2.228	2.764	3.169	4.144	4.587
11	1.363	1.796	2.201	2.718	3.106	4.025	4.437
12	1.356	1.782	2.179	2.681	3.055	3.930	4.318
13	1.350	1.771	2.160	2.650	3.012	3.852	4.221
14	1.345	1.761	2.145	2.624	2.977	3.787	4.140
15	1.341	1.753	2.131	2.602	2.947	3.733	4.073
16	1.337	1.746	2.120	2.583	2.921	3.686	4.015
17	1.333	1.740	2.110	2.567	2.898	3.646	3.965
18	1.330	1.734	2.101	2.552	2.878	3.610	3.922
19	1.328	1.729	2.093	2.539	2.861	3.579	3.883
20	1.325	1.725	2.086	2.528	2.845	3.552	3.850
21	1.323	1.721	2.080	2.518	2.831	3.527	3.819
22	1.321	1.717	2.074	2.508	2.819	3.505	3.792
23	1.319	1.714	2.069	2.500	2.807	3.485	3.768
24	1.318	1.711	2.064	2.492	2.797	3.467	3.745
25	1.316	1.708	2.060	2.485	2.787	3.450	3.725
26	1.315	1.706	2.056	2.479	2.779	3.435	3.707
27	1.314	1.703	2.052	2.473	2.771	3.421	3.689
28	1.313	1.701	2.048	2.467	2.763	3.408	3.674
29	1.311	1.699	2.045	2.462	2.756	3.396	3.660
30	1.310	1.697	2.042	2.457	2.750	3.385	3.646
60	1.296	1.671	2.000	2.390	2.660	3.232	3.460

## **Chapter 4 : Computational Domain**

This chapter of the thesis will explain the computational domain created to simulate the experimental work. ANSYS Workbench 13.0 Platform is used to create and simulate the computational domain. For the computational analysis a static bed height of 5.5 cm was selected to compare to experimental results. The fluid simulation domain consists of a three-dimensional system with the origin of the grid centered at the center of the column. A grid independence test was conducted and was determined that the grid of 35420 cells was optimal for the analysis. The working fluid was selected as isothermal air at 25°C. The gas velocity was varied for each simulation run from 0 – 1.4 m/s in the axial direction in increments of 0.1 m/s, corresponding to experiments. The boundary conditions for the gas phase consist of no-slip, impermeable walls on the vertical sides of the bed. For the outflow boundary condition at the top of the bed, a pressure outlet set at atmospheric pressure is specified across the entire width. At the bed inlet, a velocity inlet boundary condition was specified. The developed model was then solved numerically using a finite volume technique in Fluent. The phase coupled SIMPLE algorithm was used to couple pressure and velocity and a first order upwind scheme used to solve for all terms.

### **4.1 Geometry**

The geometry was created maintaining the dimensions of the experimental setup. Height of the fluidized bed was reduced to 0.5 meters instead of 0.8 meters. Because particles do not reach at the top of the fluidized bed with the velocity provided and so to reduce the computational load the height of the fluidized bed was reduced to 0.5. The geometry of the bed is created using ANSYS 13.0 Workbench Geometry toolbox. Fig. 4.1a shows the schematic

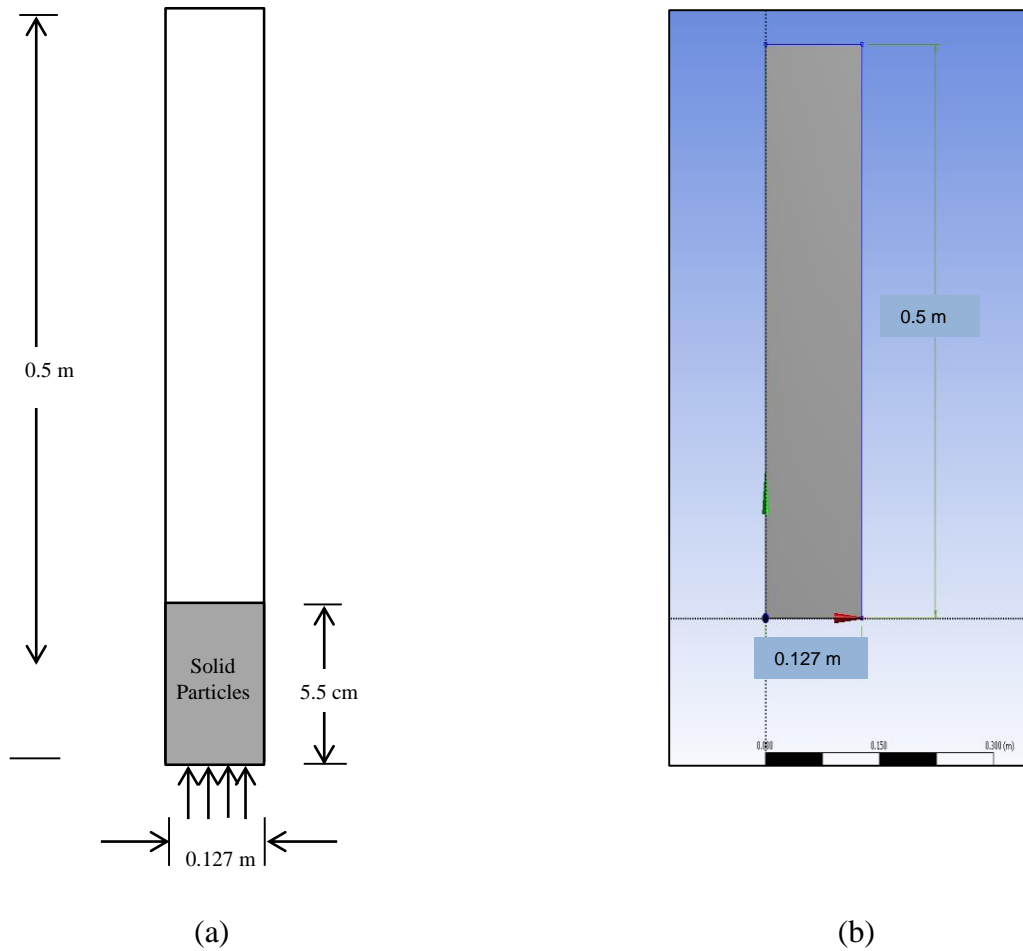


Figure 4.1: (a) Schematic diagram of the fluidized bed, (b) Geometry made in ANSYS

#### Workbench 13.0

Diagram of the fluidized bed and Fig. 4.1b shows the geometry created using ANSYS Workbench 13.0.

### 4.2 Boundary conditions

The inlet of the channel was considered velocity inlet, for different Reynolds number different velocity is selected. Initial velocity was 0 m/s, simulation was run up to 1.4 m/s velocity with the increment of 0.1 m/s. The outlet of the channel is considered pressure outlet. Specification of static gauge pressure is required to select this boundary condition; in this case the static gauge pressure is zero. The other four boundaries are considered wall with no slip

condition. Fig. 4.1b shows the boundary conditions, which was done in ANSYS workbench 13.0. Fig. 4.2 shows the boundary conditions of the fluidized bed in ANSYS Fluent 13.0.

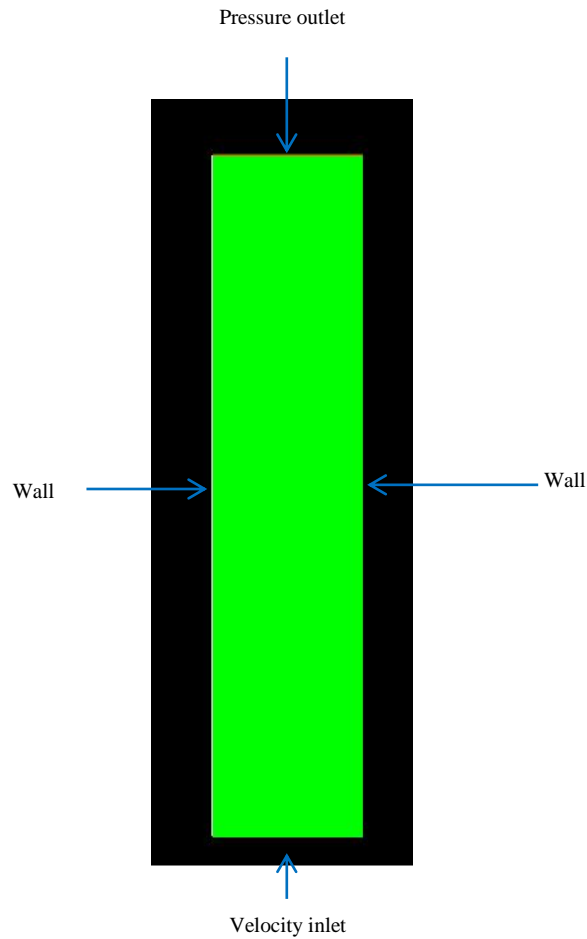


Figure 4.2: Boundary Conditions

### 4.3 Mesh

The mesh was generated using ANSYS Workbench 13.0 meshing tool. Quad meshing is implemented in the geometry. Using bias feature of the meshing tool available, more grid are created at the bottom part of the bed. A grid independence test was conducted and was determined that the grid of 35420 cells was optimal for the analysis.

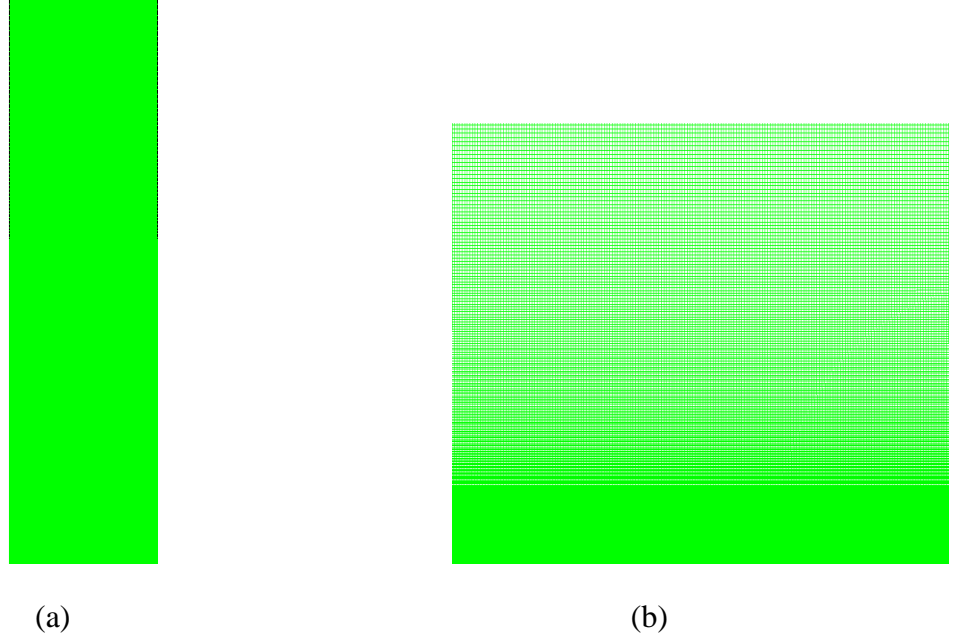


Figure 4.3: (a) Mesh of the 2D bed, (b) Bottom section of the bed

#### 4.4 Eulerian-Eulerian Models

In the Euler-Euler approach, the different phases are treated mathematically as interpenetrating continua. Since the volume of a phase cannot be occupied by the other phases, the concept of phasic volume fraction is introduced. These volume fractions are assumed to be continuous functions of space and time and their sum is equal to one. Conservation equations for each phase are derived to obtain a set of equations, which have similar structure for all phases. These equations are closed by providing constitutive relations that are obtained from empirical information, or, in the case of granular flows, by application of kinetic theory.

An Eulerian-Eulerian approach for both the fluid and the solid phase was considered for the simulation. Eqs. 4.1-4.4 represent the governing equations used to calculate the pressure and velocity components within a gas-solid bed. In these equations the subscript g denotes fluid (gas) and s the solid particle,  $\varepsilon$  is the volume fraction,  $\tau$  is the stress tensor, and  $K_{\text{drag}}$  accounts for the

momentum exchange between the fluid phase and the solid phase. Eqs. 4.1 and 4.2 show the mass conservation equations for solid and gas flow while Eqs. 4.3 and 4.4 show the momentum conservation equations for the same flow field [55].

$$\frac{\partial}{\partial t}(\varepsilon_g \rho_g) + \nabla \cdot (\varepsilon_g \rho_g \vec{V}_g) = 0 \quad (4.1)$$

$$\frac{\partial}{\partial t}(\varepsilon_s \rho_s) + \nabla \cdot (\varepsilon_s \rho_s \vec{V}_s) = 0 \quad (4.2)$$

$$\frac{\partial}{\partial t}(\varepsilon_g \rho_g \vec{V}_g) + \nabla \cdot (\varepsilon_g \rho_g \vec{V}_g \vec{V}_g) = \nabla \cdot \bar{\bar{\tau}}_g - \varepsilon_g \nabla p + \varepsilon_g \rho_g \vec{g} - K_{drag}(\vec{V}_g - \vec{V}_s) \quad (4.3)$$

$$\frac{\partial}{\partial t}(\varepsilon_s \rho_s \vec{V}_s) + \nabla \cdot (\varepsilon_s \rho_s \vec{V}_s \vec{V}_s) = \nabla \cdot \bar{\bar{\tau}}_s - \varepsilon_s \nabla p - \nabla P_s + \varepsilon_s \rho_s \vec{g} + K_{drag}(\vec{V}_g - \vec{V}_s) \quad (4.4)$$

Here the gas phase stress tensor is calculated according to Newton's expression shown in Eq. 4.5.

$$\bar{\bar{\tau}}_g = \mu_g [\nabla \vec{V}_g + \nabla^T \vec{V}_g] - \frac{2}{3} \mu_g (\nabla \cdot \vec{V}_g) \bar{\bar{I}} \quad (4.5)$$

For the solid phase, the gradient of the particle pressure is represented by  $P_s$  and the particle phase stress tensor is given by Eqs. 4.6 and 4.7 respectively:

$$P_s = \rho_s \varepsilon_s \Theta_s + 2 \rho_s \varepsilon_s^2 g_o \Theta_s (1 + e_s) \quad (4.6)$$

$$\bar{\bar{\tau}}_s = \mu_s [\nabla \vec{V}_s + \nabla^T \vec{V}_s] + \left( \lambda_s - \frac{2}{3} \mu_s \right) (\nabla \cdot \vec{V}_s) \bar{\bar{I}} \quad (4.7)$$

Where,  $e_s$  is the coefficient of restitution which was assumed as 0.9.  $g_o$  is the radial distribution function in Eq. 4.8 and  $\Theta_s$  is the granular temperature which is proportional to the kinetic energy of the fluctuating particle motion. The transport equation derived from kinetic

theory is used to calculate the field of granular temperature, Eq. 4.9. For the present model the granular temperature was initially set to a value of  $1.0 \times 10^{-5} \text{ m}^2\text{s}^{-2}$ .

$$g_o = \left[ 1 - \left( \frac{\varepsilon_s}{\varepsilon_{s,max}} \right)^{1/3} \right]^{-1} \quad (4.8)$$

$$\frac{3}{2} \left[ \frac{\partial}{\partial t} (\varepsilon_s \rho_s \theta_s) + \nabla \cdot (\varepsilon_s \rho_s \vec{V}_s \theta_s) \right] = (-P_s \bar{I} + \bar{\tau}_s) : \nabla \vec{V}_s + \nabla \cdot (\kappa_s \nabla \theta_s) - \gamma_s + \Psi_{ls} \quad (4.9)$$

The maximum packing fraction ( $\varepsilon_{s,max}$ ) was assumed to vary based on the sphericity of the particles used. Yang [13] provides data on expected maximum packing densities based on the sphericity of the particles used, based on these values the present model used values between 0.32 to 0.59 for different shapes. In Eq. 4.9,  $\kappa_s$  is the diffusion coefficient,  $\gamma_s$  is the collisional dissipation energy, and  $\Psi_{ls}$  represents the energy exchange between gas and solid phase. These are defined in Eqs. 4.10-4.12:

$$\kappa_s = \frac{150 \rho_s d_p \sqrt{\theta_s \pi}}{384 g_o (1 + e_s)} \left[ 1 + \frac{6}{5} g_o \varepsilon_s (1 + \varepsilon_s) \right]^2 + 2 \varepsilon_s^2 \rho_s d_p g_o (1 + e_s) \left( \frac{\theta}{\pi} \right)^{1/2} \quad (4.10)$$

$$\gamma_s = 3(1 - e_s^2) \rho_s \varepsilon_s^2 g_o \theta_s \left[ \frac{4}{d_p} \sqrt{\frac{\theta_s}{\pi}} - \nabla \cdot \vec{V}_s \right] \quad (4.11)$$

$$\Psi_{ls} = -3K_{drag} \theta_s \quad (4.12)$$

The solids stress tensor, Eq. 4.7, contains shear and bulk viscosities from particle momentum exchange due to translation and collision, Eq. 4.13.

$$\mu_s = \mu_{s,col} + \mu_{s,kin} \quad (4.13)$$

$$\text{Where,} \quad (4.14)$$

$$\mu_{s,col} = \frac{4}{5} \varepsilon_s \rho_s d_p g_o (1 + e_s) \left( \frac{\theta_s}{\pi} \right)^{1/2}$$

$$\text{and} \quad (4.15)$$

$$\mu_{s,kin} = \frac{10 \rho_s d_p \sqrt{\theta \pi}}{96 g_o (1 + e_s)} \left[ 1 + \frac{4}{5} (1 + e_s) \varepsilon_s g_o \right]^2$$

The solids bulk viscosity that appears in Eq. 4.7 accounts for the resistance of the granular particles to compression and expansion, the relation is shown in Eq. 4.16:

$$\lambda_s = \frac{4}{3} \varepsilon_s^2 \rho_s d_p g_o (1 + e_s) \left( \frac{\theta_s}{\pi} \right)^{1/2} \quad (4.16)$$

This paper primarily focuses on the development of the momentum exchange ( $K_{drag}$ ) shown in Eqs. 4.3 and 4.4. Since the parameter  $K_{drag}$  depends on the drag coefficient for more dilute flows, it can be modeled a variety of ways. Some typical approximations used for the estimation of  $K_{drag}$  are shown in Eqs. 4.17 and 4.18 [56], [57], [58].

$$K_{drag} = 150 \frac{(1-\varepsilon_g)^2}{\varepsilon_g^2} \frac{\mu_g}{d_p^2} + 1.75(1 - \varepsilon_g) \frac{\rho_g}{\varepsilon_g d_p} (\vec{V}_g - \vec{V}_s) \quad \text{for } \varepsilon_g \leq 0.8 \quad (4.17)$$

$$K_{drag} = \frac{3}{4} C_D \frac{(1-\varepsilon_g)\varepsilon_g}{d_p} \rho_g (\vec{V}_g - \vec{V}_s) \varepsilon_g^{-2.65} \quad \text{for } \varepsilon_g > 0.8 \quad (4.18)$$

For the current study Eq. 4.18 is modified to accommodate the newly developed  $C_D$  correlation and compared to experimental results. The modification was implemented through a user-defined function sub-routine in ANSYS Fluent 13.0 code.

In general, the Eulerian-Eulerian approach is computationally more efficient and therefore can be applied to systems with a larger number of particles than the Eulerian-Lagrangian approach, which is limited to approximately 100,000 particles. However, incorporation of complex particle physics is a more difficult task with Eulerian-Eulerian models. The impact of cohesion on such a continuum quantity is more difficult to model than its incorporation on a particle-particle level. The focus of many subsequent Eulerian-Eulerian efforts has been to incorporate improved constitutive relations for the solid phase.

#### 4.5 Conservation Equations

Solving mass, momentum and energy equations the simulation of fluidized bed is done in ANSYS Fluent 13.0. Following are the equations solved by ANSYS fluent to produce the results from the given input.

Momentum conservation equations of gas and solid phases:

$$\frac{\partial}{\partial t} \cdot (\alpha_g \cdot \rho_g) + \nabla \cdot (\alpha_g \cdot \rho_g \cdot \vec{v}_g) = 0 \quad (4.19)$$

$$\frac{\partial}{\partial t} \cdot (\alpha_s \cdot \rho_s) + \nabla \cdot (\alpha_s \cdot \rho_s \cdot \vec{v}_s) = 0 \quad (4.20)$$

Momentum conservation equations of gas and solid phases:

$$\begin{aligned} & \frac{\partial}{\partial t} \cdot (\alpha_g \cdot \rho_g \cdot \vec{v}_g) + \nabla \cdot (\alpha_g \cdot \rho_g \cdot \vec{v}_g^2) \\ & = -\alpha_g \cdot \nabla p + \nabla \cdot \bar{\tau}_g + \alpha_g \cdot \rho_g \cdot \vec{g} + K_{gs} \cdot (\vec{v}_g - \vec{v}_s) \end{aligned} \quad (4.21)$$

#### 4.6 K-epsilon model:

K-epsilon turbulence model is the most common model used in Computational Fluid Dynamics to simulate turbulent conditions. It is a two equation model which gives a general description of turbulence by means of two transport equations. The way forward is to consider statements regarding the dynamics of turbulence. The k- $\epsilon$  model focuses on the mechanisms that affect the turbulent kinetic energy. The instantaneous kinetic energy  $k(t)$  of a turbulent flow is the sum of the mean kinetic energy( $K$ ) and turbulent kinetic energy( $k$ ).

$$\text{Mean kinetic energy, } K = \frac{1}{2} (U^2 + V^2 + W^2) \quad (4.22)$$

$$\text{Turbulent kinetic energy, } k = \frac{1}{2} (\overline{u^2} + \overline{v^2} + \overline{w^2}) \quad (4.23)$$

$$k(t) = K + k \quad (4.24)$$

Standard k-epsilon model is used among the three types of k-epsilon turbulence models exist.

Those are:

- 1) Standard k-epsilon model
- 2) RNG k-epsilon model and
- 3) Realizable k-epsilon model

##### 4.6.1 Standard k-epsilon model

Standard k-epsilon model is a turbulence model based on model transport equations for the turbulence kinetic energy ( $k$ ) and its dissipation rate ( $\epsilon$ ). From the exact equation the model transport equation for  $k$  is derived, the model transport equation for  $\epsilon$  was obtained using physical reasoning and bears little resemblance to its mathematically exact counterpart. In the derivation of the k-epsilon model, the assumption is that the flow is fully turbulent, and the effects of the molecular viscosity is negligible [59].

#### 4.6.1.1 Transport Equations for the Standard k-epsilon model

The turbulence kinetic energy,  $k$ , and its rate of dissipation,  $\varepsilon$ , are obtained from the following transport equations:

$$\frac{\partial}{\partial t}(\rho k) + \frac{\partial}{\partial x_i}(\rho k u_i) = \frac{\partial}{\partial x_j} \left[ \left( \mu + \frac{\mu_t}{\sigma_k} \right) \frac{\partial k}{\partial x_j} \right] + G_k + G_b - \rho \varepsilon - Y_M + S_k \quad (4.25)$$

and

$$\begin{aligned} \frac{\partial}{\partial t}(\rho \varepsilon) + \frac{\partial}{\partial x_i}(\rho \varepsilon u_i) \\ = \frac{\partial}{\partial x_j} \left[ \left( \mu + \frac{\mu_t}{\sigma_\varepsilon} \right) \frac{\partial \varepsilon}{\partial x_j} \right] + C_{1\varepsilon} \frac{\varepsilon}{k} (G_k + C_{3\varepsilon} G_b) - C_{2\varepsilon} \rho \frac{\varepsilon^2}{k} + S_\varepsilon \end{aligned} \quad (4.26)$$

In these equations,  $G_k$  represents the generation of turbulence kinetic energy due to the mean velocity gradients,  $G_b$  is the generation of turbulence kinetic energy due to buoyancy,  $Y_M$  represents the contribution of the fluctuating dilatation in compressible turbulence to overall dissipation rate.  $C_{1\varepsilon}$ ,  $C_{2\varepsilon}$ , and  $C_{3\varepsilon}$  are constants.  $\sigma_k$  and  $\sigma_\varepsilon$  are the turbulent Prandtl numbers for  $k$  and  $\varepsilon$ , respectively.  $S_k$  and  $S_\varepsilon$  are user defined source term.

#### 4.6.1.2 Modeling the Turbulent Viscosity

The turbulent viscosity,  $\mu_t$ , is computed by combining  $k$  and  $\varepsilon$  as follows:

$$\mu_t = \rho C_\mu \frac{k^2}{\varepsilon} \quad (4.27)$$

Where,  $C_\mu$  is a constant.

#### 4.6.1.3 Model Constants

The model constants  $C_{1\varepsilon}$ ,  $C_{2\varepsilon}$ ,  $C_\mu$ ,  $\sigma_k$  and  $\sigma_\varepsilon$  have the following default values

$$C_{1\varepsilon} = 1.44, C_{2\varepsilon} = 1.92, C_\mu = 0.09, \sigma_k = 1.0 \text{ and } \sigma_\varepsilon = 1.3$$

These default are determined from experiments for fundamental turbulent flows including frequently encountered shear flows like boundary layers, mixing layers and jets as well as for decaying isotropic grid turbulence. These have been found to work fairly well for a wide range of wall-bounded and free shear flows [59].

## 4.7 Problem Setup

The problem setup is a section in the ANSYS Fluent 13.0 platform used to set up the problem. It includes few sections, General, Models, Materials, Phases, Cell Zone Conditions, Boundary Conditions, and Reference Values. In the following subsections the elements of the problem set up are going to be discussed.

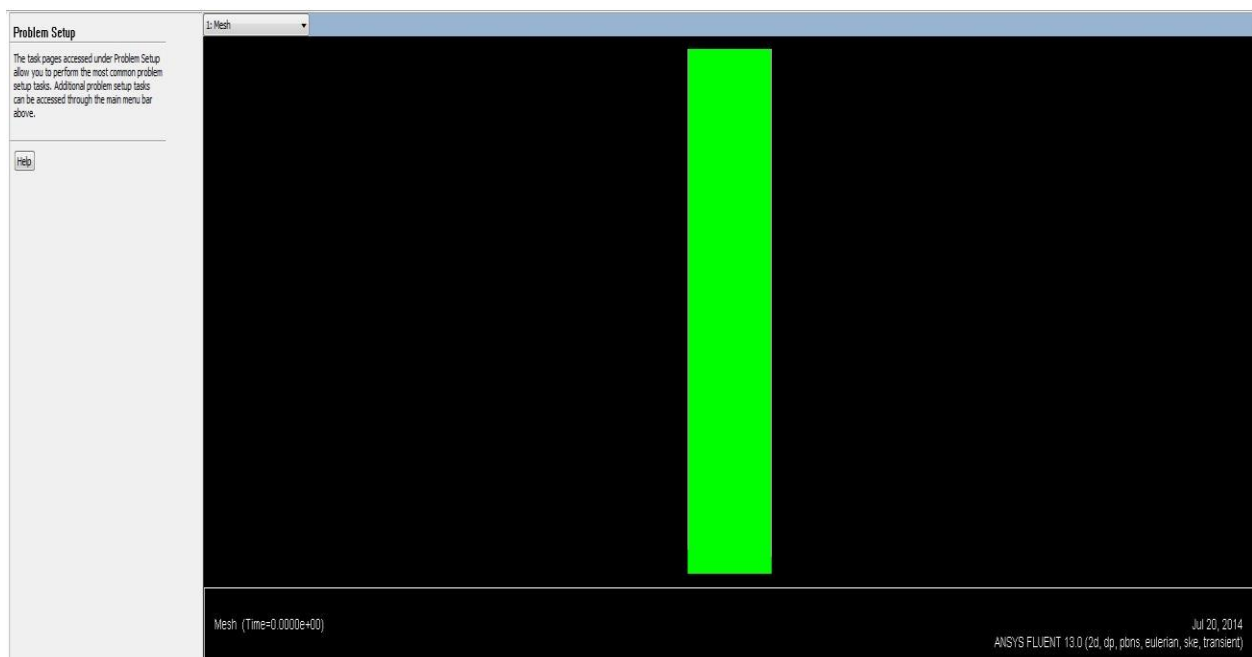


Figure 4.4: Problem Setup

### 4.7.1 General

In the General section the Mesh quality can be checked, Solver, Time and Gravitational Acceleration are selected and modified. Mesh scale can be checked in the General section.

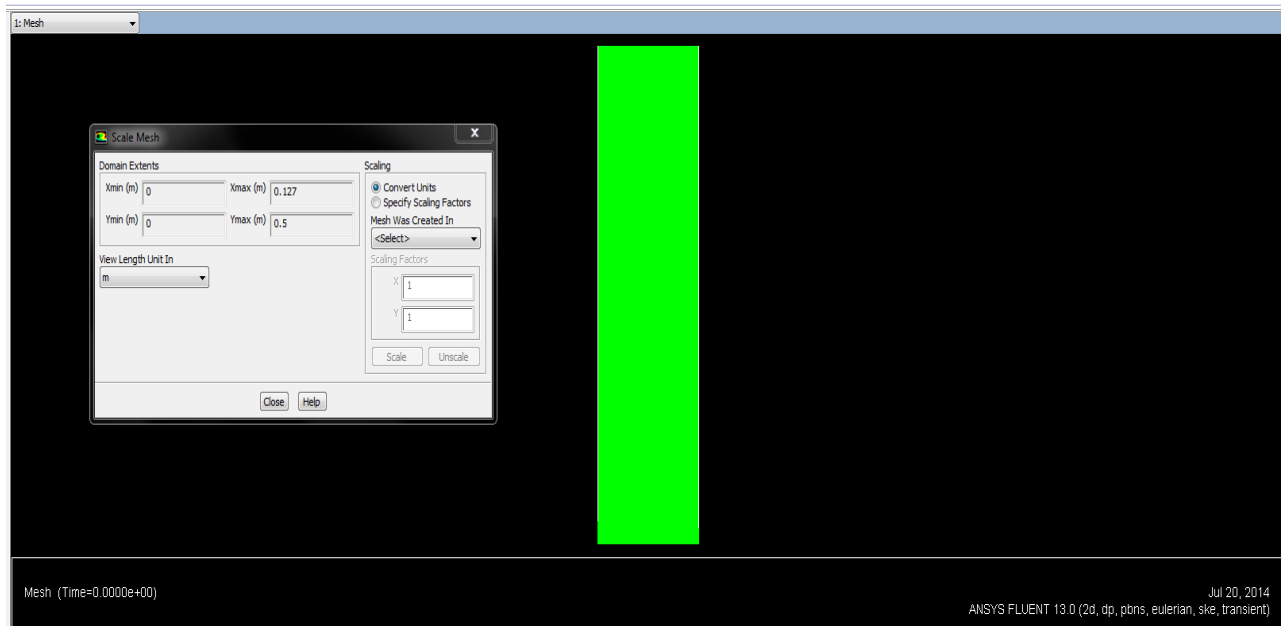


Figure 4.5: Mesh Scale in the General Section

Fig. 4.3 shows the domain 0 to 0.127 meters in the X axis and 0 to 0.5 meters in the Y axis. The actual setup in 0.8 meters in height. It is moved down to 0.5 meters because most of the solid and fluid interaction occurs at the bottom of the bed occurs and at top of the bed nothing occurs. We found that reduction of the reactor height in the domain would save computational resources and time without sacrificing accuracy. Simulations are run using this configuration of the reactor.

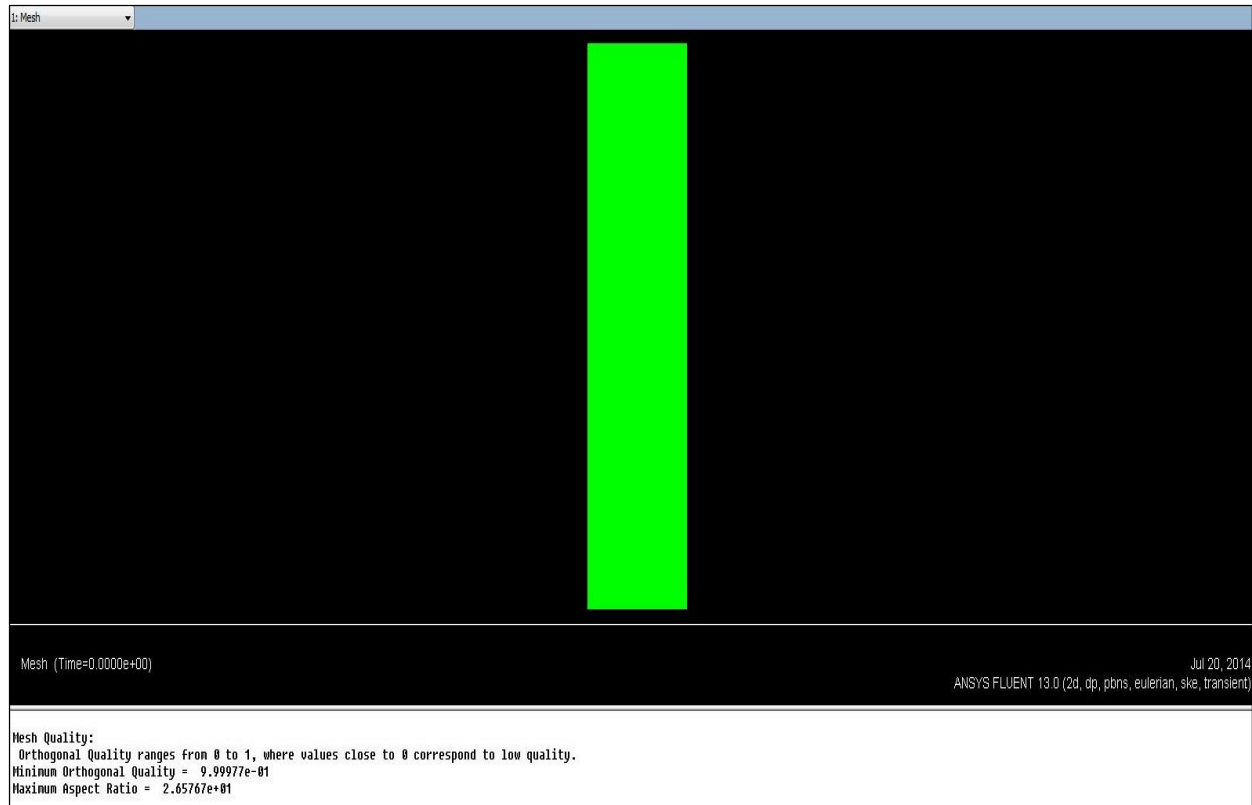


Figure 4.6: Mesh Quality.

Mesh quality is one of the most important factors to produce good results. The orthogonal quality is the measurement of the mesh quality, it ranges from 0 to 1, where values close to 0 corresponds to low quality. In our case the minimum orthogonal quality of the mesh is 9.99977e-01 and maximum aspect ratio is 2.65767e+01.

The time scheme is considered transient, since the simulation was run for several seconds. Gravitational Acceleration was considered  $-9.81 \text{ m/s}^2$ , since gravity acts vertically downwards.

#### 4.7.2 Models

Multiphase Eulerian model is used for this simulation. Standard k-epsilon model is used among the k-epsilon models. For Near-Wall Treatment, Standard Wall Functions is used. Since

two phases are involved Dispersed Turbulence Multiphase Model is used in the Turbulence Multiphase section. Fig. 4.7 shows the model set up in ANSYS Fluent 13.0.

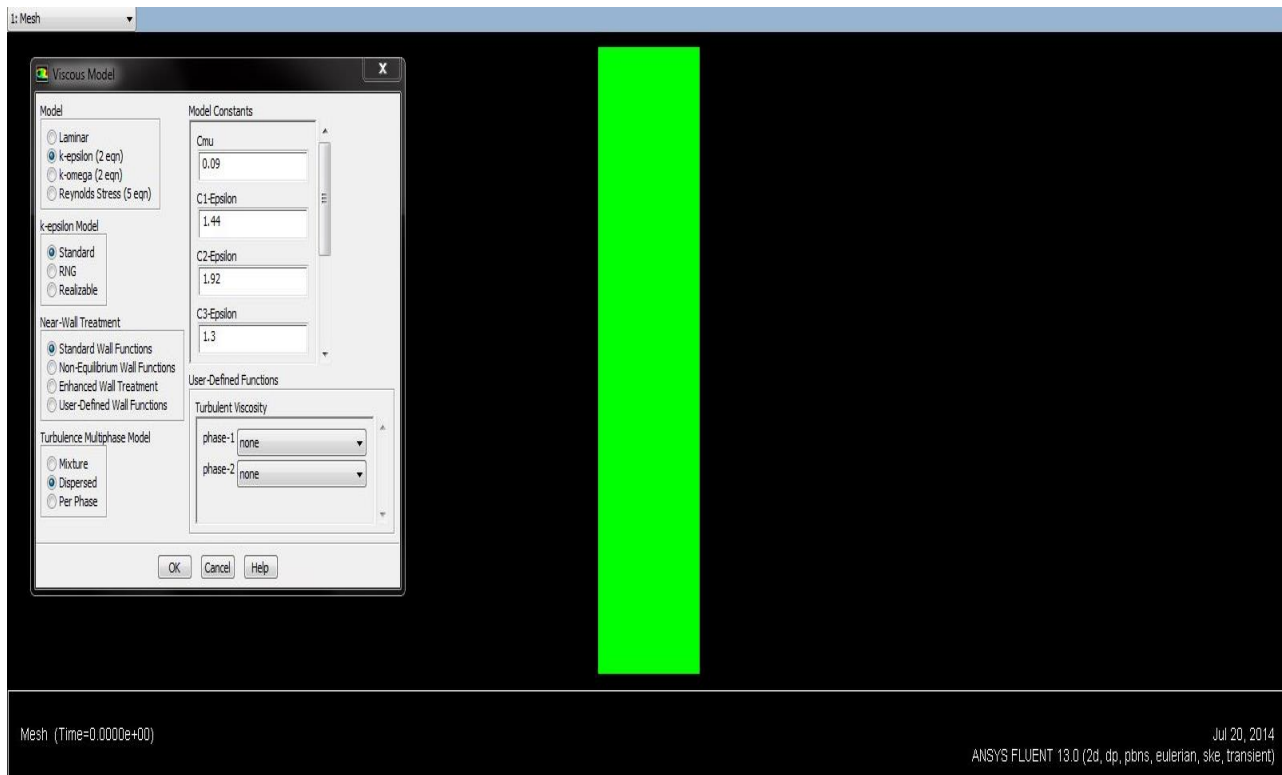


Figure 4.7: Models

Table 4.1: Conditions for the Simulation Using 2D Assumption

Geometry		Gas	
Width	0.127 meters	Type	Air
Height	0.5 meters	Density	1.225 kg/m <sup>3</sup>
		Viscosity	1.7894e-05
Boundary Condition		Closing Equations	
Inlet	Velocity	Drag correlation	Syamlal and O'brien,
Outlet	Pressure		Gidaspow,
Walls	No slip		Developed Drag model
Initial Condition		Granular Viscosity	syamlal-obrien
Velocity of air	0 m/s	Granular Bulk Viscosity	lun-et-al
Volume fraction	0.69	Frictional Viscosity	schaeffer
Particle		Solid Pressure	lun-et-al
Type	Glass bead	Iteration	
Size	0.001 meters		
Density	2230 kg/m <sup>3</sup>	Time Step Size	0.001 sec
Viscosity	1.7894e-05	Number of Time Steps	2000
Coefficient of restitution	0.81	Max Iteration/Time Step	20
Angle of Internal	30 <sup>0</sup>		

#### 4.8 Drag analysis of the particles

The drag analysis is done by measuring the displacement of particles with time. There are equipment and procedure to get this displacement with time. Microscopic Video Camera is used to capture the particle image to get the particle diameter. Dino Capture 2.0 was synchronized with microscopic video camera to analyze the particle diameters that are in micron scales. A hopper is used to introduce the drag test particles into the bed a 5600A overhead; hopper made

from stainless steel and having the maximum discharge height of 15 1/4 inches and capacity of 1/4 cubic feet. A Dantec Dynamics 5 kHz high speed camera Phantom was used to capture the particle movement for the drag analysis. The initial terminal velocity was calculated from the following equation.

$$V_t = \sqrt{\frac{4 \cdot g \cdot d \cdot (\rho_s - \rho_f)}{3 \cdot \rho_f \cdot C_D}} \quad (4.28)$$

Where  $V_t$  is the terminal velocity,  $d$  is the mean diameter of the solid particles,  $\rho_s$  is the density of the solid particles,  $\rho_f$  is the density of fluid, and  $C_D$  is the drag coefficient.

The distance from top of the bed to the point where a particle is supposed to reach the terminal velocity was calculated using Eqn. (3.3) where  $H$  is the distance traveled by a single free falling particle.

$$H = \frac{V_t^2}{2g} \quad (4.29)$$

The particles were introduced into the bed through a hopper mounted above the bed. The 500 KHz camera was used to capture the particle motion in the free falling stream using 3100 fps frame rate. Using the phantom software the starting and ending point of the free falling particles in the camera frame and the time required to travel that distance by a single particle were determined. Final particle velocity is then determined by using the following equation:

$$V_t = \frac{\Delta s}{\Delta t} \quad (4.30)$$

Finally, drag coefficient is calculated from the following equation:

$$C_D = \frac{4 \cdot g \cdot d \cdot (\rho_s - \rho_f)}{3 \cdot \rho_f \cdot V_t^2} \quad (4.31)$$

## Chapter 5 : Results and Discussions

In this section, the experimental and computational results of the hydrodynamic behavior of the fluidized bed will be presented. Experiments are done for two different types of particles, Borosilicate glass beads and Hematite particles. Minimum fluidization velocity is one of the most important parameters to determine the behavior of the fluidized bed. Pressure drop vs superficial velocity is determined to evaluate the effect of density of the in a gas-solid fluidized bed. Computational analysis of the fluidized bed is a major part of the thesis. Using the existing drag correlations the simulation are done which does not consider the sphericity of the particles. In reality particles used in fluidized bed irregular in shape. So a new drag correlation has been developed which is implemented in ANSYS Fluent 13.0 to determine the fluidized bed behavior computationally considering sphericity.

The following experimental and computational results will be presented and compared in this section.

- 1) Effect of Particle Density on Hydrodynamic Behavior of a Gas-Solid Fluidized Bed for non-spherical particles.
- 2) Development of a drag model using a Non-Intrusive Optical Technique.
- 3) Comparison of computational to experimental data when using spherical particles and established drag models from Syamlal and O'Brien [60] and Gidaspow [56]. The model shows good agreement with experiments.
- 4) Qualitative comparison of bubbling behavior of particles from simulation and experiment.
- 5) Plots of drag coefficient at various Reynolds numbers for different drag models and newly proposed drag model.

- 6) Comparison of pressure drop versus superficial velocity using new drag model for different sphericities.

## **5.1 Effect of particle density on the hydrodynamic behavior of a Gas-Solid Fluidized Bed**

Density of particles play an important role on the hydrodynamic behavior of the fluidized bed. Two different types of particles, Borosilicate glass beads and Hematite are tested to observe the effect of density of the particles on a gas-solid fluidized bed. Canadian Hematite has density of  $4989 \text{ kg/m}^3$ , which is higher than Borosilicate glass beads which has density of  $2230 \text{ kg/m}^3$ . These two different types of particles shows different behavior in experiments. Two different types of mass distribution is used to study the fluidized bed. The following sections will describe the features of the mass distributions.

### **5.1.1 Mass distribution of the particles**

Due to wide range of particles and amount of different size range in two types of particles, Hematite and Borosilicate glass beads particles are arranged in two different arrangements. In one arrangement particles are arranged maintaining different weight percentage for each range but same weight percentage for both types of particle's particle ranges. And in another arrangement particles are arranged by same weight percentage in both types of particles.

#### **5.1.1.1 Mass distributions for 90-425 $\mu\text{m}$ particles**

For one set of particles, particles are characterized maintaining different weight percentage for each range but same weight percentage for both types of particle's particle ranges. This weight percentages scheme is used for 90-425  $\mu\text{m}$  particles range. The same weight percentages are maintained for both hematite and Borosilicate glass beads particles. Fig. 5.1

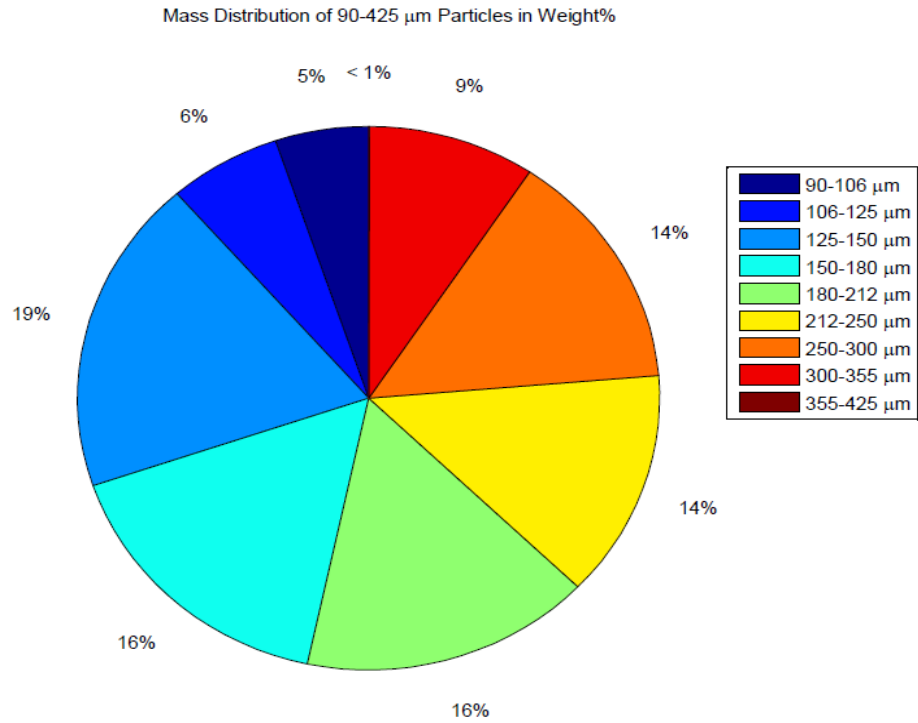


Figure 5.1: Mass Distribution of 90-425 micro meter particles in weight%

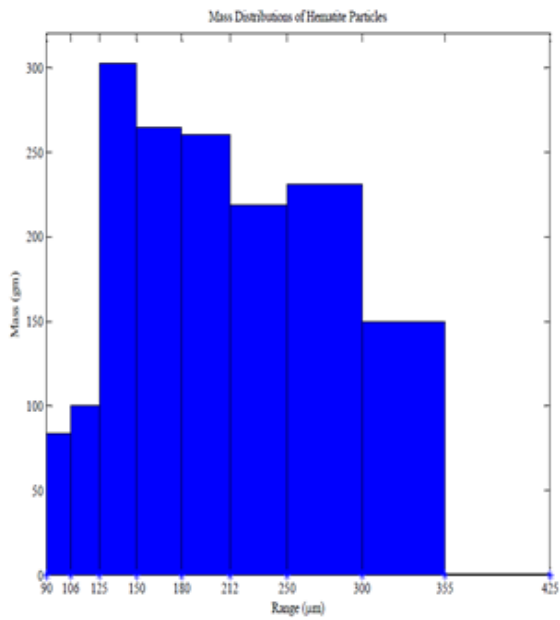


Figure 5.2: Mass distribution for Hematite Particles.

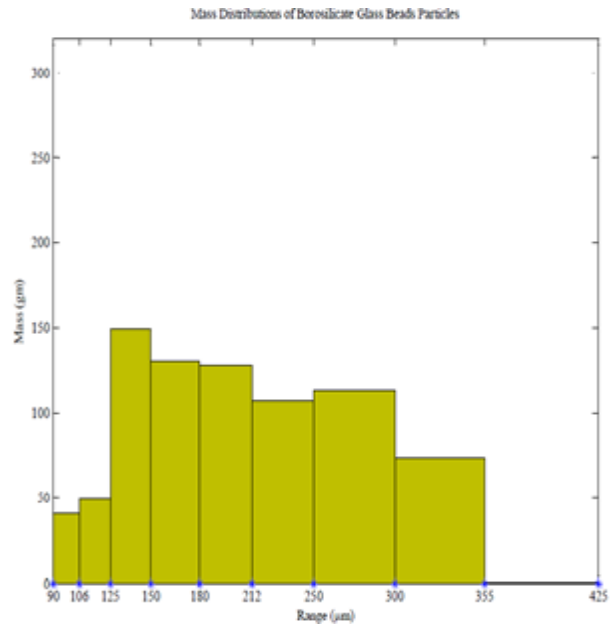


Figure 5.3: Mass distribution for Glass beads Particles.

shows the mass distributions of the particles in weight percentage. Maintaining this weight percentages, the mass of the Hematite and Borosilicate glass beads are measured. Fig. 5.2 shows the mass distribution of the Hematite particle and Fig. 5.3 shows the mass distribution of the Borosilicate glass beads particles

#### **5.1.1.2 Mass distributions for 125-300 $\mu\text{m}$ particles**

The total range of the previous arrangement of the particles is too large compare to the amount of the particles available. So a different distribution of particles is incurred maintaining same weight percent of particles for all ranges of particles from 125 to 300  $\mu\text{m}$ . This is a small range of the particles and most of the particle for both types of particle are concentrated in this range. The results of the use of these two different sets of particles are presented in the following section.

#### **5.1.2 Effect of density analysis**

Fluidized bed can be created using different types of particles, different bed diameter, and different static bed height. To analyze the effect of density, Hematite and Borosilicate glass beads particles are used. The tables below show the pressure drop of two different types of particles with the change of the superficial velocity for the 90-425  $\mu\text{m}$  range and 125-300  $\mu\text{m}$  range for both Hematite and Borosilicate glass beads. The deviation of pressure drop in percentage is highest for the 3 cm bed height for the 90-425  $\mu\text{m}$  particles. As the bed height increases the deviation of pressure drop decreases. 3 cm is small bed height compared to other two bed heights and 90-425  $\mu\text{m}$  range contains nine different ranges of particles among these ranges some of the ranges are very small. These small particles reach minimum fluidization velocity earlier and the particle bigger in size take little bit longer to reach minimum fluidization velocity. With the increase of bed height the amount of particles increase. The particles in the

middle range increases for the 90-425  $\mu\text{m}$  particles. So, when the velocity is introduced from the bottom the pressure drop provides data close to the analytical results. When the result of 90-425  $\mu\text{m}$  Hematite is compared with the result of 90-425  $\mu\text{m}$  Borosilicate glass beads, it is clear that the pressure drop to achieve minimum fluidization velocity is less than the Hematite for the same range of particles and minimum fluidization occurs earlier for less density particles. From the same composition of these two types of material it is clear that the as the density of the particles increases the pressure drop increase.

Table 5.1: Analytical and Experimental Minimum fluidization Velocity and Pressure Drop for 90-425  $\mu\text{m}$  Hematite particles

Bed Height (cm)	Analytical Min. fluidization velocity (m/sec)	Exp. Min. Fluidization Velocity (m/sec)	Analytical pressure drop (Pa)	Exp. Pressure Drop(Pa)	Deviation of Pressure Drop (%)
3	0.079	0.041	706	301.43	57.30
4	0.079	0.054	942	578.46	38.59
5	0.079	0.059	1178	785	33.36

Table 5.2: Analytical and Experimental Minimum fluidization Velocity and Pressure Drop for 90-425  $\mu\text{m}$  Borosilicate glass beads particles

Bed Height (cm)	Analytical Min. fluidization velocity, m/sec	Exp. Min. Fluidization Velocity (m/sec)	Analytical pressure drop (Pa)	Exp. Pressure Drop (Pa)	Deviation of Pressure Drop (%)
3	0.034	0.0333	391	213	45.52
4	0.034	0.0328	417	296	29.02
5	0.034	0.030	521	420	19.39

To get even better understanding of these behavior another range of particles is used for both type of materials. This range consists of materials from the range 125-300  $\mu\text{m}$ . Five different ranges exist in this range and the weight of the particles is same in every range. The results for the 125-300  $\mu\text{m}$  also shows that the pressure drop for the Hematite is higher than the Borosilicate glass beads and minimum fluidization occurs earlier in case of less density particles. The experimental results of the Hematite shows good agreement with the analytical data. In this case this is also the same thing happens, the deviation of pressure drop decrease with the increase of bed height. For the case of 125-300  $\mu\text{m}$  Borosilicate glass beads the deviation of pressure drop is slightly higher, it is probably because the density of the particles is less than the Hematite. But the experimental pressure drop is less than the Hematite as expected from the data produced from 90-425  $\mu\text{m}$  materials. So the effect of density certain in fluidized beds. As the density of the particles increases the pressure drop increase and as the density of the particles decreases the pressure drop decreases.

Table 5.3: Analytical and Experimental Minimum fluidization Velocity and Pressure Drop for 125-300  $\mu\text{m}$  Hematite particles

Bed Height (cm)	Analytical Min. fluidization velocity, m/sec	Exp. Min. Fluidization Velocity, m/sec	Analytical pressure drop (Pa)	Exp. Pressure Drop (Pa)	Deviation of Pressure Drop (%)
3	0.062	0.0495	710	406	42.82
4	0.062	0.0633	947	666	29.67
5	0.062	0.0616	1178	981	16.72

Table 5.4: Analytical and Experimental Minimum fluidization Velocity and Pressure Drop for 125-300  $\mu\text{m}$  Borosilicate glass beads particles.

Bed Height (cm)	Analytical Min. fluidization velocity (m/sec)	Exp. Min. Fluidization Velocity (m/sec)	Analytical pressure drop (Pa)	Exp. Pressure Drop (Pa)	Deviation of Pressure Drop (%)
3	0.028	0.03	368	197	46.47
4	0.028	0.036	490	311.64	36.4
5	0.028	0.045	613	412	32.79

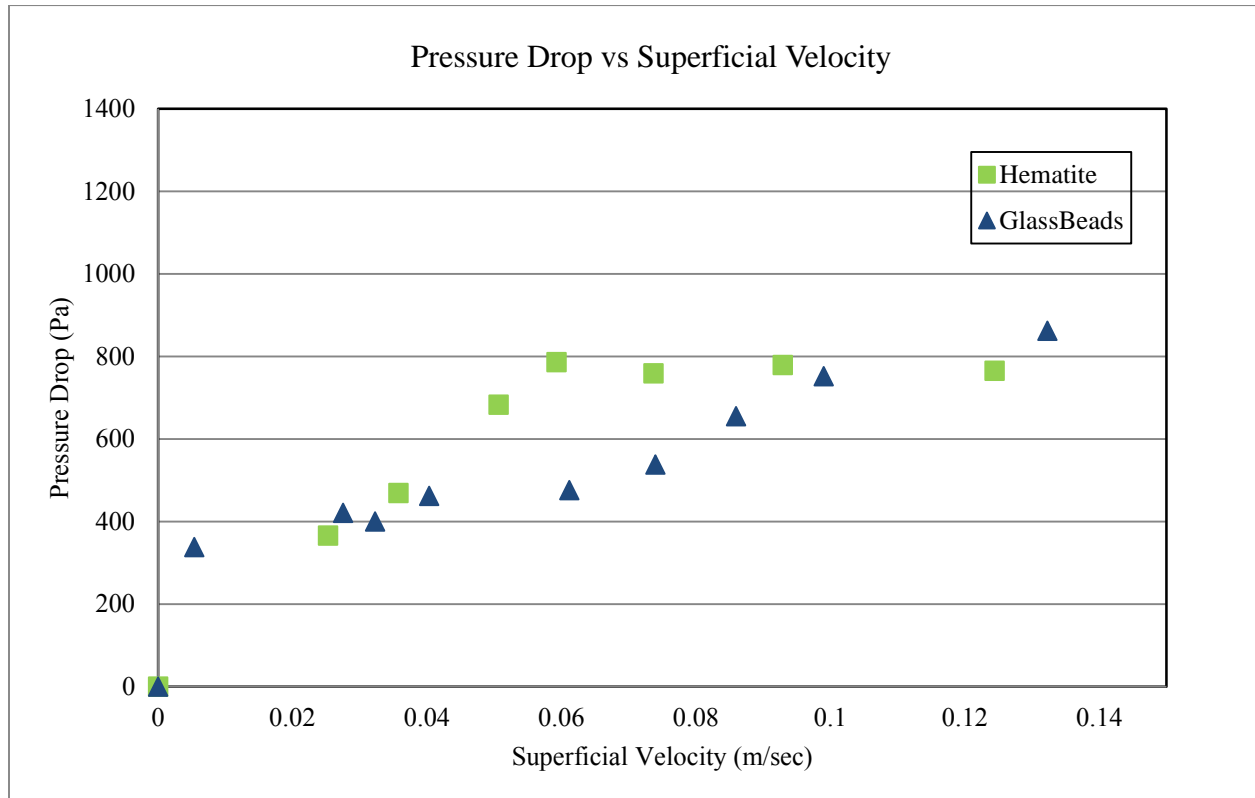


Figure 5.4: Pressure Drop vs. Superficial Velocity for 90-425  $\mu\text{m}$  particle and 5 cm bed height

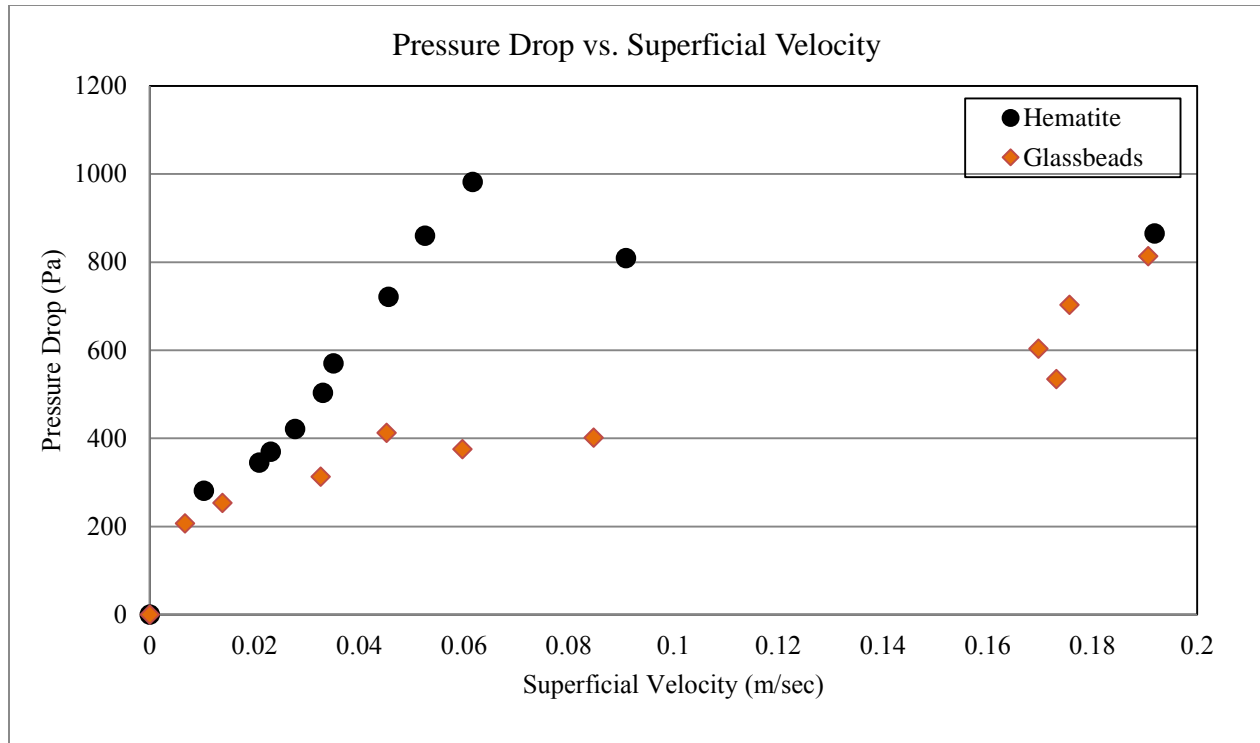


Figure 5.5: Pressure Drop vs. Superficial Velocity for 125-300  $\mu\text{m}$  particle and 5 cm bed height.

From the plot it is seen that the pressure drop for Hematite is greater than the pressure drop for Borosilicate glass beads. Due to the higher density the pressure drop is higher for the Hematite than the Borosilicate glass beads and minimum fluidization occurs earlier for less density particles.

## 5.2 Drag correlation development

Drag is the force acting on free falling particles is due to the result of velocity difference between particles and fluid. The force a flowing fluid exerts on a body in the flow direction is called drag. The drag force depends on the density  $\rho$  of the fluid, the upstream velocity  $V$ , and the size, shape and orientation of the body, among other things [61]. It is found convenient to work with appropriate dimensionless numbers or relationship dependent of few parameters are called drag coefficient. From experimentally measured terminal velocity of particles with different size Reynolds numbers were calculated with nominal diameter of particles as

characteristic length. General form of drag expression by Haider & Levenspiel [62] (Eq. 5.3) describe drag coefficient as a function for Reynolds number and sphericity where the sphericity is

$$\phi = \frac{s}{S} \quad (5.1)$$

Where  $s$  is the surface of sphere having the same volume of particle and  $S$  is the actual surface area of particles. Sphericity is a measure of how spherical or circular a particle is. We developed a drag model based on general drag expression by Haider and Levenspiel where drag coefficient is function of Reynolds number and sphericity. In our proposed model the sphericity of particles were measured as

$$\phi = \frac{d}{a} \quad (5.2)$$

Where the sphericity is the ratio of nominal diameter of particle ( $d$ ) and the largest length of the particles ( $a$ ). The general expression for drag coefficient is

$$C_D = \frac{24}{Re} (1 + AR_e^B) + \frac{C}{1 + \frac{D}{Re}} \quad (5.3)$$

In this equation there are four constants  $A$ ,  $B$ ,  $C$  and  $D$ . For different sphericities, data were fitted in Eq. 5.3. Least square method used to fit the data in the equation mentioned above. This approach minimizes the sum of the square residuals and produces the best fit curve for given values. The following table is produced using the least square method.

Table 5.5: Values of constants used in Eq. 5.3 for different sphericities to predict  $C_D$

$\phi$	A	B	C	D
0.47	1.9484	0.0062	0.9481	-0.2085
0.53	7.5902	-0.1573	0.8352	1.5798
0.58	1.1728	0.0011	1.117	-0.3684
0.63	2.2173	-0.0017	1.0178	-0.1354
0.68	2.419	-0.0134	0.8776	0.7191

Functionality between the parameter and sphericity has been established using a reasonable order of polynomial equation using the data from the Table 5.5. The following four equations have been found using the data above from Table 5.5.

$$A = \exp(-142.7123 + 555.6297\phi - 533.0938\phi^2) \quad (5.4.a)$$

$$B = 0.2004\phi - 0.1489 \quad (5.4.b)$$

$$C = \exp(47.3143 - 258.3263\phi + 464.8296\phi^2 - 275.7239\phi^3) \quad (5.4.c)$$

$$D = \exp(-161.8 + 855.9\phi - 1502\phi^2 + 870.4\phi^3) \quad (5.4.d)$$

By substituting this four values in Eq. 5.3 our final drag expression is as follow

$$C_D = \frac{24}{R_e} \left[ 1 + \exp[-142.7123 + 555.6297\phi - 533.0938\phi^2] R_e^{(0.2004\phi - 0.1489)} \right] \quad (5.5)$$

$$+ \frac{\exp(47.3143 - 258.3263\phi + 464.829\phi^2 - 275.72369\phi^3)}{1 + \frac{\exp(-161.8 + 855.9\phi - 1502\phi^2 + 870.4\phi^3)}{R_e}}$$

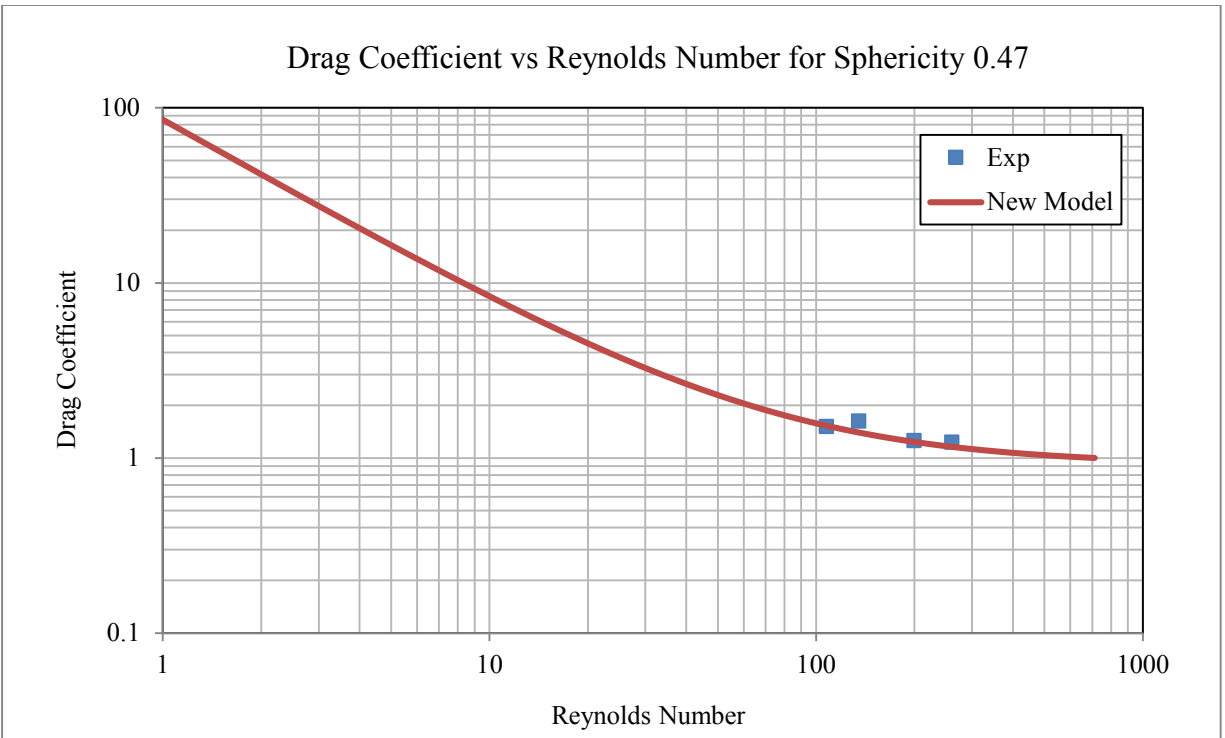


Figure 5.6: Drag coefficient vs Reynolds number for Sphericity of 0.47

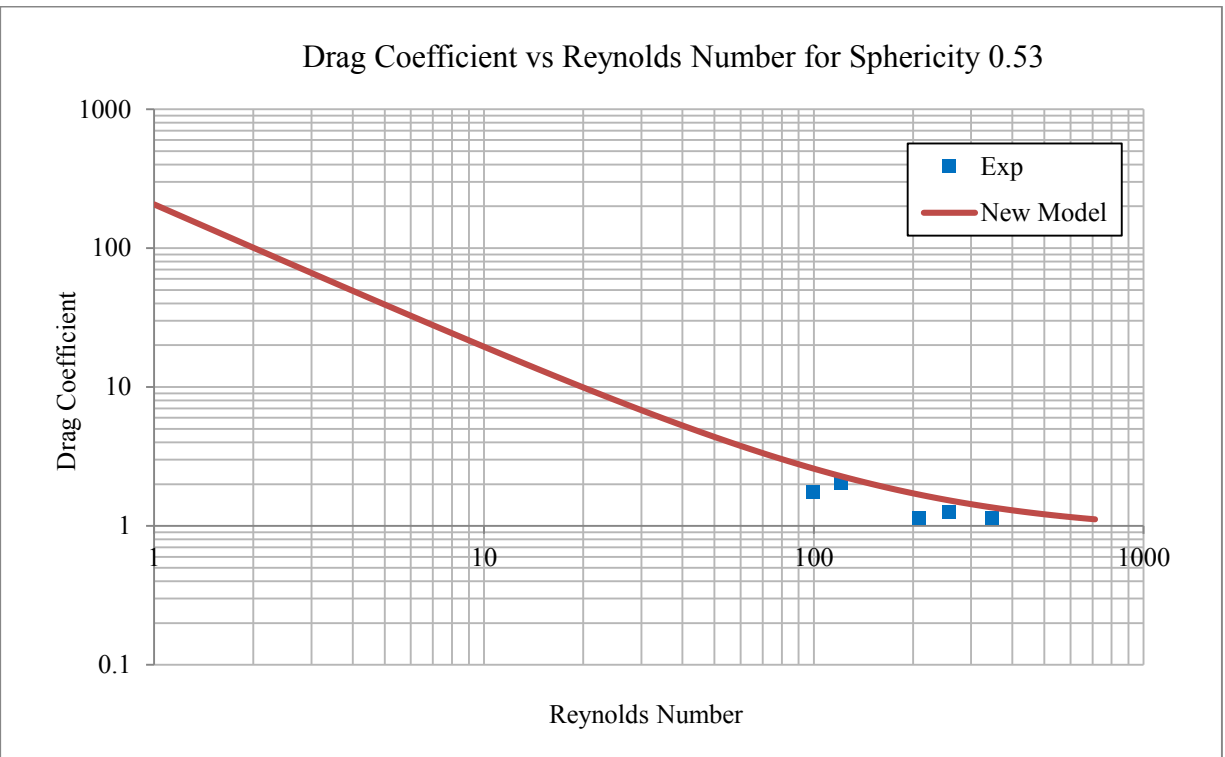


Figure 5.7: Drag coefficient vs Reynolds number for sphericity 0.53

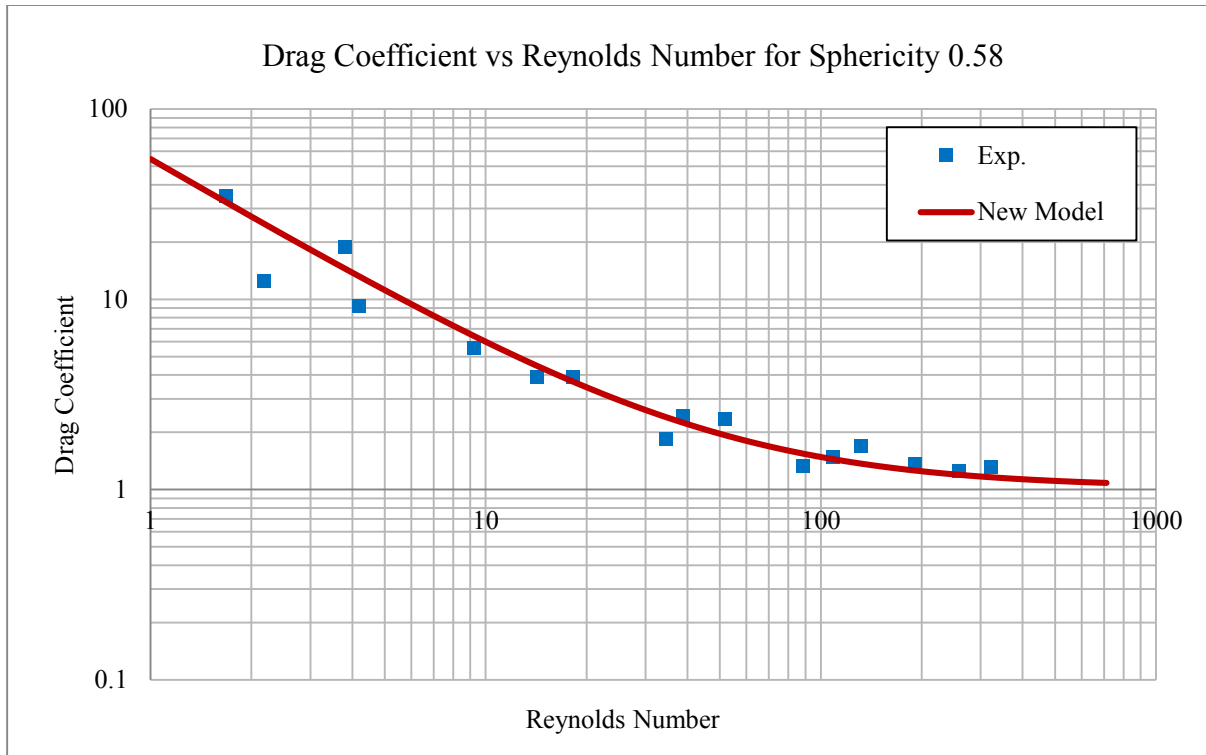


Figure 5.8: Drag coefficient vs Reynolds Number for sphericity 0.58

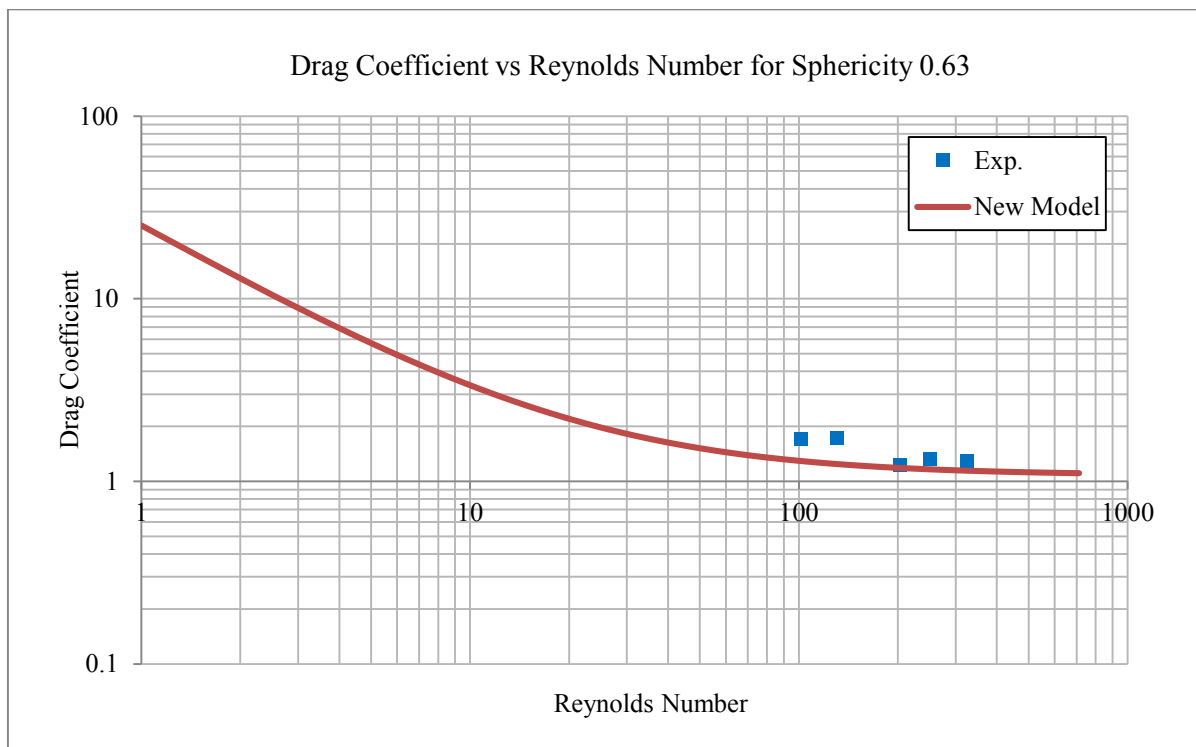


Figure 5.9: Drag Coefficient vs Reynolds Number for sphericity 0.63

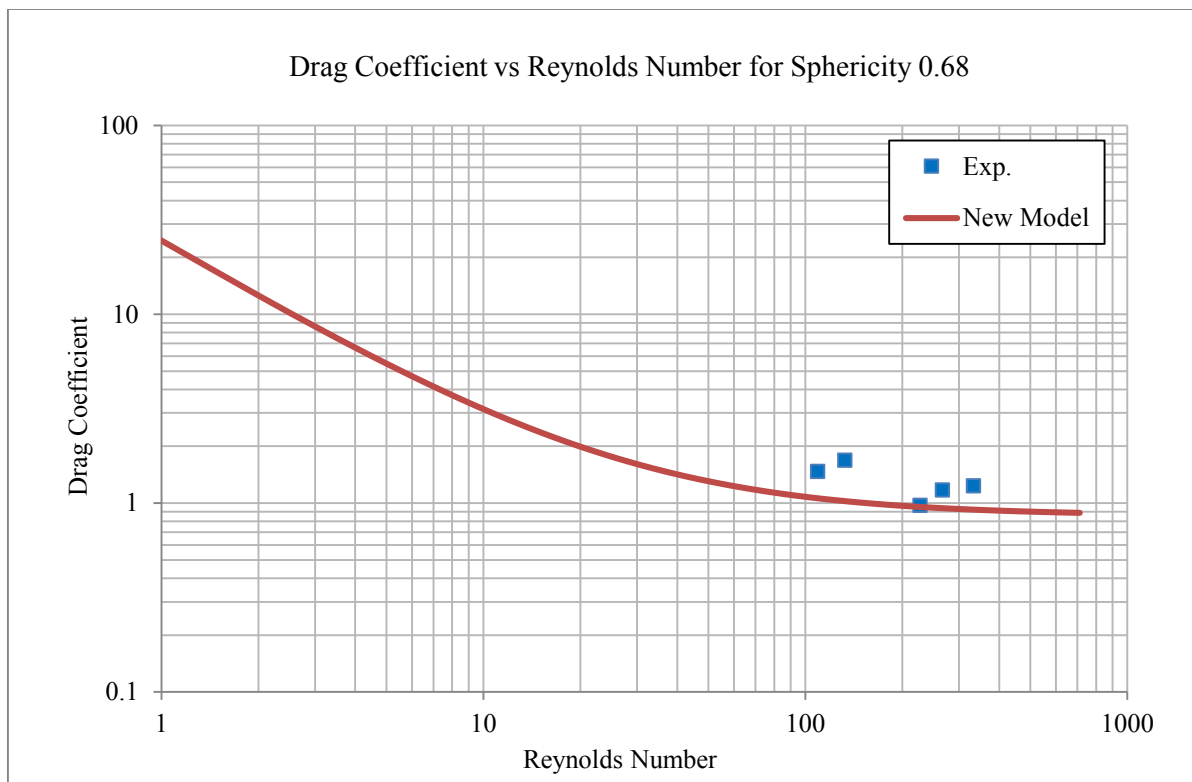


Figure 5.10: Drag Coefficient vs Reynolds Number for sphericity 0.68

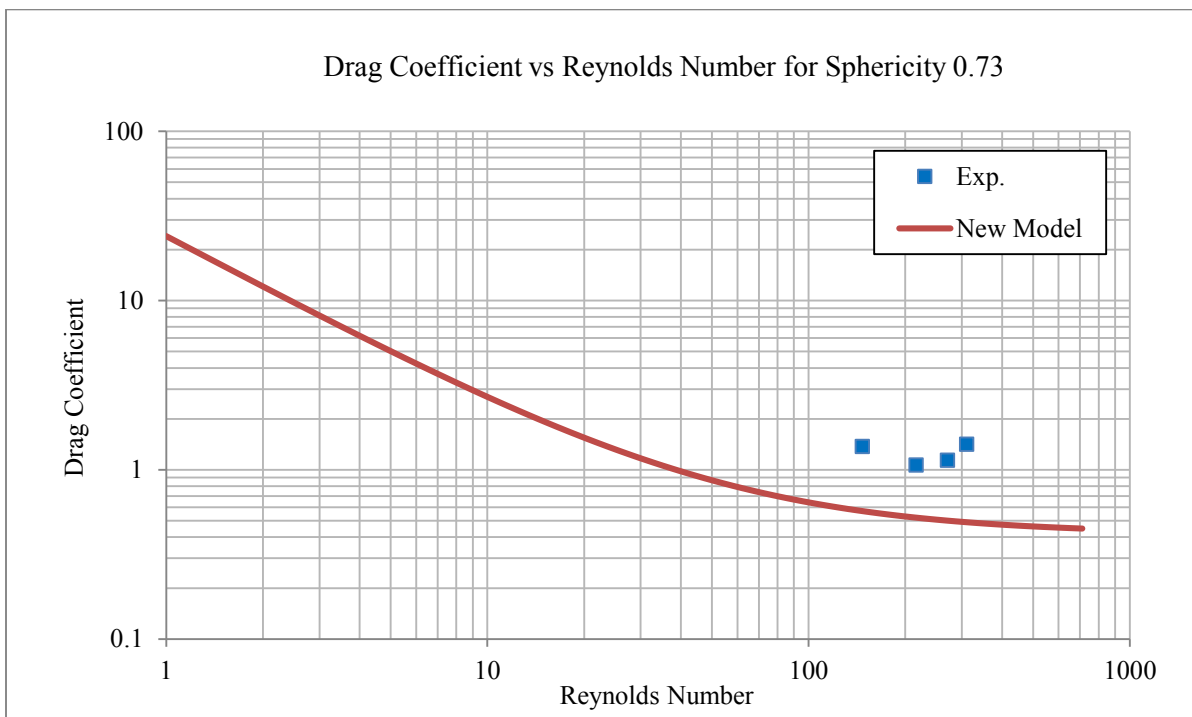


Figure 5.11: Drag Coefficient Vs Reynolds Number for sphericity 0.73

Eq. 5.5 can predict drag coefficient ( $C_D$ ) over various Reynolds number and sphericity. This model fit well from sphericity 0.43 to 0.68. Fig. 5.6-5.11 shows the plot of drag coefficient over Reynolds number for different sphericity of free falling non-spherical particles. From Fig. 5.6-5.11, it is found that our models best suits from sphericity 0.47 to 0.68. Particles over 500 microns we have different sphericity range. Particles below 500 microns the sphericity measurement and categorize them with different range is difficult. But we considered average sphericity of all ranges particles below 500 microns as 0.58 as crushed glass particles has sphericity around 0.6 [13]. Fig. 5.8 shows all data experimental data point with sphericity 0.58. All other plots in (Fig. 5.6, 5.7, 5.9, 5.10, 5.11) shows five data points with different sphericity.

### **5.3 Comparison of computational to experimental data when using spherical particles**

The computational results have been compared with the experimental results to see how close the simulation results to the experimental results. Results produced from established spherical drag models of Syamlal and O'brien [56] and Gidaspow [46] have been compared with experimental data. Pressure drop found from these two models little bit lower than the experimental results. The comparison between the results when using the boundary conditions and grid dimensions previously mentioned along with the established drag relationships and experiments is shown in Fig. 5.12. Averaging pressure drop over approximately 6s at the desired gas velocity ach datum of the Fig. 5.12 is obtained. The pressures used from the model were taken from the same location used in the experiments. The model proposed by Syamlal and O'brien [56] predicted the value of minimum fluidization, however, over predicts pressure drop after this point. Using the model by Gidaspow [46] shows that at a gas velocity of 0.2 m/s the

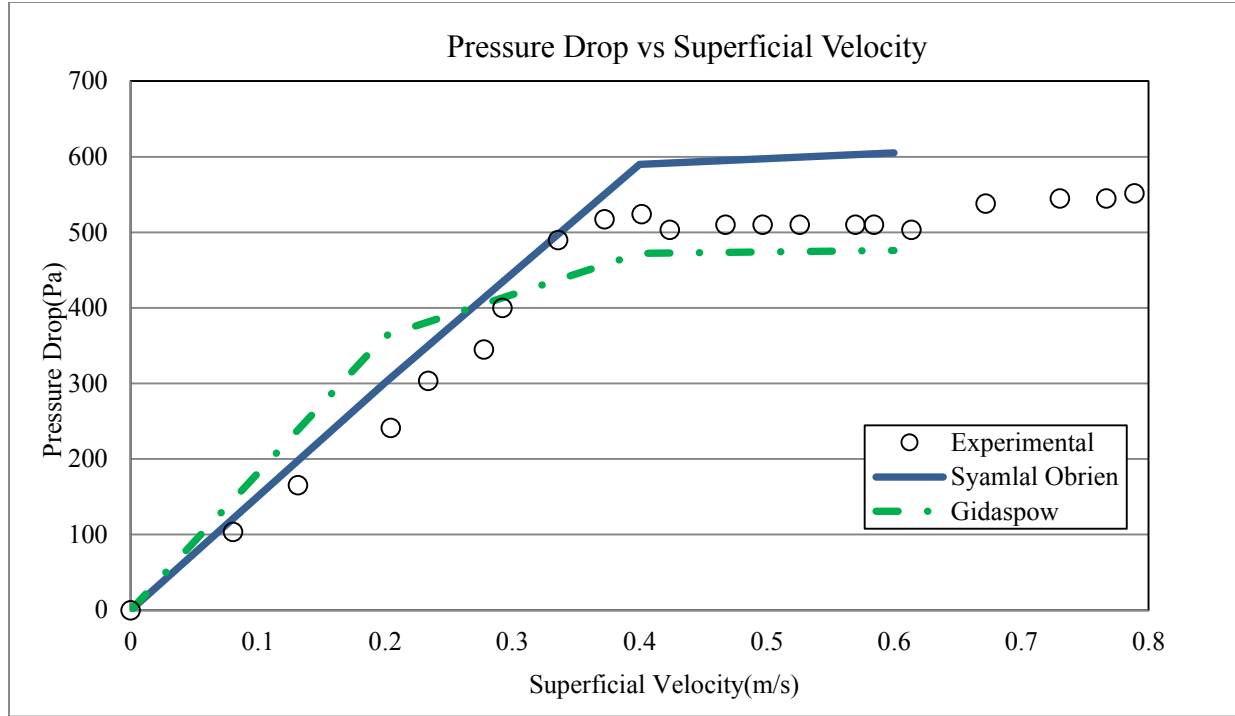


Figure 5.12: Comparison of computational to experimental data

pressure drop was over predicted compared to experiments however remains very near experimental measurement for nearly all fluid flow rates. Overall, both models did not significantly vary compared to experimental results, within  $\pm 10\%$ , this was satisfactory in order to verify the computational domain quantitatively.

#### 5.4 Qualitative comparison of bubbling behavior of particles from simulation and experiment

Fig. 5.13 shows the qualitative comparison of the fluidized bed by displaying some representative snapshots from the computational model and experiment at different times. Colliding and collapsing bubbles in the numerical simulation are observed as the gas is supplied at the bottom of the bed, the colors red and light blue indicate the volume fraction of solids in the fluidization domain, red indicating a high fraction of solid particles, while blue represents the

presence of air voids and bubbles forming in the bed. Similar hydrodynamic behavior is found in the experimental images, a qualitative agreement with respect to the numerical simulations.

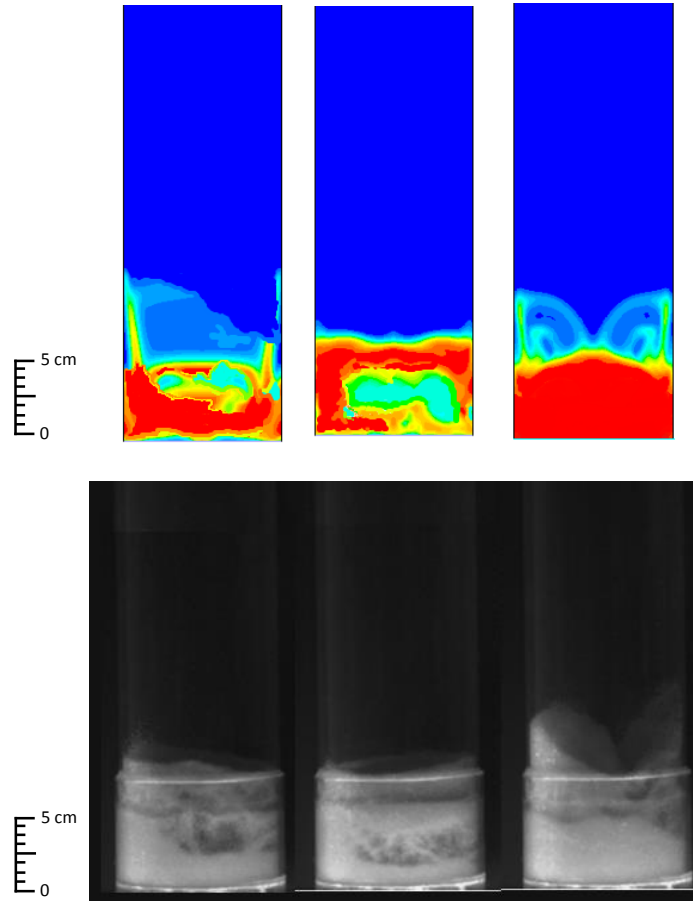
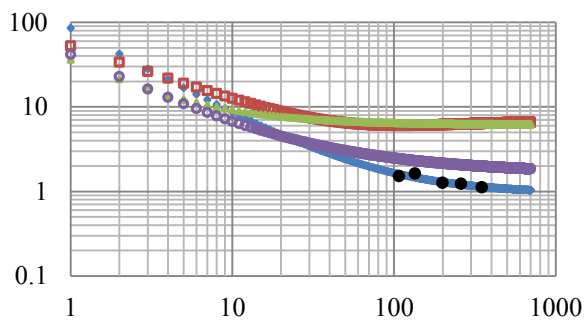


Figure 5.13: Qualitative comparison of bubbling behavior of particles from (top) simulation and experiment (bottom) at  $t = 2, 5$ , and  $7$  s from left to right

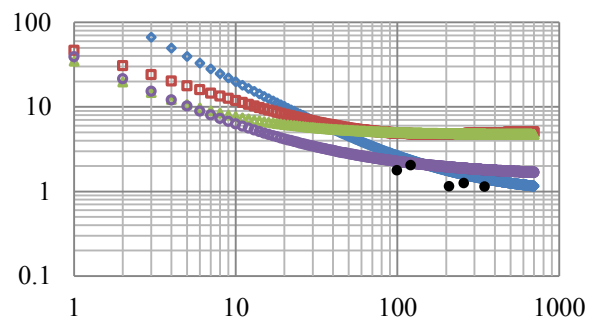
### 5.5 Plots of drag coefficient at various Reynolds numbers for different drag models and newly proposed drag model

The comparison of the correlation presented in Eq. 5.5 to other non-spherical drag models was plotted for different Reynolds numbers and is shown in Fig. 5.14. The model is compared to those found in Table 2.2 as well as with results obtained from experimental measurements in this paper. For experimental data points shown in Fig. 5.14 the Reynolds

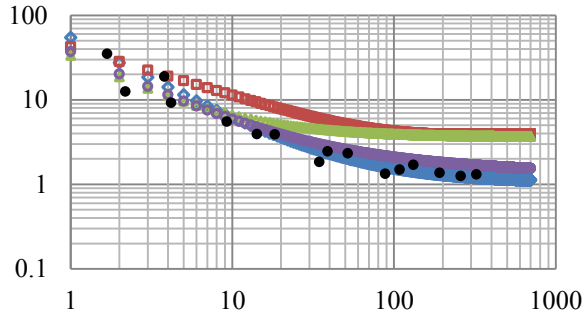
number was controlled by varying the nominal particle diameter, thus for a particular sphericity there may not have been a sufficient number of particles to test over the entire range of Reynolds numbers, this explains why the number of points measured from experiments varies for each sphericity. From Fig. 5.14a it can be seen that the drag model is very well suited to predict drag coefficients at a sphericity of 0.47 since it does not deviate from experimental data significantly. Comparison to other available drag relations show a large deviation from experiments for these models since the sphericity or particle shape is not in their applicable range. At the sphericity of 0.53 the newly proposed model again predicts the drag coefficient of particles and compared to literature values a large deviation is still observed between other relations and the present experiment. At a moderate sphericity of 0.58 the model predicted the drag coefficient accurately over a range of Reynolds numbers from 2 to 300, Fig. 5.14c. In Fig. 5.14c above a particle Reynolds number of 10 there is a significant deviation between the newly proposed drag model and those found in literature. This same trend in favor of the newly proposed model is also observed at particle sphericities of 0.63 and 0.68, Figs. 5.14d and 5.14e, respectively. The last range of particle sphericity tested was that of 0.9 and showed that the newly proposed model under predicts the value of drag coefficient above a Reynolds number of 100 with experimental values lying closer to those proposed by Holzer and Sommerfeld [41].



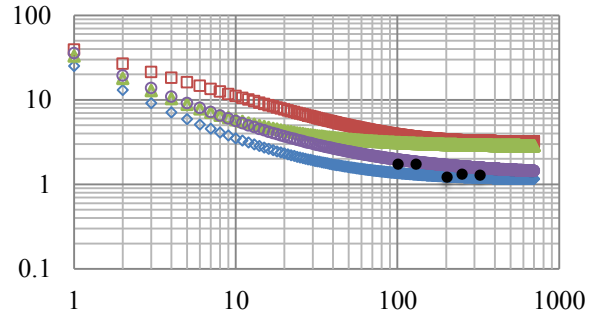
(a)



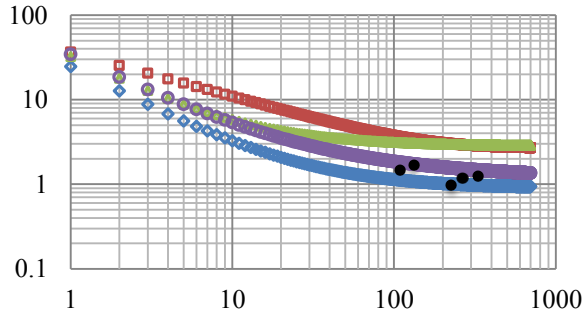
(b)



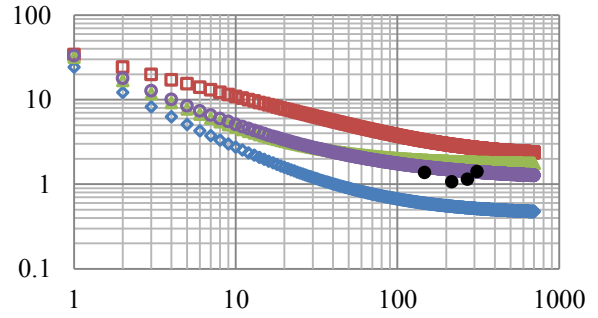
(c)



(d)



(e)



(f)

Figure 5.14: Plots of drag coefficient at various Reynolds numbers ( $<10^3$ ) for different drag models including  $\circ$  = Holzer and Sommerfeld [3],  $\square$  = Haider and Levenspiel [15],  $\Delta$  = Chien [26], and  $\diamond$  = newly proposed drag model. All are compared to experimental measurements  $\bullet$ . From top left values for sphericity ( $\phi$ ) are (a) 0.475, (b) 0.53, (c) 0.58, (d) 0.63, (e) 0.68 and (f) 0.90

Hence based on the plots the newly proposed drag correlation, Eq. 5.5 is best suited for a sphericity range between 0.47 to 0.90 for a Reynolds number range between 2 and 103 with special note that results begin to deviate at a sphericity of 0.9. This discrepancy is probably due to the broad applicable range and shapes for which the current model is applicable. For example, unlike other models which are shape specific, e.g. disc, ellipse, cube, etc., or depend on particle orientation, e.g. parallel or perpendicular to the flow, the current model depends on the broad

definition of particle sphericity which can be successfully correlated to predict drag coefficient over a broader range of shapes and sizes. Another consideration when using the current model is its practicality since it does not require definition of particle orientation relative to the flow and may be ideal for use into the two-fluid model.

## **5.6 Comparison of pressure drop versus superficial velocity using new drag model for different sphericities**

Computational results found from the simulation are used to compare with the experimental results. In the experiment pressure drop is measured 2 cm above the bed height with the change of the superficial velocity and Static bed height of the particle is 5 cm. Simulation is also run with same specification. In this simulation, 2D case is considered. It was found that the global physics behavior of a 2D and 3D simulation was very similar and indicated that 2D models could be used to reduce computational times [63]. The drag correlation developed here is compared the drag coefficient to various sources found in literature and with experiments, and then it was implemented into ANSYS Fluent through a user-defined function with the boundary conditions and assumptions mentioned previously. Fig. 5.15, 5.16 and 5.17 presents the results of pressure drop prediction for a particle bed operating on non-spherical particles compared to experiments. Fig. 5.15 closely follows experiments for a sphericity of 0.5 for nearly all data points, deviating by 37% at a flow rate of 0.3 m/s which is probably due to the amount of time used to average pressure drop in the simulations, 6s, and is expected to replicate results more closely if a longer average time is used. Fig. 5.16 presents results for mid-range sphericity of 0.65 which replicates results very closely up to minimum fluidization, then deviates up to 25% at 1.4 m/s. At the higher range of particle sphericities tested,  $\phi = 0.9$ , values were accurately predicted up to minimum fluidization where pressure drop was over predicted at a

flow rate of 0.5 m/s deviating from experiments by 28% and decreasing thereafter. Hence for all three ranges of particle sphericity, this drag model can be used to more accurately predict pressure drop and gas velocity values up to the minimum fluidization value. After the minimum fluidization gas velocity the model tends to over predict pressure drop by approximately 25% reaching a maximum at the highest sphericity of 0.9. Some discrepancies may be accounted for by increasing the amount of time used to capture the average pressure data in the computational model. Overall, implementation of this model represents a significant improvement over currently used spherical models which tend to over predict pressure drop by over 50% when used to estimate behaviors of non-spherical particles. In addition, this model successfully predicted

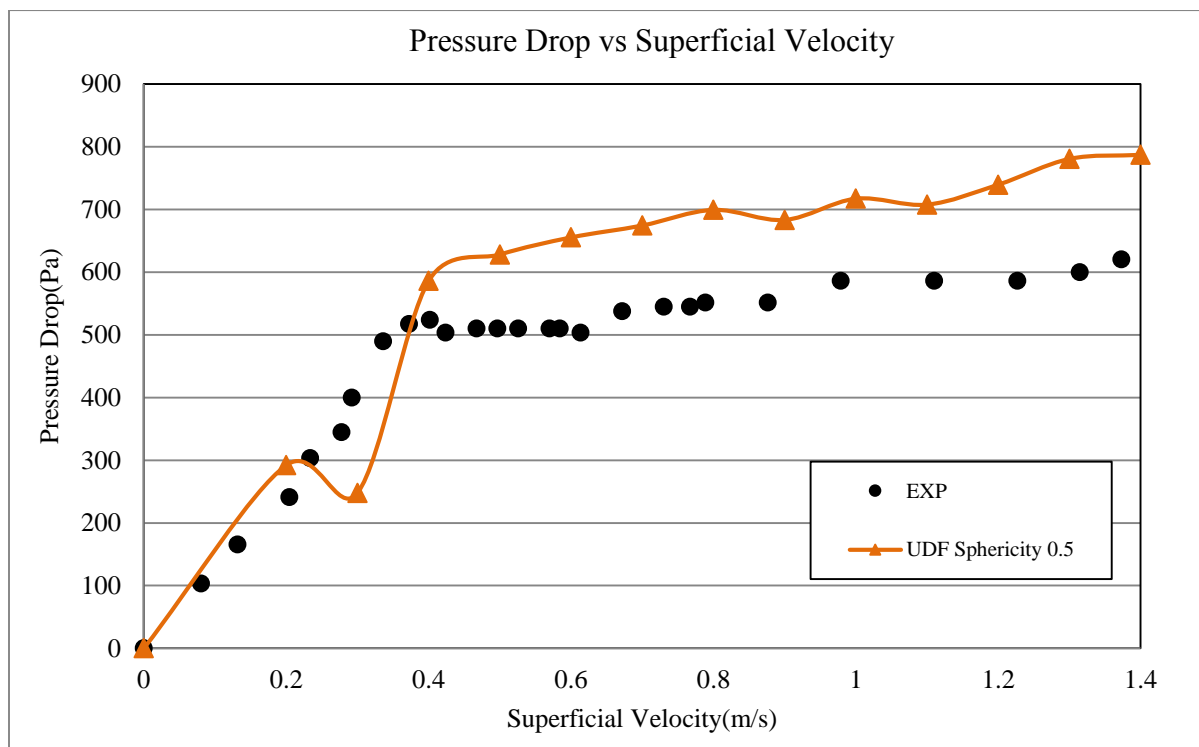


Figure 5.15: Pressure Drop vs. Superficial Velocity using developed model with sphericity 0.50

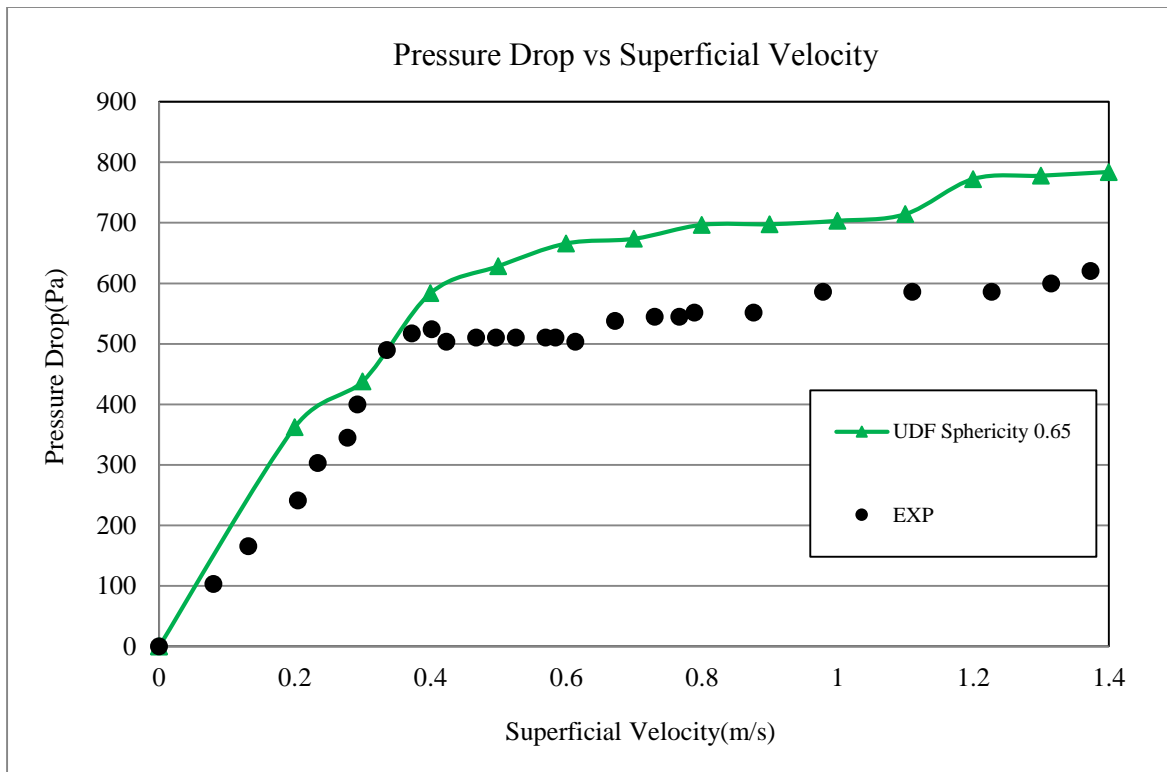


Figure 5.16: Pressure Drop vs. Superficial Velocity using developed model with sphericity 0.65

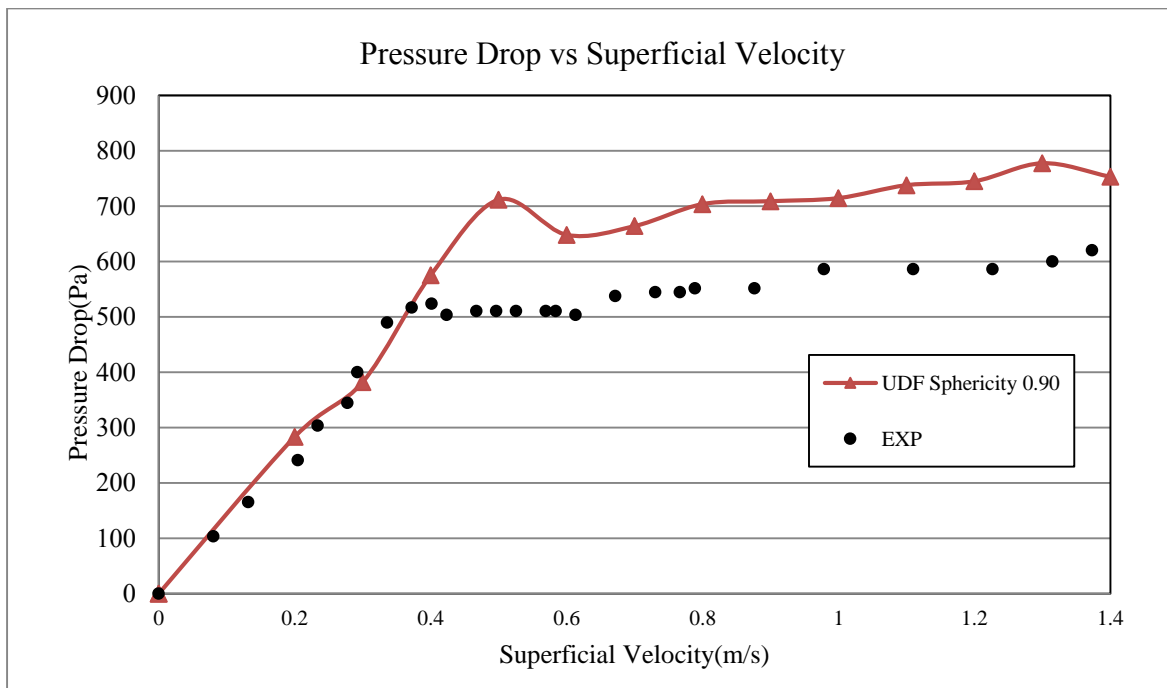


Figure 5.17: Pressure Drop vs. Superficial Velocity using developed drag model with sphericity 0.90

particle and flow behaviors, both qualitative and quantitative, for particle sphericities varying over a wide range from 0.5 to 0.9. This model is immediately applicable to computational modelers trying to more accurately predict hydrodynamics of gas-solid beds operating on realistic non-spherical particles. The following sections compare the experiment and the computational results to determine the accuracy of the computational fluid dynamics model predictions. The simulations were run for different drag model Gidaspow, Syamlal O'brien, and the drag model developed from the experiment using three different sphericities.

Table 5.6: Percent of Deviation in pressure drop at minimum fluidization

No.	Drag Model	Computational Result	Experimental Results	Percent of Deviation from the Experimental Results
1.	Developed drag model with Sphericity 0.50	585.95	523.99	11.82%
2.	Developed drag model with Sphericity 0.65	583.69	523.99	11.39%
3.	Developed drag model with Sphericity 0.90	575.10	523.99	9.75%

From Table 5.6 we can see that the percent of deviation for all the drag models. In case of Gidaspow and Syamlal O'brien model is very high. Percent of deviation for the Syamlal O'brien drag model is 94.61% and for the Gidaspow drag model is 66%. On the other hand, the developed drag model provides considerably good result. The results produced from the drag model have less percent of deviation from the experimental results.

### 5.7 Single rotating and Multiple rotating falling particles

In gas-solid two phase flows particle rotation is a very common phenomenon. In most of cases in a gas-solid two phase flow the particle used to rotate when they fall. The characteristics of rotating and multiple rotating falling particle needs to be studied. This phenomenon needs to be studied. Here we studied two cases, single particle rotation in the first case and multiple particle rotation is done in the second case. This analysis is done with help of the shadow sizer

processing system, described in section 3.5. Images of the particles are taken using the Shadow Sizer system, from these images the velocity of the particles is measured and the rotational behavior of the particles is analyzed.

### 5.7.1 Single rotating particle

The analysis will begin with the single rotating particle. Fig. 5.18 shows the pictures of falling particles. The particle enters in the first frame (Fig. 5.18a) and leaves the frame in the last image (Fig. 5.18d). Mean diameter of the particle is 0.00078 m, analyzing these images the velocity is found 4.86 m/s.

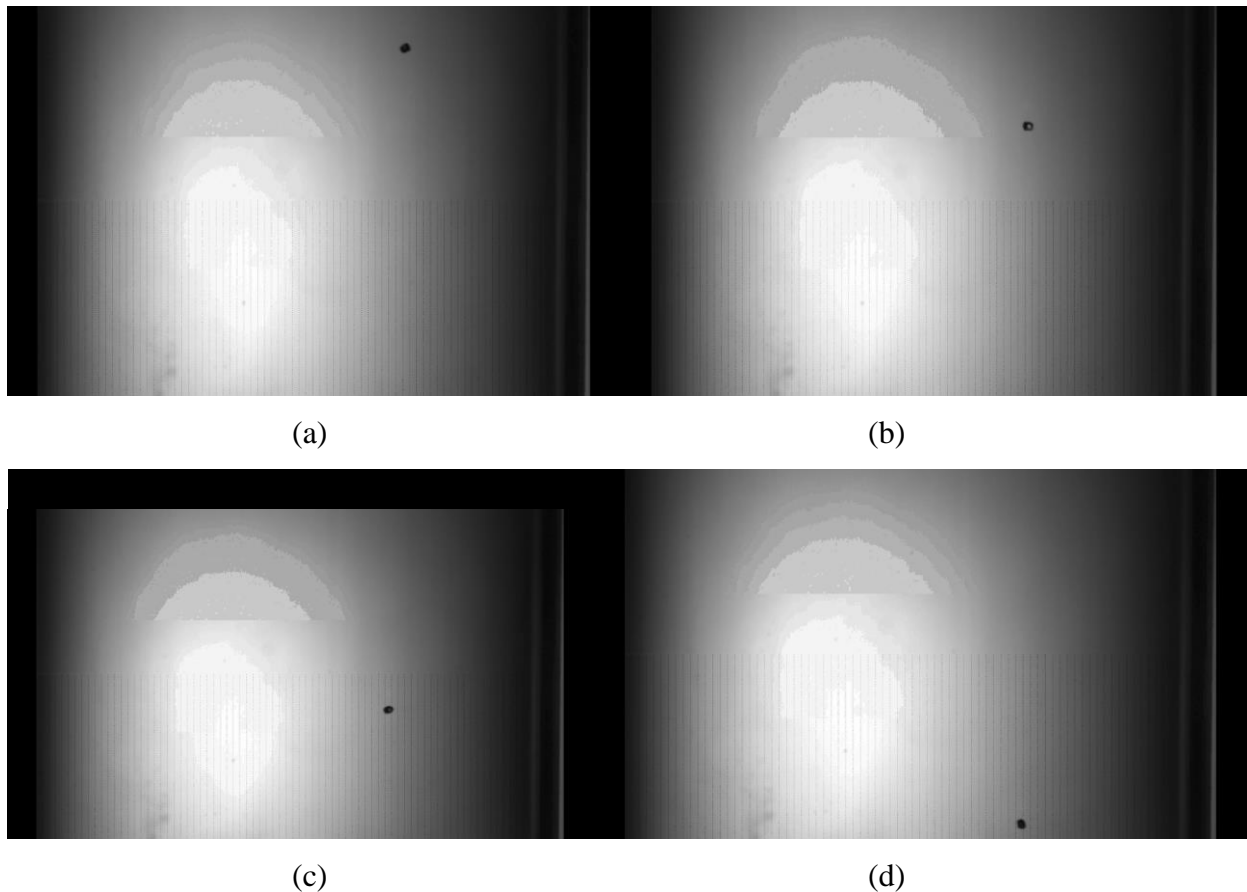


Figure 5.18: Images of the single rotating falling particle.

The experimental values of the Reynolds number and the drag coefficient are the following. The numerical value of the drag coefficient is found using the Eq. 5.5.

Table 5.7: Single rotational particle's experimental and numerical values

$D_{mean}$	Sphericity, $\phi$	$Re_{exp}$	$C_{D,exp}$	$C_{D,eqn}$
0.00078 m	0.58	2500.89	0.8	1.25

From the Table 5.7 it can be seen that the drag coefficient value found from the Eq. 5.5 is higher than the experimental value of the drag coefficient. The experimental value of the drag coefficient is lower than the value produced from the equation. For rotating particle it predicted a 36% higher value than the experimental value. This is likely due to the rotation of the particles and future work needs to be done to further analyze this.

### 5.7.2 Multiple rotating particles

For the multiple particles the same experiment is done. The four particles shown in Fig. 5.19 are the shadow sizing images of the particles. All these particles are rotating as they are falling. The experimental drag coefficient and the drag coefficient found from the Eq. 5.5 are shown in Table 5.8. It can be seen from the Table 5.8 that the drag coefficient from the equation is over predicted. For the multiple particles we again see the effect of drag coefficient. Particles 3 and 4 have a significantly higher drag coefficient than particles 1 and 2. From Table 5.8 it is seen that particle 3 and particle 4 have drag coefficient almost 10% more than the particles following them. In addition to the effect of rotation there is also an observable effect by the wake of the upstream particles. Future work needs to be done to analyze the drag coefficient of the multiple particles as it is beyond the scope of the current thesis.

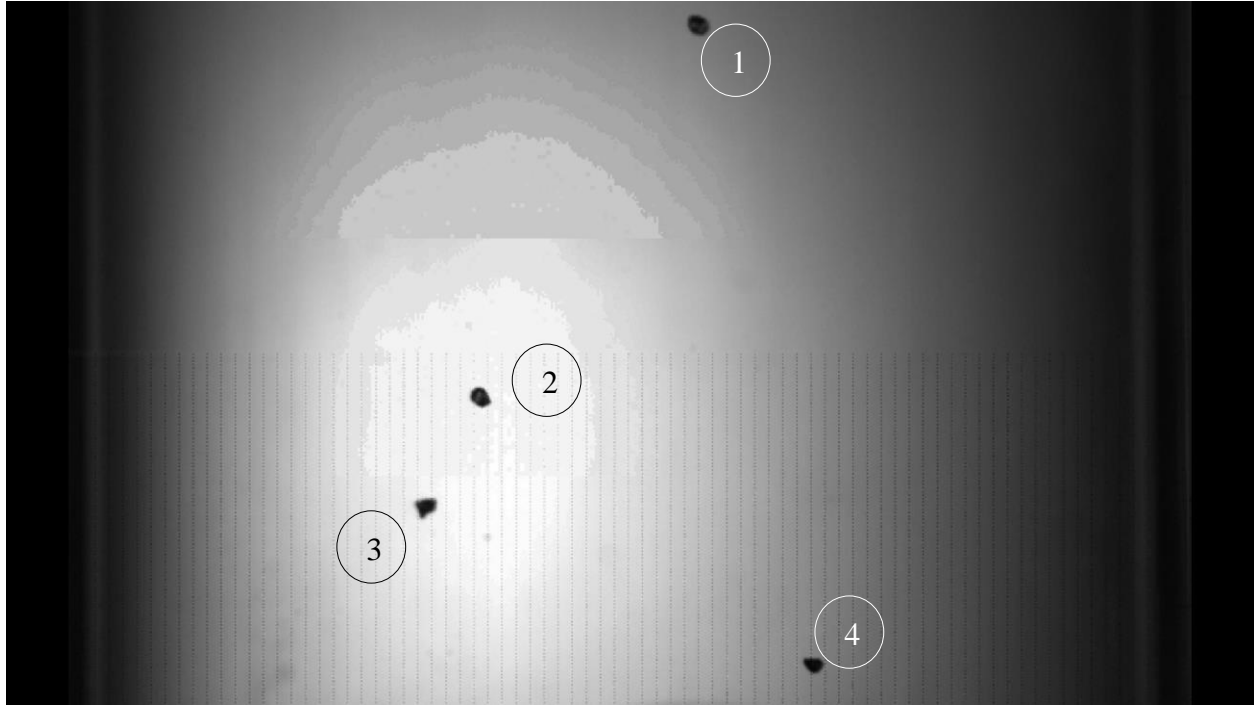


Figure 5.19: Image of multiple rotation falling particles

Table 5.8: Multiple rotational particles experimental and numerical values

Particle	$D_{mean}$	Sphericity, $\phi$	$Re_{exp}$	$C_{D,exp}$	$C_{D,eqn}$
1	0.000925 m	0.68	433.28	0.37	0.95
2	0.000655 m	0.68	256.68	0.54	0.99
3	0.00078 m	0.63	336.54	0.44	1.19
4	0.00055 m	0.68	196.30	0.65	1.01

## **Chapter 6 : Conclusion & Future Work**

### **6.1 Conclusion**

More than thousands of fluidized beds are operating around the world. Increasing the efficiency of the fluidized bed would save us a lot of energy. The following are some of the areas studied in this thesis: the effect of density in a gas-solid fluidized bed is studied, a new drag model is developed which includes sphericity term, and the drag model is then implemented in ANSYS Fluent 13.0 and compared with the experimental results.

Analyzing the hydrodynamic behavior of the fluidized bed is necessary. It is directly related to efficient of the fluidized bed. Here the hydrodynamic behavior of the fluidized bed is observed with changing the density of the particles. Borosilicate glass beads and the hematite are the two types of particles used to determine the effect of density in a gas-solid fluidized bed. From the experiment it is found that bed pressure drop increases with the increase of particle density. The particle with less density tends to reach minimum fluidization velocity earlier than the particles with more density. These are valuable insights about the hydrodynamic behavior of the fluidized bed is found from the results from the experiments.

A new drag model is developed from the experiment using MATLAB, which included the sphericity term. Sphericity is measured for different ranges of particles. The terminal velocity of the particles are measured from the experiment. Drag coefficient and the Reynolds number were measured from the terminal velocity found from the experiment. These values of the drag coefficient and the Reynolds number are used to find the new drag correlation. The general form of the equation is taken from the literature which is mentioned in the text. A nonlinear least square regression method is used to find the final form of the equation. Putting the value of the sphericity will provide the final equation for each sphericity. Very little can be found in the

literature about the drag correlation which considers sphericity. It was a unique model which determines the drag of the particles considering sphericity. So development of the drag model was a noble work which can be used in many different applications.

The drag correlation developed here was implemented in ANSYS Fluent 13.0. Implementation of the drag model in a computational code is very important part of the thesis. This drag correlation was implemented into ANSYS Fluent 13.0 using C++ software. New drag model produces much better results than existing drag models. Results found from implementing the drag model with different sphericity in mentioned in the Results and Discussion section.

With the increase of the computational capabilities lot of the systems are design and tested using computational domain. Fluidized bed involved numerous parameters with complicity. Assumptions are made to run the simulation. There are many areas regarding the fluidized bed needs to be developed to achieve more accuracy in results. Sphericity is a valuable addition to the computational research. This will allow us to consider the effect of the irregular shape of the particle for simulation. Not only fluidized bed, this drag correlation can be used in other purposes, such as pharmaceuticals.

The implementation of the drag correlation in ANSYS Fluent 13.0 is also a very good accomplishment. In this thesis, implementation of the drag correlation has been shown, which demonstrates the experiment and the development of the drag model and at the end implementation of this in a computational code. I believe, the work done here will help the future researcher to analyze and design the fluidized bed.

## **6.2 Future Work**

Analysis is recommended on the effect of particle density for two types of particles. Other types of particles can be used to see the effect of density. Only cylindrical bed is used for

the current experiment. Different bed geometries like the rectangular bed and cylindrical bed with conical shape bottom can be used to investigate bed hydrodynamics. Another area of research can be looking at the particles rotation and orientation, if it has any effect on the particle simulation inside the fluidized bed.

This research is done using two fluid model, discrete element method can be used to for the fluidized bed simulation. The drag model developed here can be implemented in the discrete element method. MFiX (Multiphase Flow with Interphase eXchanges) is one of the tools developed by Department of Energy which uses the discrete element method for the particle simulation. Particle simulation can be done using MFiX, and the drag model can be implemented in MFiX.

## References

- [1] “Clean Coal Research Department of Energy.” [Online]. Available: <http://energy.gov/fe/science-innovation/clean-coal-research>. [Accessed: 08-Jul-2014].
- [2] R. M. Flores, *Coal and Coalbed Gas: Fueling the Future (Google eBook)*. Newnes, 2013, p. 720.
- [3] “Gasification | Department of Energy.” [Online]. Available: <http://energy.gov/fe/science-innovation/clean-coal-research/gasification>. [Accessed: 08-Jul-2014].
- [4] “Fluidized Bed Reactors - Reactors - MEL Equipment Encyclopedia 4.0.” [Online]. Available: <http://encyclopedia.che.engin.umich.edu/Pages/Reactors/FBR/FBR.html>. [Accessed: 08-Jul-2014].
- [5] C. E. Brennen, *Fundamentals of Multiphase Flow*. Cambridge: Cambridge University Press, 2005, pp. 19–20.
- [6] S. Limtrakul, A. Chalermwattanatai, K. Unggurawirote, Y. Tsuji, T. Kawaguchi, and W. Tanthapanichakoon, “Discrete particle simulation of solids motion in a gas–solid fluidized bed,” *Chem. Eng. Sci.*, vol. 58, no. 3–6, pp. 915–921, Feb. 2003.
- [7] C. T. Crowe, *Multiphase Flow Handbook*. Boca Raton: CC Press Taylor & Francis Group, 2006.
- [8] S. Limtrakul, A. Chalermwattanatai, K. Unggurawirote, Y. Tsuji, T. Kawaguchi, and W. Tanthapanichakoon, “Discrete particle simulation of solids motion in a gas–solid fluidized bed,” *Chem. Eng. Sci.*, vol. 58, no. 3–6, pp. 915–921, Feb. 2003.
- [9] D. R. Breault, “National Energy Technology Laboratory’s (NETL’s),” in *Turkish-American Clean Energy Conference*, 2008.
- [10] F. H. Hutchison, “Clean-Energy.US,” 2009. [Online]. Available: <http://www.clean-energy.us/facts/gasification.htm>.
- [11] PeakGraphic, “Process Energy Solutions.” [Online]. Available: <http://www.bqpes.com/gasification-tech-history.php>. [Accessed: 19-Mar-2014].
- [12] D. R. Escudero, “Bed height and material density effects on fluidized bed hydrodynamics,” 2010.
- [13] W.-C. Yang, *Handbook of Fluidization and Fluid-Particle Systems*. New York: Marcel Dekker, Inc., 2003.
- [14] C. T. Crowe, *MULTIPHASE FLOW HANDBOOK*. Boca Raton: CRC Press, Taylor & Francis Group, 2006, pp. 5–4.
- [15] R. K. Niven, “Physical insight into the Ergun and Wen & Yu equations for uid ow in packed and uidised beds,” vol. 57, pp. 527–534, 2002.
- [16] L. Li and W. Ma, “Experimental Study on the Effective Particle Diameter of a Packed Bed with Non-Spherical Particles,” pp. 35–48, 2011.
- [17] W. McCabe, J. Smith, and P. Harriott, *Unit Operations of Chemical Engineering*. New York City: Mc Graw Hill Education, 2008.

- [18] D. Geldart and R. R. Cranfield, "The gas fluidisation of large particles," *Chem. Eng. J.*, vol. 3, pp. 211–231, Jan. 1972.
- [19] S. Park, "The expansion of gas-fluidised beds in bubbling fluidisation," vol. 52, no. 16, 1997.
- [20] B. N. Hilal, M. T. Ghannam, and M. Z. Anabtawi, "Effect of Bed Diameter , Distrubutor and Inserts on Minimum Fluidization Velocity," *Chem. Eng. Technol.*, vol. 24, pp. 161–165, 2001.
- [21] C.-L. Lin, M.-Y. Wey, and S.-D. You, "The effect of particle size distribution on minimum fluidization velocity at high temperature," *Powder Technol.*, vol. 126, no. 3, pp. 297–301, Aug. 2002.
- [22] J. J. P. Marque, "Minimum fluidization v elocities for gas Á solid 2D beds Guadalupe Ramos Caicedo \*, Mo," vol. 41, pp. 761–764, 2002.
- [23] W. Zhong, X. Chen, and M. Zhang, "Hydrodynamic characteristics of spout-fluid bed: Pressure drop and minimum spouting/spout-fluidizing velocity," *Chem. Eng. J.*, vol. 118, no. 1–2, pp. 37–46, May 2006.
- [24] D. C. Sau, S. Mohanty, and K. C. Biswal, "Minimum fluidization velocities and maximum bed pressure drops for gas–solid tapered fluidized beds," *Chem. Eng. J.*, vol. 132, no. 1–3, pp. 151–157, Aug. 2007.
- [25] A. Rao, J. S. Curtis, B. C. Hancock, and C. Wassgren, "The Effect of Column Diameter and Bed Height on Minimum Fluidization Velocity," vol. 56, no. 9, 2010.
- [26] D. Escudero and T. J. Heindel, "Bed height and Material density effects on Minimum Fluidization Velocity in a Cylindrical Fluidized Bed.pdf," in *7th International Conference on Multiphase Flow*, 2010, pp. 1–6.
- [27] A. Brucato, F. Grisafi, and G. Montante, "Particle drag coefficients in turbulent fluids," vol. 53, no. 18, pp. 3295–3314, 1998.
- [28] R. P. Chhabra, L. Agarwal, and N. K. Sinha, "Drag on non-spherical particles : an evaluation of available methods," no. March 1998, pp. 288–295, 1999.
- [29] K. Ceylan, S. Herdem, and T. Abbasov, "A theoretical model for estimation of drag force in the flow of non-newtonian fluids around spherical solid particles," pp. 286–291, 1999.
- [30] S. Tran-Cong, M. Gay, and E. E. Michaelides, "Drag coefficients of irregularly shaped particles," *Powder Technol.*, vol. 139, no. 1, pp. 21–32, Jan. 2004.
- [31] H. N. Yow, M. J. Pitt, and A. D. Salman, "Drag correlations for particles of regular shape," *Adv. Powder Technol.*, vol. 16, no. 4, pp. 363–372, Aug. 2005.
- [32] E. Loth, "Drag of non-spherical solid particles of regular and irregular shape," vol. 182, pp. 342–353, 2008.
- [33] J. P. Hsu, S. J. Yeh, and S. Tseng, "Drag on a sphere in a spherical dispersion containing Carreau fl uid," *Powder Technol.*, vol. 188, no. 1, pp. 34–41, 2008.
- [34] J. Gabitto and C. Tsouris, "Drag coefficient and settling velocity for particles of cylindrical shape," vol. 183, pp. 314–322, 2008.

- [35] M. Zastawny, G. Mallouppas, F. Zhao, and B. Van Wachem, "International Journal of Multiphase Flow Derivation of drag and lift force and torque coefficients for non-spherical particles in flows," *Int. J. Multiph. Flow*, vol. 39, pp. 227–239, 2012.
- [36] A. Terfous, A. Hazzab, and A. Ghenaim, "Predicting the drag coefficient and settling velocity of spherical particles," *Powder Technol.*, vol. 239, pp. 12–20, 2013.
- [37] R. Barati, S. Ali, A. Salehi, and G. Ahmadi, "Development of empirical models with high accuracy for estimation of drag coefficient of flow around a smooth sphere: An evolutionary approach," *Powder Technol.*, vol. 257, pp. 11–19, 2014.
- [38] A. Haider and O. Levenspiel, "HaiderLevenspielPT1989.pdf," *Drag Coeff. Termin. Veloc. Spherical Nonspherical Part.*, vol. 58, pp. 63–70, 1989.
- [39] G. H. Ganser, "A rational approach to drag prediction of spherical and nonspherical particles," *Powder Technol.*, vol. 77, no. 2, pp. 143–152, Nov. 1993.
- [40] S. Chien, "Settling Velocity of Irregularly Shaped Particles," *Soc. Pet. Eng. Dilling Complet.*, vol. 9(4), pp. 281–289, 1994.
- [41] A. Hölzer and M. Sommerfeld, "New simple correlation formula for the drag coefficient of non-spherical particles," *Powder Technol.*, vol. 184, no. 3, pp. 361–365, Jun. 2008.
- [42] a M. Brown, "A step-by-step guide to non-linear regression analysis of experimental data using a Microsoft Excel spreadsheet.," *Comput. Methods Programs Biomed.*, vol. 65, no. 3, pp. 191–200, Jun. 2001.
- [43] A. M. Brown, "A non-linear regression analysis program for describing electrophysiological data with multiple functions using Microsoft Excel.," *Comput. Methods Programs Biomed.*, vol. 82, no. 1, pp. 51–7, Apr. 2006.
- [44] G. J. Tsekouras, E. N. Dialynas, N. D. Hatziaargyriou, and S. Kavatza, "A non-linear multivariable regression model for midterm energy forecasting of power systems," *Electr. Power Syst. Res.*, vol. 77, no. 12, pp. 1560–1568, Oct. 2007.
- [45] C. F. Mora, A. K. H. Kwan, and H. C. Chan, "PARTICLE SIZE DISTRIBUTION ANALYSIS OF COARSE AGGREGATE USING DIGITAL IMAGE PROCESSING," *Pergamon*, vol. 28, no. 6, pp. 921–932, 1998.
- [46] H. Wadell, "Volume, Shape, and Roundness of Rock Particles," *J. Geol.*, vol. 40, no. 5, pp. 443–451, Jul. 1932.
- [47] W. C. s. l. Krumbein, "Measurement and Geological Significance of Shape and Roundness of Sedimentary particles," *J. Sediment. Petrol.*, vol. 11, pp. 64–72, 1941.
- [48] W.-C. Yang, *HANDBOOK of FLUIDIZATION and FLUID-PARTICLE SYSTEMS* edited by Wen-Ching Yang. Pittsburgh, 2003.
- [49] F. Berruti and N. Kalogerakis, "Modelling the internal Flow Structure of Circulating Fluidized Beds.," *Can. J. Chem. Eng.*, vol. 67, no. 6, pp. 1010–1014, 1989.
- [50] R. S. Laramee, H. Hauser, H. Doleisch, B. Vrolijk, F. H. Post, and D. Weiskopf, "The State of the Art in Flow Visualization: Dense and Texture-Based Techniques," *Comput. Graph. Forum*, vol. 23, no. 2, pp. 203–221, Jun. 2004.

- [51] J. J. van Wijk, "Image based flow visualization," *ACM Trans. Graph.*, vol. 21, no. 3, pp. 745–754, Jul. 2002.
- [52] "FLOW VISUALIZATION BY MEANS OF SINGLE-EXPOSURE SPECKLE PHOTOGRAPHY," *Opt. Commun.*, vol. 37, no. 5, pp. 326–330, 1981.
- [53] "DANTEC DYNAMICS A/S," 2013. [Online]. Available: <http://www.dantecdynamics.com/shadow-sizing>. [Accessed: 07-May-2014].
- [54] R. H. Sarker, A. S. M. R. R. Chowdhury, N. Love, and A. Choudhuri, "Flow Field Visualization and Drag Analysis of Particles in a Gas - Solid Fluidized Bed Using a Non - Intrusive Optical Technique," in *51st AIAA Aerospace Sciences Meeting Including the New Horizons Forum and Aerospace Exposition*, 2013, pp. 1–12.
- [55] a. Passalacqua and L. Marmo, "A critical comparison of frictional stress models applied to the simulation of bubbling fluidized beds," *Chem. Eng. Sci.*, vol. 64, no. 12, pp. 2795–2806, Jun. 2009.
- [56] D. Gidaspow, R. Bezburuah, and J. Ding, "Hydrodynamics of Circulating Fluidized Beds: Kinetic Theory Approach," in *7th International Conference on Fluidization*, 1992, pp. 75–82.
- [57] F. Flow and T. Packed, "Chemical Engineering Progress s," *Fluid Flow Through Packed Columns*, vol. 48 (2)., pp. 89–94, 1952.
- [58] W. C and Y. Y., "Mechanics of Fluidization," in *Chemical Engineering Progress Symposium Series*, 1966, pp. 100–111.
- [59] *ANSYS FLUENT Theory Guide*, 13.0 ed., vol. 15317, no. November. Canonsburg: ANSYS, Inc., 2010, pp. 49–50.
- [60] M. Syamlal and T. O'Brien, "Computer Simulation of Bubbles in a Fluidized Bed," in *AIChE Symposium Series.*, 1989, pp. 22–31.
- [61] Y. Cengel and J. Cimbala, *FLUID MECHAICS FUNDAMENTALS AND APPLICATIONS*. New York: McGraw-Hill, 2006, pp. 563–566.
- [62] A. Haider and O. Levenspiel, "Drag coefficient and terminal velocity of spherical and nonspherical particles," *Powder Technol.*, vol. 58, no. 1, pp. 63–70, May 1989.
- [63] I. Hulme, E. Clavelle, L. Van Der Lee, and A. Kantzas, "CFD Modeling and Validation of Bubble Properties for a Bubbling Fluidized Bed," pp. 4254–4266, 2005.

## Glossary

$\varepsilon_g$	=	Gas void fraction	[-]
$\varepsilon_s$	=	Solid void fraction	[-]
$\phi$	=	Sphericity	[-]
$\gamma_s$	=	Granular energy dissipation term	[kg/m-s <sup>3</sup> ]
$\kappa_s$	=	Granular energy conductivity	[kg/m-s]
$\lambda_s$	=	Granular bulk viscosity	[kg/m-s]
$\Psi$	=	Dissipation of granular energy	[kg/m-s <sup>3</sup> ]
$\Theta_s$	=	Granular energy	[m <sup>2</sup> /s <sup>2</sup> ]
$\mu_g$	=	Gas viscosity	[kg/m-s]
$\mu_s$	=	Particulate phase viscosity	[kg/m-s]
$\rho_f$	=	Fluid density	[kg / m <sup>3</sup> ]
$\rho_g$	=	Gas density	[kg / m <sup>3</sup> ]
$\tau_g$	=	Gas phase stress tensor	[kg/m-s <sup>2</sup> ]
$\tau_s$	=	Solid phase stress tensor	[kg/m-s <sup>2</sup> ]
$A$	=	Particle surface area	[m <sup>2</sup> ]
$C_D$	=	Particle drag coefficient	[-]
$d_n$	=	Nominal diameter	[m]
$d_p$	=	Particle diameter	[m]
$e_s$	=	Coefficient of restitution	[-]
$F_D$	=	Drag Force	[N]
$g$	=	Gravitational acceleration	[m/s <sup>2</sup> ]
$g_o$	=	Radial distributionfunction	[-]

$H$	=	Particle Bed Height	[m]
$I$	=	Identity matrix	[-]
$K_{\text{drag}}$	=	Momentum exchange coefficient	[kg/m <sup>3</sup> -s]
$p$	=	Pressure	[Pa]
$P_s$	=	Granular pressure	[Pa]
$Re$	=	Reynolds number	[-]
$V_{\text{mf}}$	=	Minimum fluidization velocity	[m/s]
$V_g$	=	Gas velocity	[m/s]
$V_s$	=	Solid particle velocity	[m/s]
$V_t$	=	Particle terminal velocity	[m/s]
$\dot{V}$	=	Particle volume	[m <sup>3</sup> ]

## **Vita**

A S M Raufur Rahim Chowdhury was born in 15th January, 1990 in Khulna, Bangladesh. He is the son of A K M Shahadat Hossain Chowdhury and Gulshan Ara Chowdhury. In 2007 he has completed his college degree from Bir Shreshtha Noor Mohammad Rifles Public College, Dhaka, Bangladesh and joined the University of Texas at El Paso in 2009. He completed his Bachelor of Science Degree in Mechanical Engineering from the University of Texas at El Paso in December, 2012. He worked with a group of students to build an autonomous crane system as his undergraduate senior design project. Besides pursuing his Bachelor's degree he worked as an undergraduate research assistant in the research labs at the University of Texas at El Paso. After finishing his Bachelor's degree he joined in the Master's program at the University of Texas at El Paso in January 2013. He worked as a Graduate Research Assistant at NASA Center for Space Exploration Technology Research (cSETR) for last one and half year where he focused on Investigation on a Gas-Solid Fluidized Bed Hydrodynamics and development of a new drag correlation and implementation of the developed drag model in the computational code. Within this period he submitted three full conference paper and presented in 49th AIAA/ASME/SAE/ASEE Joint Propulsion Conference (JPC) and the 11th International Energy Conversion, July 14-17, 2013, San Jose, CA. He also submitted one article for 2nd Southwest Energy Science and Engineering Symposium, 2012 and another article for the 3rd Southwest Energy Science and Engineering Symposium, in 2013. He also worked as a teaching assistant for the Graphics Design & Fundamentals class on Spring 2014. His proposal was awarded for Provost's Summer-2014 Student Research Assistant Program.

Permanent address: House-2, Road-20, Satkhira Court,  
Satkhira, Khulna, 9400

This thesis was typed by A S M Raufur Rahim Chowdhury.